

博士論文

Integrated Optical Unitary Converter Based on Multi-Plane Light Conversion

(多面光変換法に基づく
集積光ユニタリ変換器に関する研究)

令和元年11月29日提出

指導教員 中野 義昭 教授

東京大学大学院工学系研究科

電気系工学専攻

37-167092

唐 睿

Abstract

An integrated optical unitary converter (OUC), which can realize arbitrary $N \times N$ unitary transformation on chip, is promising for widespread applications in various areas, such as optical communication, quantum information processing, and optical neural networks. For example, mode-division-multiplexing (MDM) is the key technology to realize higher-capacity optical communication systems, but the mode coupling effect that occurs inside few-mode fibers (FMFs) scrambles all the signals that are originally carried by different modes of the FMF. In this case, an OUC can be employed to compensate for the mode coupling effect, thus functioning as an all-optical multi-input-multi-output (MIMO) mode demultiplexer. Compared with the MIMO mode demultiplexing by digital signal processing (DSP), all-optical demultiplexing offers unique advantages, such as bit-rate-independent operation and low power consumption. Besides optical communication, with the revival of optical computing, especially in artificial neural networks, OUCs are attracting emerging interest for realizing deep learning processors with significantly less power consumption. Deep learning relies heavily on matrix-vector multiplication. Although an OUC can only generate unitary matrices, non-unitary matrices can also be generated using two OUCs along with a variable optical attenuator array, based on singular value decomposition (SVD). Direct matrix-vector multiplication in the optical domain, enabled by this scheme, can theoretically reduce energy consumption to a great extent.

To date, integrated $N \times N$ OUCs have been demonstrated on silica, InP, SiN, and silicon-on-insulator (SOI) platforms, using cascaded 2×2 Mach-Zehnder interferometers (MZIs) based on Reck's scheme or its variation. However, all these existing OUCs suffer two common problems: 1. the operation bandwidths are limited to less than 10 nm, which prevent their deployment into wavelength-division-multiplexing (WDM) optical communication systems; 2. the device performances are sensitive to fabrication errors, due to sensitive 50:50 optical splitters. On the other hand, the multi-plane light conversion (MPLC) is a free-space scheme that can realize reconfigurable continuous unitary transformations. The symmetric and robust nature of MPLC brings the hope to solve the problems in existing integrated OUCs. In this thesis, we propose and demonstrate novel integrated OUCs based on MPLC.

Chapter 1 introduces the background of integrated OUCs and explains the problems of previous works.

Chapter 2 first introduces the basics of photonic integrated circuits (PICs), including the analysis of optical waveguides, several simulation methods, and waveguide-based components. The waveguide analysis gives the basic properties of optical waveguides, especially the concept of polarization and mode. The finite difference method (FDM) is suitable for complicated waveguide analysis and the eigenmode expansion method (EME) is suitable for simulating passive photonic devices with periodic structures. The operation principles of MMI coupler, directional coupler, phase shifter, Mach-Zehnder interferometer (MZI), and spot-size converter are explained in detail. Next, the theory of MPLC is introduced. Any unitary transformation can be realized by a finite sequence of phase plate and Fourier transformation.

Chapter 3 first presents the proposal of a novel integrated OUC structure for wideband operations, which consists of cascaded stages of multimode interference (MMI) couplers and phase shifter arrays. From the numerical analysis, we show the ability of this device to implement reconfigurable $N \times N$ unitary conversions with high fidelities. By using more than N stages, desired unitary matrices are realized with mean squared errors (MSEs) smaller than -20 dB for all tested cases. Moreover, we show an example of applying the device to 16-mode unscrambling in MDM transmission systems with a modal crosstalk less than -24 dB. Next, we experimentally demonstrate a 3×3 OUC on a compact silicon chip based on the proposed structure. By optimizing the phase shifters with a custom-designed printed circuit board (PCB), reconfigurable 3-mode demultiplexing is realized with a wavelength-dependent loss of less than 3 dB and a modal crosstalk of less than -10 dB over 23-nm (1542.5~1565.5 nm) wavelength range. Besides, error-free demultiplexing of 40-Gbps non-return-to-zero (NRZ) signals is successfully demonstrated. This is the first experimental demonstration of an integrated OUC based on MPLC.

Chapter 4 first presents the proposal a novel integrated OUC that is robust to fabrication errors, which consists of cascaded stages of multiport directional couplers (DCs) and phase shifter arrays. Similarly, from numerical analysis, we show the ability of this device to implement reconfigurable $N \times N$ unitary conversions with high fidelities. The robustness is attributed to the inherent property of the multiport DC because the

port-dependent loss is nearly eliminated. The numerical analysis further shows that the device performance is related to the entropy of coupling of the multiport DC. We can find a wide range of waveguide gap (G) and length (L) of the multiport DC that can yield a relatively good device performance. Next, we experimentally demonstrate a 4×4 integrated OUC on the SOI platform based on the proposed structure. By optimizing all the phase shifters with the PCB, reconfigurable all-optical 4-mode demultiplexing is realized with a modal crosstalk of less than -10.5 dB at the 1550-nm wavelength. The relatively large modal crosstalk results from the limitation of the driver circuit, which can drive each phase shifter only up to 1.3π . Error-free demultiplexing of 40 Gbps NRZ signals is also demonstrated.

Chapter 5 presents the design and preliminary characterization results of a 10×10 OUC using multiport DCs, and compares the devices in this work with previous demonstrations. While all other works are based on the MZI structure, the OUCs demonstrated in this work present different methods that have unique advantages, such as the wide operation bandwidth or robustness against fabrication errors. What's more, the 10×10 OUC in this work is the largest-scale device that obeys the standard $N\times N$ structure.

Chapter 6 concludes this thesis and discusses the future prospect of this work. Further efforts should be put into finding the rigorous proof that the proposed integrated OUC structures are universal to arbitrary unitary transformation, although the numerical results indicate that they can realize a large number of desired unitary transformation with sufficiently-high fidelities. In addition, the device performance, optimization time, power consumption, and device size should be further improved.

Table of Contents

Chapter 1	Introduction	1
1.1	Optical unitary converter	1
1.2	Photonic integrated circuits	3
1.3	Previous work	4
1.3.1	Reck's scheme	4
1.3.2	Multi-plane light conversion	6
1.4	Outline of thesis	7
Chapter 2	Fundamental theories	9
2.1	Optical waveguide	9
2.1.1	Slab waveguide	9
2.1.2	Rectangular waveguide	14
2.2	Simulation methods	16
2.2.1	Finite difference method	17
2.2.2	Eigenmode expansion method	19
2.3	Waveguide-based components	22
2.3.1	Silicon waveguide	22
2.3.2	Directional coupler	24
2.3.3	Multimode interference (MMI) coupler	28
2.3.4	Phase shifter	32
2.3.5	Mach-Zehnder interferometer	34
2.3.6	Spot-size converter	35
2.4	Multi-plane light conversion	36
2.5	Summary	37
Chapter 3	Wideband integrated OUC using MMI couplers	39
3.1	Proposed structure	39

3.2 Numerical analysis	40
3.2.1 Simulated annealing algorithm	40
3.2.2 Mean squared error	42
3.2.3 Modal crosstalk	44
3.3 Device design	47
3.3.1 3×3 MMI coupler	47
3.3.2 3×3 OUC	51
3.4 Fabricated device.....	52
3.5 Device characterization	52
3.5.1 Propagation loss	52
3.5.2 Phase shifter	53
3.5.3 Custom-designed electronic circuit.....	55
3.5.4 Mode unscrambling experiments	58
3.5.5 40-Gbps signal demultiplexing	64
3.6 Summary	65
Chapter 4 Robust integrated OUC using multiport direction couplers.....	67
4.1 Proposed structure	67
4.2 Numerical analysis	69
4.2.1 Mean squared error	71
4.2.2 Modal crosstalk	78
4.2.3 Discussion	81
4.3 Device design and fabricated chip.....	81
4.4 Device characterization	83
4.4.1 Phase shifter	83
4.4.2 Mode unscrambling experiments	83
4.4.3 40-Gbps signal demultiplexing	87
4.5 Summary	89

Chapter 5	Large-scale integrated OUC using multiport directional couplers.....	90
5.1	Device design and fabricated chip.....	90
5.2	Device characterization	91
5.2.1	Propagation loss and phase shifter	91
5.2.2	Custom-designed electronic circuit.....	92
5.2.3	Chip packaging.....	94
5.3	Comparison with previous work	94
5.4	Summary	95
Chapter 6	Conclusions	96
Appendix I	Source codes for numerical analysis	98
Appendix II	Source code written into the microcontroller	101
Appendix III	Wavelength dependencies of the MMI coupler and the multiport DC	105
Bibliography	107
Publications	119
Acknowledgement.....		121

Chapter 1 Introduction

1.1 Optical unitary converter

Linear optics is a sub-field of optics that consists of linear optical components such as lenses, mirrors, waveplates, and diffraction gratings. In linear optical devices, there is no amplification, negligible absorption, and the superposition principle applies. This means that after propagating through a linear optical device, the spatial distribution of amplitude and phase of the input light may change, but the energy is always conserved. Therefore, the transformation of light caused by a linear device must be a unitary transformation [1]. This unitary transformation can be continuous or discrete. For example, a phase plate implements a continuous unitary transformation by altering the transverse phase distribution of the light passing through it, and a 2×2 optical switch (2 input ports and 2 output ports) implements a discrete 2×2 unitary transformation by directing light from one input port to one output port. In the discrete case, an $N \times N$ optical device (N input ports and N output ports) implementing an $N \times N$ unitary transformation means that the complex transfer matrix of this device is an $N \times N$ unitary matrix. Optical unitary converter (OUC) is defined as a linear optical device that is able to implement any $N \times N$ unitary transformation. In other words, the complex transfer matrix of an $N \times N$ OUC can be configured to any $N \times N$ unitary matrix.

The ability to implement arbitrary $N \times N$ unitary transformation is fundamentally interesting and can have widespread applications in many areas, such as optical communication, quantum information processing, and artificial neural networks. In optical communication, mode-division-multiplexing (MDM) is a key technology to further increase the transmission capacity beyond 100 Tb/s [2]. The information in an MDM system is carried by the transverse modes of a few-mode fiber (FMF), which has a larger core diameter than that of the single-mode fiber. These modes are initially mutually orthogonal, but due to the mode coupling effect [3] induced by the bending or twisting of the FMF, signals carried by different modes will mix together at the receiver side. If the mode-dependent propagation loss of the FMF is negligible, the mode coupling effect can be described by a unitary matrix. Therefore, we can use an OUC to implement the inversed mode coupling matrix to retrieve the original signals, as illustrated in Fig. 1.1. This all-optical multi-input-multi-output (MIMO) processing

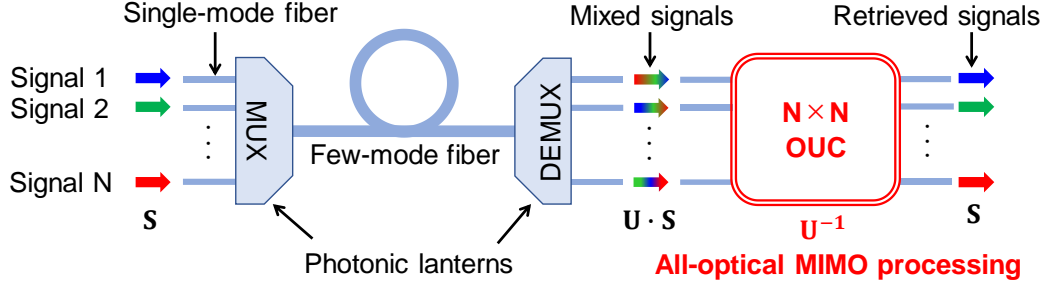


Fig. 1.1. Schematic of all-optical mode unscrambling using an OUC. \mathbf{S} is an N -element vector that represents the multiple input signals, \mathbf{U} is an $N \times N$ unitary matrix that represents the mode coupling effect. The OUC implements the inverse matrix of \mathbf{U} to retrieve the original signals.

approach is independent of the signal bit rate, unlike the MIMO processing by digital signal processing (DSP), and can be significantly more energy-efficient than using DSP [4].

Furthermore, non-unitary matrices can also be implemented using two OUCs and a variable optical attenuator/amplifier array, based on singular value decomposition (SVD) [5]. This enables direct matrix-matrix and matrix-vector multiplication in the optical domain and can be useful in artificial neural networks (ANNs). Figure 1.2 depicts the way of applying OUCs into an ANN. Each layer consists of an optical matrix-vector multiplier followed by the nonlinear threshold function. Direct matrix-vector multiplication in the optical domain is energy-efficient [6] and can be extremely fast since the computation is performed at the speed of light. In addition, the OUC is also an attractive platform for quantum information processing: boson sampling [7] can

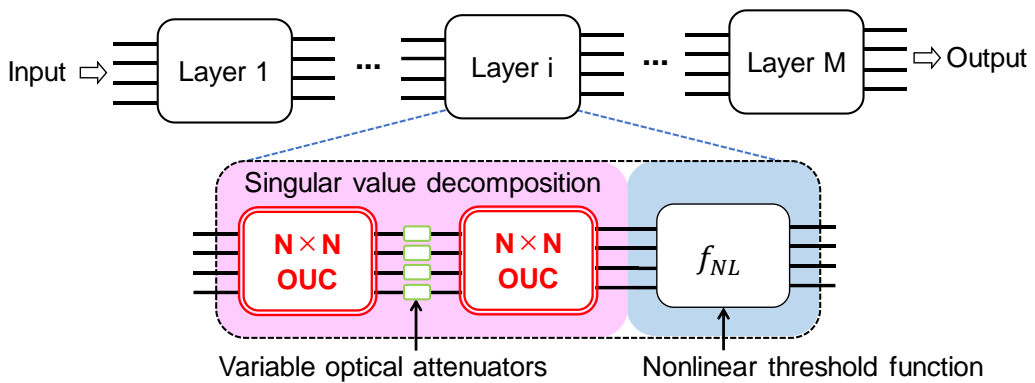


Fig. 1.2. Schematic of applying OUCs into an artificial neural network. Two OUCs together with a variable optical attenuator array can implement non-unitary matrices, according to singular value decomposition. Direct matrix-vector multiplication in the optical domain is energy-efficient and can be extremely fast.

be characterized by measuring the photon probability distribution at the output of the OUC; various quantum gates can be constructed to enable optical quantum computing.

1.2 Photonic integrated circuits

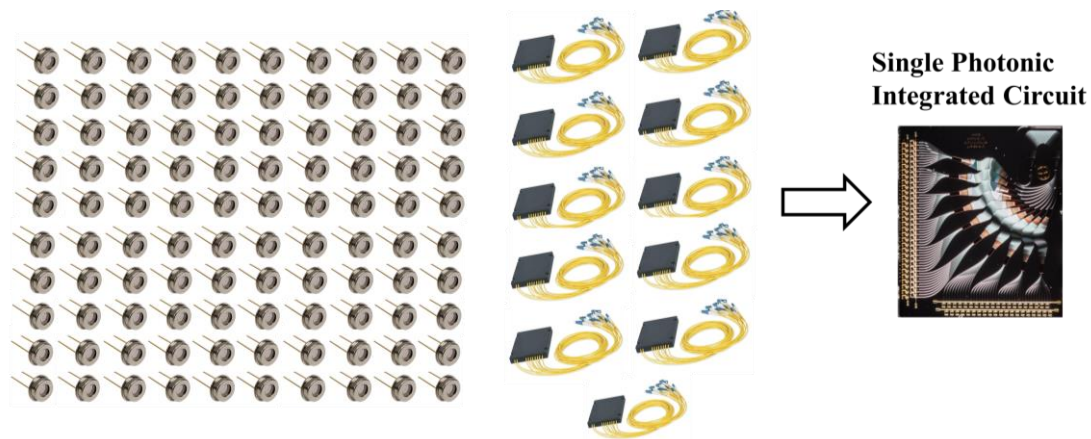
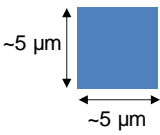
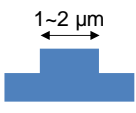
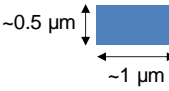
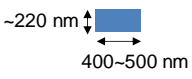
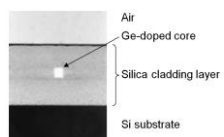
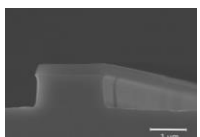
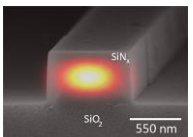
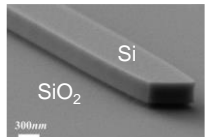


Fig. 1.3. 100 photodetectors and 11 wavelength demultiplexers are integrated in a $6 \times 8\text{-mm}^2$ chip [8].

Massive and various optical components can be integrated into a single chip to form a photonic integrated circuit (PIC). For example, 100 photodetectors and 11 wavelength demultiplexers can be integrated in a $6 \times 8\text{-mm}^2$ chip [8], as shown in Fig. 1.3. Large-scale photonic integration enables complicated optical systems to be fabricated on a compact chip. Therefore, compared with OUCs using bulky free-space optical components, integrated OUCs are much more attractive in terms of the system scale and device dimension.

Tab. 1.1. List of common optical waveguides

Core material	SiO ₂	InP	SiN	Si
Typical geometry				
Sample image	 [9]	 [10]	 [11]	 [12]

Light in a PIC is confined and propagating in optical waveguides, which comprise a core and a cladding with different refractive indices. The refractive index of the core (n_1) is larger than that of the cladding (n_2), so that the light is guided waveguides through total internal reflection. Table 1.1 summarizes several typical waveguide geometries, core materials, and sample images [9, 10, 11, 12]. Among these, Si waveguide has the largest refractive index contrast between the core and cladding and thus can achieve the largest integration scale.

1.3 Previous work

1.3.1 Reck's scheme

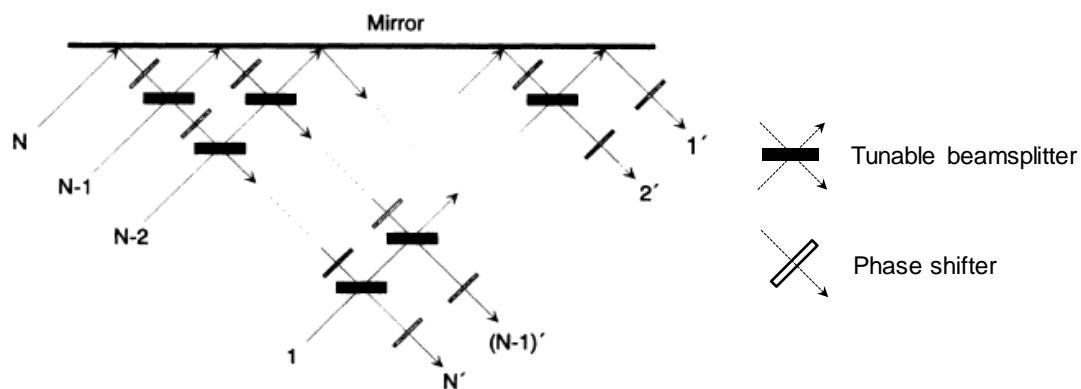


Fig. 1.4. A triangular array of tunable beam splitters can implement any $N \times N$ unitary matrix. Each diagonal row of tunable beam splitters reduces the effective dimension of the Hilbert space by one [13].

Reck et al. proposed the first scheme to experimentally realize arbitrary unitary operator in 1994 [13]. As shown in Fig. 1.4, it comprises a triangular array of tunable beam splitters and phase shifters. Any $N \times N$ unitary matrix can be recursively factorized into a sequence of 2D beam splitter transformations. In integrated optics, a tunable Mach-Zehnder interferometer (MZI) can function as a tunable beam splitter, as shown in Fig. 1.5. The MZI is composed of two 50:50 waveguide couplers and a phase shifter placed on top of one arm. The phase shifter induces a phase difference between the two

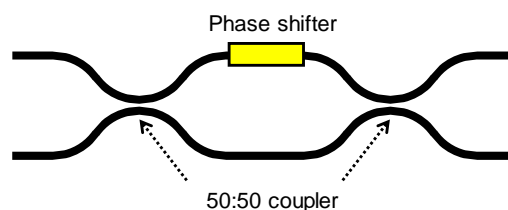


Fig. 1.5. Schematic of an MZI. The power splitting ratio at the two output arms can be adjusted by tuning the phase shifter.

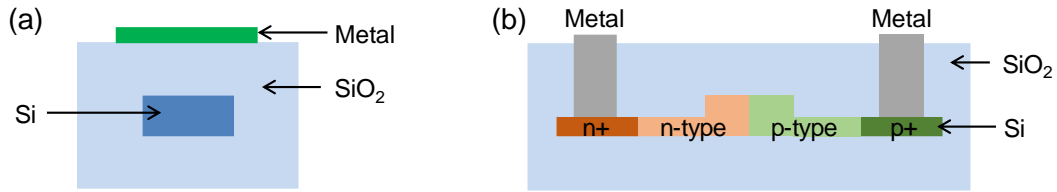


Fig. 1.6. Cross-sectional structure of (a) a thermo-optic phase shifter and (b) a plasma-dispersion-based phase shifter.

arms. Therefore, the power splitting ratio at the two output arms can be adjusted by tuning the phase shifter. The phase shifter can be realized based on the electro-optic effect, the thermo-optic effect or the plasma dispersion effect [14]. These effects change the refractive index of the waveguide through an external electric field, heat and free carriers, respectively. Because the electro-optic effect in silicon waveguides is relatively weak, phase shifters for silicon waveguides are either based on the thermo-optic effect or the plasma dispersion effect. Figure 1.6 shows the cross-sectional structure of two typical silicon photonic phase shifters. In Fig. 1.6(a), the metal film functions as a resistor that dissipates heat to the waveguide when electric currents flow through it; In Fig. 1.6(b), the silicon layer is doped in n-type and p-type regions so that free carriers can be injected into or depleted from the core.

Using the MZI and the phase shifter as two basic building blocks, the structure in Fig. 1.7 implements the Reck's scheme on chip. Each coupler symbol in Fig. 1.7 represents a tunable MZI along with an external phase shifter. This structure was first experimentally demonstrated using SiO₂ waveguides in 2015 [15] and later using Si [16, 17, 18, 19], InP [20, 21] and SiN [22] waveguides, respectively.

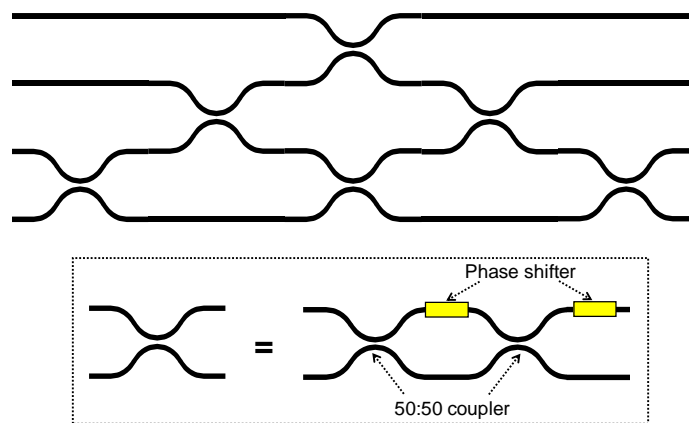


Fig. 1.7. Schematic of an integrated 4×4 OUC based on the Reck's scheme. Each coupler symbol represents a tunable MZI along with an external phase shifter.

However, several problems exist in this structure: First, each path has an unequal number of MZIs. This asymmetry brings the path-dependent loss so that the transfer matrices are no longer unitary for large-scale chips. Second, perfect 50:50 couplers are required in this scheme, while the power splitting ratio in actual devices is sensitive to fabrication inaccuracies. Even a slight deviation from their ideal conditions, caused by fabrication errors, accumulates in the cascaded stages, thus presenting a great challenge to realize large-scale OUCs with high performance.

1.3.2 Multi-plane light conversion

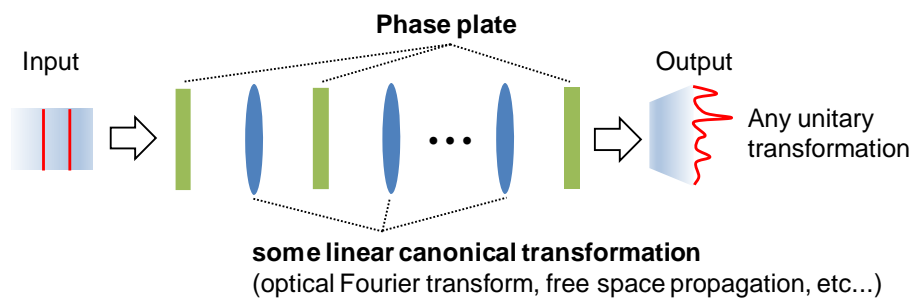


Fig. 1.8. Principle of the MPLC approach. Any unitary transformation can be approximately realized using a finite number of reconfigurable phase plates and some linear canonical transformations.

The multi-plane light conversion (MPLC) approach is another method to approximately realize arbitrary unitary transformation, which was proposed by J.-F. Morizur et al. in 2010 [23]. The fundamental idea is that using cascaded stages of reconfigurable phase plates separated by some linear canonical transformations, the entire transformation can be approximately configured to any unitary transformation, as illustrated in Fig. 1.8. In principle, the transformation fidelity can be improved by increasing the stage number. However, the stage number in actual devices is limited by the control complexity and the device size. The original demonstration used spatial light modulators (SLMs) as the phase plates and successfully converted an input TEM_{00} -mode light into another TEM-mode light. Figure 1.9 shows one example of converting

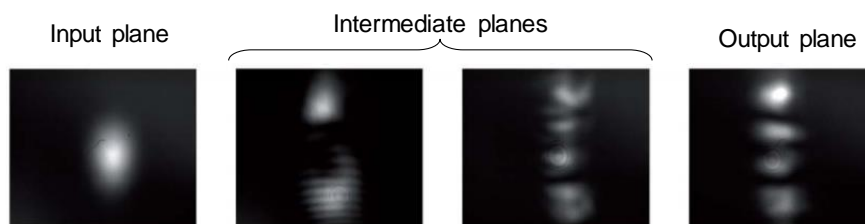


Fig. 1.9. One example of converting the TEM_{00} mode (leftmost) into the TEM_{30} mode (rightmost) using SLMs [23].

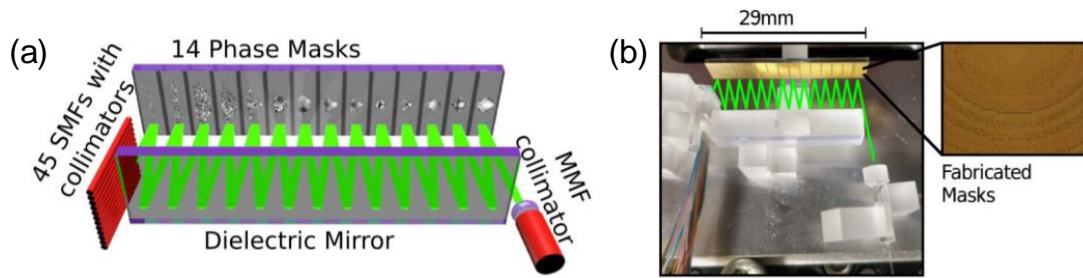


Fig. 1.10. A fixed mode converter that can simultaneously convert the modes of 45 SMFs into the transverse modes of an MMF. (a) Schematic. (b) Real device [24].

the TEM_{00} mode into the TEM_{30} mode [23]. These images are mode profiles measured by a charge-coupled device (CCD) camera. As can be seen, the input mode (leftmost) is stepwise converted into the output mode (rightmost). Although the output mode slightly differs from an ideal TEM_{30} mode, simulation results show that the conversion can be further improved using more stages. In the case that reconfigurable conversions are not required, the phase information in the phase plates can be encoded into fixed phase masks. Figure 1.10 shows a device that can simultaneously convert the modes of 45 single-mode fibers (SMFs) into the transverse modes of a multimode fiber (MMF) [24]. The wavefront matching method [25] was employed to reduce the number of phase masks to only 14.

Previous demonstrations aimed for continuous unitary transformation, but the principle should apply to the discrete case as well. Because no intrinsic asymmetry exists in this approach, the port-dependent loss can be significantly smaller than that in the Reck's scheme. Furthermore, the conversion fidelity can be improved by increasing the number of stages, unlike the Reck's scheme where the fidelity cannot be improved. Therefore, it is possible to create novel and high-performance integrated OUCs based on MPLC.

1.4 Outline of thesis

The objective of this research is to develop novel integrated OUCs based on MPLC and demonstrate their applications in the MDM optical communication systems. This chapter has introduced the background of the integrated OUC and several relevant works. Chapter 2 introduces the basic knowledge of photonic integrated circuits (PICs) and MPLC, which are necessary for the subsequent numerical analysis and device design. Chapter 3 presents the proposal and numerical analysis of wideband integrated OUCs using multimode interference (MMI) couplers, and the demonstration of a 3×3

device integrated on a silicon chip. Chapter 4 presents the proposal and numerical analysis of robust integrated OUCs using multiport directional couplers (DCs), and the demonstration of a 4×4 device integrated on a silicon chip. Chapter 5 presents the design and preliminary characterization of a large-scale (10×10) integrated OUC using multiport DCs. Chapter 6 concludes this thesis and gives the outlook of this work.

Chapter 2 Fundamental theories

This chapter first introduces the basics of photonic integrated circuits (PICs), including optical waveguides, simulation methods, and waveguide-based components, then introduces the theory of multi-plane light conversion (MPLC).

2.1 Optical waveguide

2.1.1 Slab waveguide

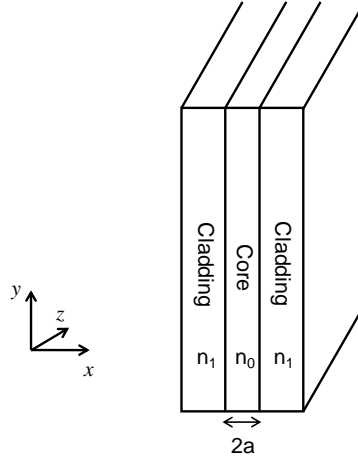


Fig. 2.1. A slab waveguide. The core layer and cladding layers are assumed to extend infinitely in the y direction.

The light propagating through a waveguide is confined by the total internal reflection at the core-cladding interface. Guided modes of a waveguide are formed by the interference in the transverse direction. First, we analyze the transverse modes of the slab waveguide shown in Fig. 2.1 [26]. A slab waveguide consists of one core layer and two cladding layers. The refractive index of the core (n_0) is larger than that of the cladding (n_1). These layers are assumed to extend infinitely in the y direction. According to the Maxwell's equations, the relationships between the electric field \mathbf{E} and the magnetic field \mathbf{H} in a homogenous and lossless dielectric medium are

$$\nabla \times \mathbf{E} = -\mu \frac{\partial \mathbf{H}}{\partial t}, \quad (2.1)$$

$$\nabla \times \mathbf{H} = \varepsilon \frac{\partial \mathbf{E}}{\partial t}, \quad (2.2)$$

where t is the time, ε and μ are the permittivity and permeability of the medium, respectively. The permittivity and permeability can be written as

$$\varepsilon = \varepsilon_0 n^2, \quad (2.3)$$

$$\mu = \mu_0, \quad (2.4)$$

where n is the refractive index of the medium, ε_0 and μ_0 are the permittivity and the permeability in vacuum, respectively. Let us consider a plane wave propagating in the slab waveguide, whose time-varying electric field $\tilde{\mathbf{E}}$ and magnetic field $\tilde{\mathbf{H}}$ are in the form of

$$\tilde{\mathbf{E}} = \mathbf{E}(x, y)e^{j(\omega t - \beta z)}, \quad (2.5)$$

$$\tilde{\mathbf{H}} = \mathbf{H}(x, y)e^{j(\omega t - \beta z)}. \quad (2.6)$$

where ω is the angular frequency and β is the propagation constant. Substitute Eq. (2.5-2.6) into Eq. (2.1-2.2), we obtain:

$$\begin{cases} \frac{\partial E_z}{\partial y} + j\beta E_y = -j\omega\mu_0 H_x \\ -j\beta E_x - \frac{\partial E_z}{\partial x} = -j\omega\mu_0 H_y \\ \frac{\partial E_y}{\partial x} - \frac{\partial E_x}{\partial y} = -j\omega\mu_0 H_z, \end{cases} \quad (2.7)$$

$$\begin{cases} \frac{\partial H_z}{\partial y} + j\beta H_y = -j\omega\varepsilon_0 n^2 E_x \\ -j\beta H_x - \frac{\partial H_z}{\partial x} = -j\omega\varepsilon_0 n^2 E_y \\ \frac{\partial H_y}{\partial x} - \frac{\partial H_x}{\partial y} = -j\omega\varepsilon_0 n^2 E_z. \end{cases} \quad (2.8)$$

Because the core layer and cladding layers extend infinitely in the y direction, \mathbf{E} and \mathbf{H} do not have y -axis dependencies, we have

$$\frac{\partial \mathbf{E}}{\partial y} = 0, \quad (2.9)$$

$$\frac{\partial \mathbf{H}}{\partial y} = 0. \quad (2.10)$$

Substitute Eq. (2.9-2.10) into Eq. (2.7-2.8), we can obtain two independent electromagnetic modes, one of which satisfies the equation

$$\frac{d^2 E_y}{dx^2} + (k^2 n^2 - \beta^2) E_y = 0, \quad (2.11)$$

where k is the angular wavenumber, and

$$H_x = -\frac{\beta}{\omega\mu_0} E_y, \quad (2.12)$$

$$H_z = \frac{j}{\omega\mu_0} \frac{dE_y}{dx}, \quad (2.13)$$

$$E_x = E_z = H_y = 0. \quad (2.14)$$

Because no electric field component exists in the propagation direction ($E_z = 0$), this mode is called transverse electric (TE) mode. The other mode satisfies the equation

$$\frac{d}{dx} \left(\frac{1}{n^2} \frac{dH_y}{dx} \right) + \left(k^2 - \frac{\beta^2}{n^2} \right) H_y = 0, \quad (2.15)$$

where

$$E_x = \frac{\beta}{\omega\epsilon_0 n^2} H_y, \quad (2.16)$$

$$E_z = -\frac{j}{\omega\epsilon_0 n^2} \frac{dH_y}{dx}, \quad (2.17)$$

$$E_y = H_x = H_z = 0. \quad (2.18)$$

Similarly, because no magnetic field component exists in the propagation direction ($H_z = 0$), this mode is called transverse magnetic (TM) mode.

Electromagnetic fields and propagation properties of TE and TM modes can be obtained by solving Eq. (2.11-2.14) and Eq. (2.15-2.18), respectively. Here, we consider the TE modes of the slab waveguide in Fig. 2.1. The refractive index profile of the waveguide is shown in Fig. 2.2. Because the guided modes are confined in the core and decay exponentially in the cladding, the electric field can be expressed as

$$E_y = \begin{cases} \cos(\kappa a - \phi) e^{-\sigma(x-a)}, & x > a \\ \cos(\kappa x - \phi), & -a \leq x \leq a \\ \cos(\kappa a + \phi) e^{\sigma(x+a)}, & x < -a, \end{cases} \quad (2.19)$$

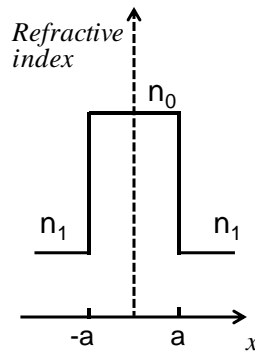


Fig. 2.2. Refractive index profile of the slab waveguide.

where the amplitude is normalized to 1, ϕ is the inclination angle of the incident wave, κ and σ are the wavenumbers along the x direction and are given by

$$\begin{cases} \kappa = \sqrt{k^2 n_0^2 - \beta^2} \\ \sigma = \sqrt{\beta^2 - k^2 n_1^2}. \end{cases} \quad (2.20)$$

Because H_z is continuous at the boundaries ($x = \pm a$), from Eq. (2.13) and Eq. (2.19), we can obtain

$$\begin{cases} \kappa \sin(\kappa a + \phi) = \sigma \cos(\kappa a + \phi) \\ \sigma \cos(\kappa a - \phi) = \kappa \sin(\kappa a - \phi). \end{cases} \quad (2.21)$$

Equation (2.21) can be further simplified into

$$\tan(u + \phi) = \tan(u - \phi) = \frac{w}{u}, \quad (2.22)$$

where $u = \kappa a$ and $w = \sigma a$. From Eq. (2.20) and Eq. (2.22), we can obtain

$$w = u \tan\left(u - \frac{m\pi}{2}\right) \quad (2.23)$$

$$\phi = \frac{m\pi}{2} \quad (m = 0, 1, 2, \dots) \quad (2.24)$$

$$u^2 + w^2 = k^2 a^2 (n_0^2 - n_1^2) \equiv v^2. \quad (2.25)$$

Equation (2.23-2.25) are the dispersion equations for the TE_m modes of the symmetric slab waveguide, where the refractive indices of the top cladding and bottom cladding are the same. The dispersion equations for TM modes can be obtained by following the

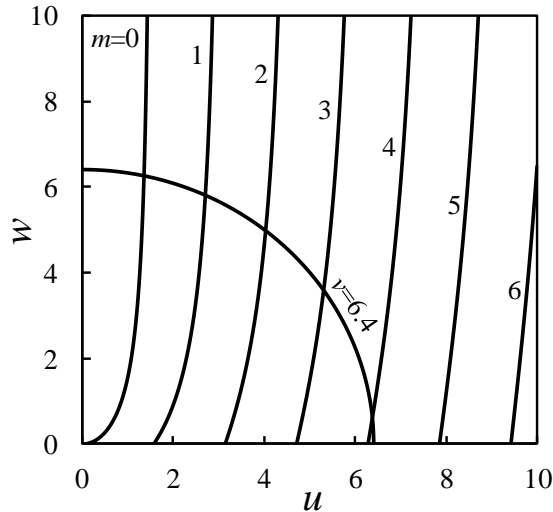


Fig. 2.3. u - w relationship of TE modes in a slab waveguide ($n_0 = 3.476$, $n_1 = 1.444$, $a = 500$ nm, $\lambda = 1550$ nm).

same procedure. The wavenumber κ has to be a real number for guided modes, from Eq. (2.20), we obtain

$$n_1 \leq n_{\text{eff}} \leq n_0, \quad (2.25)$$

where $n_{\text{eff}} = \beta/k$ and is called the effective refractive index.

In Fig. 2.3, we plot the u - w relationship of TE modes using the parameters of $n_0 = 3.476$, $n_1 = 1.444$, $a = 500$ nm, $\lambda = 1550$ nm. The circular curve ($v = 6.4$) intersects with the curve $m = 0, 1, 2, 3$ and 4 , which means that TE_{0-4} modes are supported in the slab waveguide. The intersecting points give the solutions of the dispersion equations. At a given wavelength, increasing the thickness of the core layer or the refractive index difference between the core and the cladding can increase the number of supported modes. A waveguide that only supports the fundamental mode (TE_0 and TM_0 mode) is called single-mode waveguide, that also supports higher-order modes is called multimode waveguide. Higher-order modes have smaller propagation constants than the fundamental mode, this leads to the modal dispersion in a multimode waveguide/fiber. Figure 2.4 shows the profiles of several TE modes supported in the

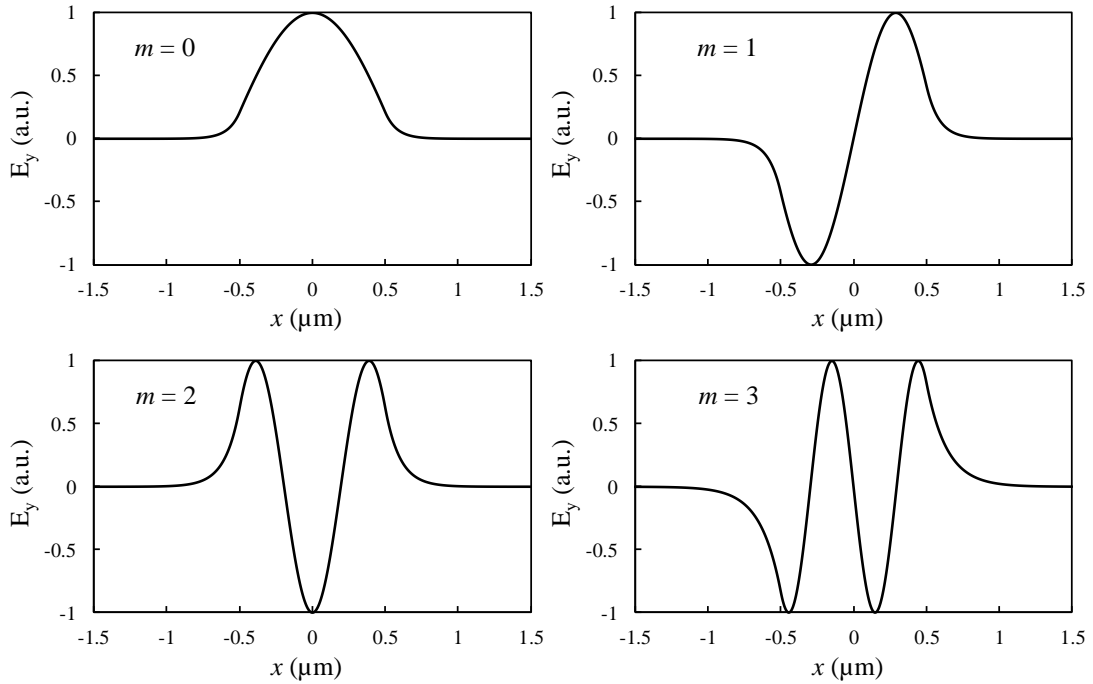


Fig. 2.4. Profiles of several TE modes supported in a slab waveguide. A small fraction of the wave exists in the cladding region ($|x| > 0.5$ μm).

above slab waveguide. In each mode profile, a small fraction of the wave exists in the cladding region ($|x| > 0.5$ μm), which is called evanescent wave. The evanescent wave

causes the coupling between adjacent waveguides and is important for the operation of direction couplers.

2.1.2 Rectangular waveguide

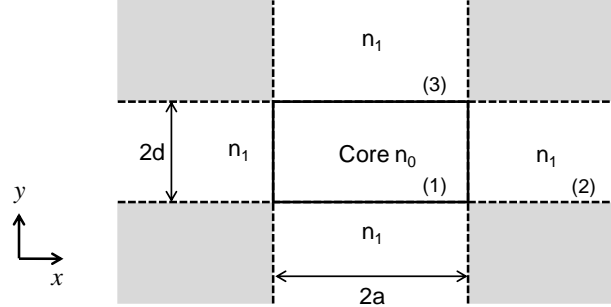


Fig. 2.5. Cross-sectional view of a rectangular waveguide. The core layer and cladding layers are assumed to extend infinitely in the y direction.

Analyzing a slab waveguide is relatively easy, but such waveguide does not exist in actual devices because it assumes an infinite length in the y direction. In practice, the waveguide core has finite lengths in both the x and y direction. The simplest core shape is the rectangle, as shown in Fig. 2.5. This rectangular waveguide, also called channel waveguide, can be analyzed by a simplified method proposed by E. A. J. Marcatili [27]. One assumption is that the electromagnetic field in the shaded cladding region in Fig. 2.5 can be neglected, because the guided modes decay rapidly in the cladding region. Therefore, the rectangular waveguide can be effectively decomposed into two independent slab waveguides in the x and y direction, respectively. Unlike the slab waveguide, the electric or magnetic component along the propagation direction cannot be zero in the channel waveguide. According to Marcatili's method, E_{pq}^x and E_{pq}^y modes can exist in the channel waveguide, where p and q represent the number of electric field peaks in the x and y direction, respectively.

In the E_{pq}^x mode, E_x and H_y are the predominant components. The wave equation and other electromagnetic field components are given by

$$\frac{\partial^2 H_y}{\partial x^2} + \frac{\partial^2 H_y}{\partial y^2} + (k^2 n^2 - \beta^2) H_y = 0, \quad (2.26)$$

$$\left\{ \begin{array}{l} H_x = 0 \\ E_x = \frac{\omega\mu_0}{\beta} H_y + \frac{1}{\omega\varepsilon_0 n^2 \beta} \frac{\partial^2 H_y}{\partial x^2} \\ E_y = \frac{1}{\omega\varepsilon_0 n^2 \beta} \frac{\partial^2 H_y}{\partial x \partial y} \\ E_z = \frac{-j}{\omega\varepsilon_0 n^2} \frac{\partial H_y}{\partial x} \\ H_z = \frac{-j}{\beta} \frac{\partial H_y}{\partial y}. \end{array} \right. \quad (2.27)$$

On the other hand, E_y and H_x are the predominant components in the E_{pq}^y mode. The wave equation and other electromagnetic field components are given by

$$\frac{\partial^2 H_x}{\partial x^2} + \frac{\partial^2 H_x}{\partial y^2} + (k^2 n^2 - \beta^2) H_x = 0, \quad (2.28)$$

$$\left\{ \begin{array}{l} H_y = 0 \\ E_x = -\frac{1}{\omega\varepsilon_0 n^2 \beta} \frac{\partial^2 H_x}{\partial x \partial y} \\ E_y = -\frac{\omega\mu_0}{\beta} H_x - \frac{1}{\omega\varepsilon_0 n^2 \beta} \frac{\partial^2 H_x}{\partial y^2} \\ E_z = \frac{j}{\omega\varepsilon_0 n^2} \frac{\partial H_x}{\partial y} \\ H_z = \frac{-j}{\beta} \frac{\partial H_x}{\partial x}. \end{array} \right. \quad (2.29)$$

For the E_{pq}^x mode, the solution of Eq. (2.26) is written as

$$H_y = \begin{cases} \cos(k_x x - \phi) \cos(k_y y - \psi) & \text{region (1)} \\ \cos(k_x a - \phi) e^{-\gamma_x(x-a)} \cos(k_y y - \psi) & \text{region (2)} \\ \cos(k_x x - \phi) e^{-\gamma_y(y-d)} \cos(k_y d - \psi) & \text{region (3)}, \end{cases} \quad (2.30)$$

where the amplitude is normalized to 1, the transverse wavenumbers ($k_x, k_y, \gamma_x, \gamma_y$) and the phases (ϕ and ψ) are given by

$$\begin{cases} -k_x^2 - k_y^2 + k^2 n_0^2 - \beta^2 = 0 & \text{region (1)} \\ \gamma_x^2 - k_y^2 + k^2 n_1^2 - \beta^2 = 0 & \text{region (2)} \\ -k_x^2 + \gamma_y^2 + k^2 n_1^2 - \beta^2 = 0 & \text{region (3)} \end{cases} \quad (2.31)$$

$$\begin{cases} \phi = (p-1) \frac{\pi}{2} & (p = 1, 2, \dots) \\ \psi = (q-1) \frac{\pi}{2} & (q = 1, 2, \dots). \end{cases} \quad (2.32)$$

After applying the boundary conditions that E_z is continuous at $x = \pm a$ and H_z is continuous at $y = \pm d$, the dispersion equations are obtained as

$$k_x a = (p - 1) \frac{\pi}{2} + \tan^{-1} \frac{n_0^2 \gamma_x}{n_1^2 k_x} \quad (2.33)$$

$$k_y d = (q - 1) \frac{\pi}{2} + \tan^{-1} \frac{\gamma_y}{k_y}. \quad (2.34)$$

For the E_{pq}^y mode, the solution of Eq. (2.28) is written as

$$H_x = \begin{cases} \cos(k_x x - \phi) \cos(k_y y - \psi) & \text{region (1)} \\ \cos(k_x a - \phi) e^{-\gamma_x(x-a)} \cos(k_y y - \psi) & \text{region (2)} \\ \cos(k_x x - \phi) e^{-\gamma_y(y-d)} \cos(k_y d - \psi) & \text{region (3)}, \end{cases} \quad (2.35)$$

After applying the boundary conditions that H_z is continuous at $x = \pm a$ and E_z is continuous at $y = \pm d$, the dispersion equations are obtained as

$$k_x a = (p - 1) \frac{\pi}{2} + \tan^{-1} \frac{\gamma_x}{k_x} \quad (2.36)$$

$$k_y d = (q - 1) \frac{\pi}{2} + \tan^{-1} \frac{n_0^2 \gamma_y}{n_1^2 k_y}. \quad (2.37)$$

Equation (2.33) and Equation (2.36) correspond to the dispersion equation of the TM and the TE mode of a slab waveguide parallel to the y axis, respectively, while Equation (2.34) and Equation (2.37) corresponds to the dispersion equation of the TE and the TE mode of a slab waveguide parallel to the x axis, respectively .

2.2 Simulation methods

Analytical methods in Sec. 2.1 give the basic mechanism and properties of optical waveguides, but are limited to only a few specific cases. Numerical methods provide more accurate results than the analytical methods and are able to deal with sophisticated waveguide structures. In this section, we introduce the simulation methods for analyzing optical waveguides and optical components.

2.2.1 Finite difference method

The finite difference method (FDM) solves differential equations by approximating them with difference equations, where finite differences approximate the derivatives. In waveguide simulations, the FDM can calculate the spatial profile and frequency dependence of modes by solving Maxwell's equations on a cross-sectional mesh of the waveguide. Several discretization methods can be used to generate the mesh [28, 29, 30]. We introduce the FDM-based mode solver proposed by Z. Zhu and T. G. Brown [30], which used the discretization scheme proposed by Yee [31].

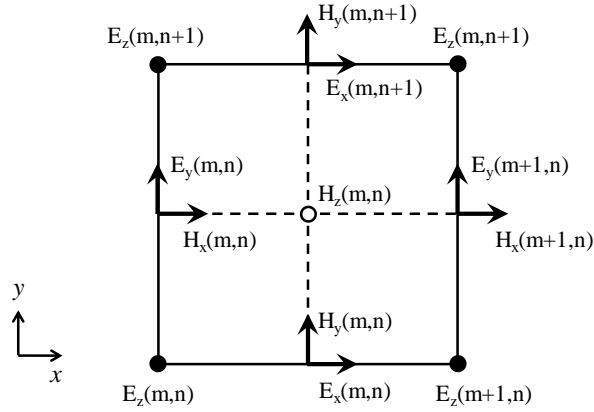


Fig. 2.6. Yee's 2D mesh.

Figure 2.6 shows the Yee's 2D mesh. From Maxwell's curl equations, we can obtain

$$\begin{cases} jk_0 H_x = \frac{\partial E_z}{\partial y} - j\beta E_y \\ jk_0 H_y = -\frac{\partial E_z}{\partial x} + j\beta E_x \\ jk_0 H_z = \frac{\partial E_y}{\partial x} - \frac{\partial E_x}{\partial y} \end{cases} \quad (2.38)$$

$$\begin{cases} -jk_0 \varepsilon_r E_x = \frac{\partial H_z}{\partial y} - j\beta H_y \\ -jk_0 \varepsilon_r E_y = -\frac{\partial H_z}{\partial x} + j\beta H_x \\ -jk_0 \varepsilon_r E_z = \frac{\partial H_y}{\partial x} - \frac{\partial H_x}{\partial y}, \end{cases} \quad (2.39)$$

where k_0 is the wavenumber in free space and ε_r is the relative permittivity. For an infinitely small mesh, the derivatives can be approximated by the differences. Therefore, Equation (2.38) and (2.39) can be rewritten as

$$\left\{ \begin{array}{l} jk_0 H_x(m, n) = \frac{E_z(m, n+1) - E_z(m, n)}{\Delta y} - j\beta E_y(m, n) \\ jk_0 H_y(m, n) = -\frac{E_z(m+1, n) - E_z(m, n)}{\Delta x} + j\beta E_x(m, n) \\ jk_0 H_z(m, n) = \frac{E_y(m+1, n) - E_y(m, n)}{\Delta x} - \frac{E_x(m, n+1) - E_x(m, n)}{\Delta y} \end{array} \right. \quad (2.40)$$

$$\left\{ \begin{array}{l} -jk_0 \varepsilon_{rx}(m, n) E_x(m, n) = \frac{H_z(m, n) - H_z(m, n-1)}{\Delta y} - j\beta H_y(m, n) \\ -jk_0 \varepsilon_{ry}(m, n) E_y(m, n) = -\frac{H_z(m, n) - H_z(m-1, n)}{\Delta x} + j\beta H_x(m, n) \\ -jk_0 \varepsilon_{rz}(m, n) E_z(m, n) = \frac{H_y(m, n) - H_y(m-1, n)}{\Delta x} - \frac{H_x(m, n) - H_x(m, n-1)}{\Delta y}, \end{array} \right. \quad (2.41)$$

where

$$\left\{ \begin{array}{l} \varepsilon_{rx}(m, n) = \frac{\varepsilon_r(m, n) + \varepsilon_r(m, n-1)}{2} \\ \varepsilon_{ry}(m, n) = \frac{\varepsilon_r(m, n) + \varepsilon_r(m-1, n)}{2} \\ \varepsilon_{rz}(m, n) = \frac{\varepsilon_r(m, n) + \varepsilon_r(m-1, n-1) + \varepsilon_r(m, n-1) + \varepsilon_r(m-1, n)}{4}. \end{array} \right. \quad (2.42)$$

Rewrite Eq. (2.40) and (2.41) in the matrix form, we can obtain

$$jk_0 \begin{pmatrix} \mathbf{H}_x \\ \mathbf{H}_y \\ \mathbf{H}_z \end{pmatrix} = \begin{pmatrix} \mathbf{0} & -j\beta \mathbf{I} & \mathbf{U}_y \\ j\beta \mathbf{I} & \mathbf{0} & -\mathbf{U}_x \\ -\mathbf{U}_y & \mathbf{U}_x & \mathbf{0} \end{pmatrix} \begin{pmatrix} \mathbf{E}_x \\ \mathbf{E}_y \\ \mathbf{E}_z \end{pmatrix} \quad (2.43)$$

$$-jk_0 \begin{pmatrix} \varepsilon_{rx} & \mathbf{0} & \mathbf{0} \\ \mathbf{0} & \varepsilon_{ry} & \mathbf{0} \\ \mathbf{0} & \mathbf{0} & \varepsilon_{rz} \end{pmatrix} \begin{pmatrix} \mathbf{E}_x \\ \mathbf{E}_y \\ \mathbf{E}_z \end{pmatrix} = \begin{pmatrix} \mathbf{0} & -j\beta \mathbf{I} & \mathbf{V}_y \\ j\beta \mathbf{I} & \mathbf{0} & -\mathbf{V}_x \\ -\mathbf{V}_y & \mathbf{V}_x & \mathbf{0} \end{pmatrix} \begin{pmatrix} \mathbf{H}_x \\ \mathbf{H}_y \\ \mathbf{H}_z \end{pmatrix}, \quad (2.44)$$

where \mathbf{I} is the identity matrix, \mathbf{U}_x , \mathbf{U}_y , \mathbf{V}_x and \mathbf{V}_y are square matrices that depend on the boundary condition of the rectangular computation windows, ε_{rx} , ε_{ry} and ε_{rz} are diagonal matrices determined by Eq. (2.42).

The eigenvalue equation of TE fields that satisfy Eq. (2.43) and (2.44) is

$$\mathbf{P} \begin{pmatrix} \mathbf{E}_x \\ \mathbf{E}_y \end{pmatrix} = \begin{pmatrix} \mathbf{P}_{xx} & \mathbf{P}_{xy} \\ \mathbf{P}_{yx} & \mathbf{P}_{yy} \end{pmatrix} \begin{pmatrix} \mathbf{E}_x \\ \mathbf{E}_y \end{pmatrix} = \beta^2 \begin{pmatrix} \mathbf{E}_x \\ \mathbf{E}_y \end{pmatrix}, \quad (2.45)$$

where

$$\begin{cases} \mathbf{P}_{xx} = -k_0^{-2} \mathbf{U}_x \boldsymbol{\varepsilon}_{rz}^{-1} \mathbf{V}_y \mathbf{V}_x \mathbf{U}_y + (k_0^2 \mathbf{I} + \mathbf{U}_x \boldsymbol{\varepsilon}_{rz}^{-1} \mathbf{V}_x) (\boldsymbol{\varepsilon}_{rx} + k_0^{-2} \mathbf{V}_y \mathbf{U}_y) \\ \mathbf{P}_{yy} = -k_0^{-2} \mathbf{U}_y \boldsymbol{\varepsilon}_{rz}^{-1} \mathbf{V}_x \mathbf{V}_y \mathbf{U}_x + (k_0^2 \mathbf{I} + \mathbf{U}_y \boldsymbol{\varepsilon}_{rz}^{-1} \mathbf{V}_y) (\boldsymbol{\varepsilon}_{ry} + k_0^{-2} \mathbf{V}_x \mathbf{U}_x) \\ \mathbf{P}_{xy} = \mathbf{U}_x \boldsymbol{\varepsilon}_{rz}^{-1} \mathbf{V}_y (\boldsymbol{\varepsilon}_{ry} + k_0^{-2} \mathbf{V}_x \mathbf{U}_x) - k_0^{-2} (k_0^2 \mathbf{I} + \mathbf{U}_x \boldsymbol{\varepsilon}_{rz}^{-1} \mathbf{V}_x) \mathbf{V}_y \mathbf{U}_x \\ \mathbf{P}_{yx} = \mathbf{U}_y \boldsymbol{\varepsilon}_{rz}^{-1} \mathbf{V}_x (\boldsymbol{\varepsilon}_{rx} + k_0^{-2} \mathbf{V}_y \mathbf{U}_y) - k_0^{-2} (k_0^2 \mathbf{I} + \mathbf{U}_y \boldsymbol{\varepsilon}_{rz}^{-1} \mathbf{V}_y) \mathbf{V}_x \mathbf{U}_y. \end{cases} \quad (2.46)$$

The eigenvalue equation of TM fields that satisfy Eq. (2.43) and (2.44) is

$$\mathbf{Q} \begin{pmatrix} \mathbf{H}_x \\ \mathbf{H}_y \end{pmatrix} = \begin{pmatrix} \mathbf{Q}_{xx} & \mathbf{Q}_{xy} \\ \mathbf{Q}_{yx} & \mathbf{Q}_{yy} \end{pmatrix} \begin{pmatrix} \mathbf{H}_x \\ \mathbf{H}_y \end{pmatrix} = \beta^2 \begin{pmatrix} \mathbf{H}_x \\ \mathbf{H}_y \end{pmatrix}, \quad (2.47)$$

where

$$\begin{cases} \mathbf{Q}_{xx} = -k_0^{-2} \mathbf{V}_x \mathbf{U}_y \mathbf{U}_x \boldsymbol{\varepsilon}_{rz}^{-1} \mathbf{V}_y + (\boldsymbol{\varepsilon}_{ry} + k_0^{-2} \mathbf{V}_x \mathbf{U}_x) (k_0^2 \mathbf{I} + \mathbf{U}_y \boldsymbol{\varepsilon}_{rz}^{-1} \mathbf{V}_y) \\ \mathbf{Q}_{yy} = -k_0^{-2} \mathbf{V}_y \mathbf{U}_x \mathbf{U}_y \boldsymbol{\varepsilon}_{rz}^{-1} \mathbf{V}_x + (\boldsymbol{\varepsilon}_{rx} + k_0^{-2} \mathbf{V}_y \mathbf{U}_y) (k_0^2 \mathbf{I} + \mathbf{U}_x \boldsymbol{\varepsilon}_{rz}^{-1} \mathbf{V}_x) \\ \mathbf{Q}_{xy} = -(\boldsymbol{\varepsilon}_{ry} + k_0^{-2} \mathbf{V}_x \mathbf{U}_x) \mathbf{U}_y \boldsymbol{\varepsilon}_{rz}^{-1} \mathbf{V}_x + k_0^{-2} \mathbf{V}_x \mathbf{U}_y (k_0^2 \mathbf{I} + \mathbf{U}_x \boldsymbol{\varepsilon}_{rz}^{-1} \mathbf{V}_x) \\ \mathbf{Q}_{yx} = -(\boldsymbol{\varepsilon}_{rx} + k_0^{-2} \mathbf{V}_y \mathbf{U}_y) \mathbf{U}_x \boldsymbol{\varepsilon}_{rz}^{-1} \mathbf{V}_y + k_0^{-2} \mathbf{V}_y \mathbf{U}_x (k_0^2 \mathbf{I} + \mathbf{U}_y \boldsymbol{\varepsilon}_{rz}^{-1} \mathbf{V}_y). \end{cases} \quad (2.48)$$

Equation (2.45) and (2.47) can be solved by available numerical routines. The mode profile and effective refractive index can be obtained from the solution.

2.2.2 Eigenmode expansion method

A variety of methods have been developed for simulating passive photonic devices, including the beam propagation method (BPM), finite difference time domain (FDTD) method and eigenmode expansion (EME) method. BPM is an approximation technique for simulating the propagation of light in slowly varying optical waveguides [32] and is probably the first widely used photonic simulation method. The principle of BPM is to remove the fast varying term from the fields and then to solve the now slower varying fields [33], under the assumption that the light is propagating at a small angle with respect to the waveguide axis, which works well for low-index-difference waveguides, such as the SiO₂ waveguide. However, for high-index-difference waveguides, like the Si waveguide, BPM struggles to give accurate results because the large refractive index difference of the Si waveguide enables large propagation angles with respect to the waveguide axis, which violates with the basic assumption of BPM. The FDTD method is a brute-force Maxwell's equations solver that depends on the finite difference discretization of Maxwell's equations in time and space domain [31]. The FDTD method can give accurate results and is universal for arbitrary structure [34]. However,

it requires a large amount of memory and computation time, which makes the FDTD method not efficient for simulating long photonic devices. The EME method is used to simulate photonic devices in this work. The EME method is a frequency domain method for solving Maxwell's equation [35]. It is fully vectorial and bidirectional, and the computational cost scales well with the device length, making it more efficient for the design and optimization of long tapers and periodic devices compared with the FDTD method [36]. What's more, the EME method does not make the slowly-varying approximation, therefore, it can provide more accurate results than the BPM.

The principle of the EME method is that the solution of Maxwell's equations in a waveguide region can be expressed using a complete basis set of eigenmodes, which is composed of the guided modes and radiative modes. The entire device is first divided into multiple sections along the propagation direction, where the waveguide structure in each section remains the same. The electric field and magnetic field in the section l can be written as

$$\begin{cases} \mathbf{E}^l(x, y, z) = \sum_{k=1}^M (a_k^l e^{j\beta_k z} + b_k^l e^{-j\beta_k z}) \mathbf{E}_k^l(x, y) \\ \mathbf{H}^l(x, y, z) = \sum_{k=1}^M (a_k^l e^{j\beta_k z} - b_k^l e^{-j\beta_k z}) \mathbf{H}_k^l(x, y), \end{cases} \quad (2.49)$$

where $\mathbf{E}_k^l(x, y)$ and $\mathbf{H}_k^l(x, y)$ are the electric field profile and the magnetic field profile of the k -th mode in section l , respectively; a_k and b_k are the amplitude of the forward and the backward wave, respectively. $\mathbf{E}_k^l(x, y)$ and $\mathbf{H}_k^l(x, y)$ can be calculated by the FDM introduced in the previous section. At the interface between adjacent sections, as shown in Fig. 2.7, Maxwell's boundary conditions are satisfied by the continuity of the tangential electric and magnetic fields. Orthogonal expansions transform the boundary condition into the matrix equation

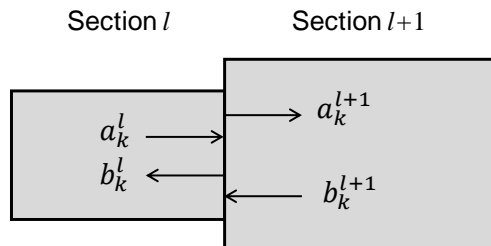


Fig. 2.7. At the interface between adjacent sections, tangential electric and magnetic fields are continuous.

2.3 Waveguide-based components

2.3.1 Silicon waveguide

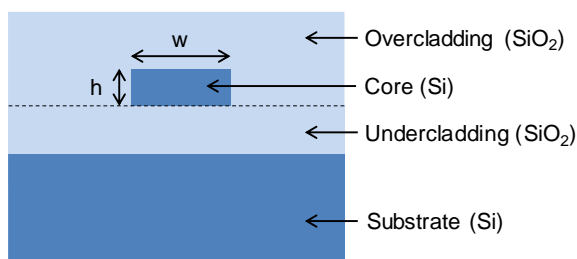


Fig. 2.8. A typical cross-sectional structure of a silicon waveguide.

A silicon waveguide is made of a Si core surrounded by a SiO₂ cladding. A typical cross-sectional structure is shown in Fig. 2.8. Because the Si layer is on top of an insulator layer, this platform is called silicon-on-insulator (SOI) platform. The high refractive index contrast between Si and SiO₂ results in strong light confinement in the core. Therefore, silicon waveguides can be sharply bent with a radius of several microns, without causing a significant bending loss [37]. The typical thickness of the Si layer (h in Fig. 2.8) is 220 nm, and the width (w in Fig. 2.8) of a single-mode waveguide is usually within 400 ~ 500 nm. Figure 2.9 shows the supported modes and their effective refractive indices as a function of w , calculated by the FDM using Lumerical Mode Solutions. The cladding is assumed to be sufficiently thick, and the refractive indices

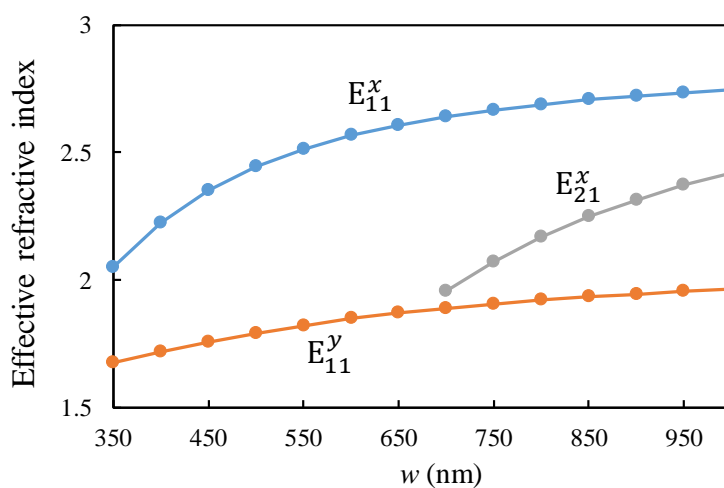


Fig. 2.9. Supported modes in Si waveguides and their effective refractive indices as a function of w . The wavelength and h are fixed at 1550 nm and 220 nm, respectively. The cladding is assumed to be sufficiently thick.

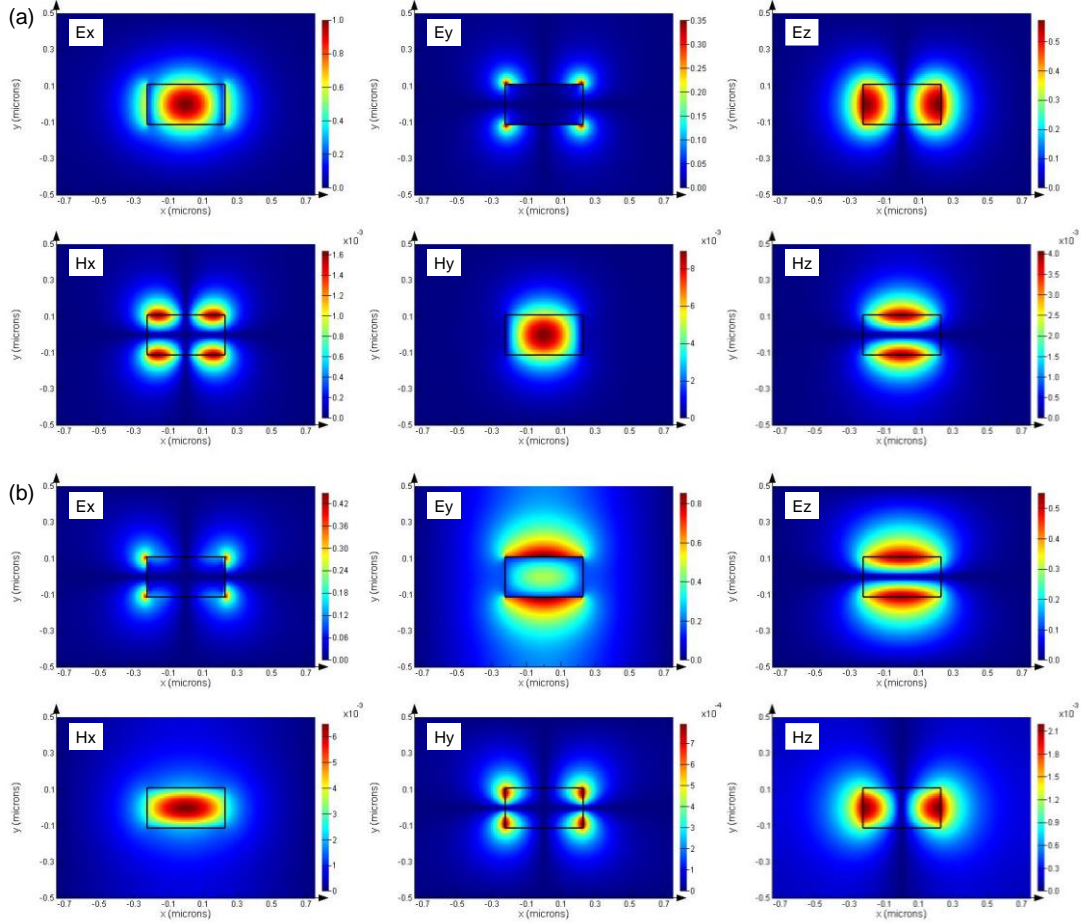


Fig. 2.10. Electric and magnetic field profiles of (a) the E_{11}^x mode and (b) the E_{11}^y mode of the Si waveguide with $w = 450$ nm and $h = 220$ nm.

of Si and SiO₂ at the wavelength of 1550 nm are 3.476 and 1.444, respectively. We can see that for TE-like modes (E_{pq}^x modes), the 2nd-order mode appears from ~ 700 -nm w . Note that this boundary is not rigorously defined, the E_{21}^x mode may still be supported by a waveguide of a smaller w , but with a larger propagation loss. Figure 2.10 shows the electric and magnetic field profiles of the E_{11}^x and E_{11}^y mode of the waveguide with $w = 450$ nm and $h = 220$ nm. As predicted in Section 2.1.2, in the transverse plane, E_x and H_y are the predominant components in the E_{11}^x mode, while E_y and H_x are the predominant components in the E_{11}^y mode.

The absorption of the light at telecom wavelengths (~ 1.55 μm) in silicon is low enough to be ignored. The propagation loss of a Si waveguide is mainly attributed to the scattering loss caused by the roughness of the core sidewall [38]. For Si single-mode channel waveguides, the propagation losses of the TE-like mode (E_{11}^x mode) have been reported to be 0.5~3.6 dB/cm at the wavelength near 1.55 μm [39, 40, 41]. Minimizing the

optical field overlap with the core sidewall, for instance, using a rib-shape core [42], can reduce the propagation loss. Sharp bends are easily achievable because of the strong light confinement in the Si core. The loss per 90° bend has been reported to be 0.086 ± 0.005 dB at the 1.5- μm wavelength for a bending radius of 1 μm [40]. The low bending loss of the Si waveguide has enabled Si microring resonators with 1.5- μm radii [43].

2.3.2 Directional coupler

A directional coupler is comprised of two closely-spaced waveguides where the light can transfer from one to the other. The coupling results from the overlap of evanescent waves of the two waveguides in the cladding region. The amount of transferred power depends on the distance of the waveguides, the mode penetration into the cladding, and the interaction length [44]. In this section, we analyze the directional coupler based on channel waveguides using the perturbation method.

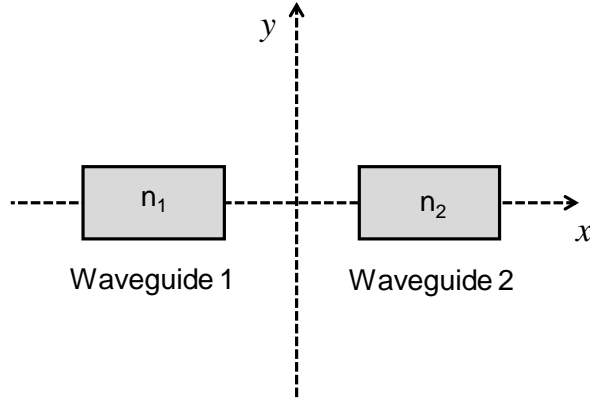


Fig. 2.11. A directional coupler comprised of two channel waveguides.

We consider the directional coupler shown in Fig. 2.11. The eigen modes of each waveguide ($\tilde{\mathbf{E}}_1, \tilde{\mathbf{H}}_1, \tilde{\mathbf{E}}_2$ and $\tilde{\mathbf{H}}_2$) satisfy

$$\begin{cases} \nabla \times \tilde{\mathbf{E}}_a = -j\omega\mu_0\tilde{\mathbf{H}}_a \\ \nabla \times \tilde{\mathbf{H}}_a = j\omega\varepsilon_0 n_p^2 \tilde{\mathbf{E}}_a, \end{cases} \quad (a = 1, 2) \quad (2.54)$$

where $n_a(x, y)$ represents the refractive index distribution of each waveguide. If the waveguides are not strongly coupled, the electromagnetic field in the directional coupler can be considered as a linear combination of the eigen modes of each waveguide:

$$\begin{cases} \tilde{\mathbf{E}} = A\tilde{\mathbf{E}}_1 + B\tilde{\mathbf{E}}_2 \\ \tilde{\mathbf{H}} = A\tilde{\mathbf{H}}_1 + B\tilde{\mathbf{H}}_2. \end{cases} \quad (2.55)$$

Because $\tilde{\mathbf{E}}$ and $\tilde{\mathbf{H}}$ also satisfy the Maxwell's equations, we can obtain

$$(\mathbf{u}_z \times \tilde{\mathbf{E}}_1) \frac{dA}{dz} + (\mathbf{u}_z \times \tilde{\mathbf{E}}_2) \frac{dB}{dz} = 0 \quad (2.56)$$

$$\begin{aligned} (\mathbf{u}_z \times \tilde{\mathbf{H}}_1) \frac{dA}{dz} - j\omega\varepsilon_0(n^2 - n_1^2)A\tilde{\mathbf{E}}_1 + (\mathbf{u}_z \times \tilde{\mathbf{H}}_2) \frac{dB}{dz} \\ - j\omega\varepsilon_0(n^2 - n_2^2)B\tilde{\mathbf{E}}_2 = 0, \end{aligned} \quad (2.57)$$

where $n(x, y)$ is the refractive index distribution of the entire region and \mathbf{u}_z is a unit vector along the $+z$ direction. Substitute Eq. (2.56) and (2.57) into the integral equation

$$\int_{-\infty}^{+\infty} \int_{-\infty}^{+\infty} [\tilde{\mathbf{E}}_a^* \cdot (2.56) - \tilde{\mathbf{H}}_a^* \cdot (2.57)] dx dy = 0 \quad (2.58)$$

and separate the z -axis dependency, we obtain

$$\frac{dA}{dz} + c_{12} \frac{dB}{dz} e^{-j(\beta_2 - \beta_1)z} + j\chi_1 A + j\kappa_{12} B e^{-j(\beta_2 - \beta_1)z} = 0 \quad (2.59)$$

$$\frac{dB}{dz} + c_{21} \frac{dA}{dz} e^{j(\beta_2 - \beta_1)z} + j\chi_2 B + j\kappa_{21} A e^{j(\beta_2 - \beta_1)z} = 0, \quad (2.60)$$

where β_1 and β_2 are the propagation constants,

$$\kappa_{ab} = \frac{\omega\varepsilon_0 \int_{-\infty}^{+\infty} \int_{-\infty}^{+\infty} (n^2 - n_b^2) \mathbf{E}_a^* \mathbf{E}_b dx dy}{\int_{-\infty}^{+\infty} \int_{-\infty}^{+\infty} \mathbf{u}_z (\mathbf{E}_a^* \times \mathbf{H}_a + \mathbf{E}_a \times \mathbf{H}_a^*) dx dy} \quad (2.61)$$

$$c_{ab} = \frac{\int_{-\infty}^{+\infty} \int_{-\infty}^{+\infty} \mathbf{u}_z (\mathbf{E}_a^* \times \mathbf{H}_b + \mathbf{E}_b \times \mathbf{H}_a^*) dx dy}{\int_{-\infty}^{+\infty} \int_{-\infty}^{+\infty} \mathbf{u}_z (\mathbf{E}_a^* \times \mathbf{H}_a + \mathbf{E}_a \times \mathbf{H}_a^*) dx dy} \quad (2.62)$$

$$\chi_i = \frac{\omega\varepsilon_0 \int_{-\infty}^{+\infty} \int_{-\infty}^{+\infty} (n^2 - n_i^2) \mathbf{E}_i^* \mathbf{E}_i dx dy}{\int_{-\infty}^{+\infty} \int_{-\infty}^{+\infty} \mathbf{u}_z (\mathbf{E}_i^* \times \mathbf{H}_i + \mathbf{E}_i \times \mathbf{H}_i^*) dx dy} \quad (i = 1, 2). \quad (2.63)$$

κ_{ab} is the mode coupling coefficient between the two waveguides, c_{ab} is the excitation efficiency at the interface. The magnitude of χ_i is significantly smaller than that of κ_{ab} [26]. From Eq. (2.62) and (2.63), we can derive

$$c_{12} = c_{21}^* \quad (2.64)$$

$$\chi_i = \chi_i^*. \quad (2.65)$$

The optical power in the directional coupler is given by

$$\begin{aligned}
P &= \frac{1}{2} \int_{-\infty}^{+\infty} \int_{-\infty}^{+\infty} (\tilde{\mathbf{E}} \times \tilde{\mathbf{H}}^*) \mathbf{u}_z dx dy \\
&= \frac{1}{2} [|A|^2 + |B|^2 + A^* B c_{12} e^{-j2\delta z} + AB^* c_{12}^* e^{j2\delta z}],
\end{aligned} \tag{2.66}$$

where $\delta = (\beta_2 - \beta_1)/2$. The optical power in lossless waveguides is constant:

$$\frac{dP}{dz} = 0. \tag{2.67}$$

Substitute Eq. (2.59-2.60) and (2.66) into Eq. (2.67), we can obtain

$$A^* B (\kappa_{21}^* - \kappa_{12} - 2\delta c_{12}) e^{-j2\delta z} = AB^* (\kappa_{21} - \kappa_{12}^* - 2\delta c_{12}^*) e^{j2\delta z}. \tag{2.68}$$

Because Eq. (2.68) needs be satisfied for any z , we have

$$\kappa_{21}^* = \kappa_{12} + 2\delta c_{12}. \tag{2.69}$$

If the propagation constants of the two waveguides are the same ($\beta_2 = \beta_1$),

$$\kappa_{21}^* = \kappa_{12} = \kappa. \tag{2.70}$$

Under the assumption that c_{ab} and χ_i can be neglected, we can obtain the following equations from Eq. (2.59) and (2.60):

$$\frac{dA}{dz} = -j\kappa_{12} B e^{-j(\beta_2 - \beta_1)z} \tag{2.71}$$

$$\frac{dB}{dz} = -j\kappa_{21} A e^{j(\beta_2 - \beta_1)z}. \tag{2.72}$$

In a codirectional coupler where the light is propagating along a single direction, $\kappa_{12} = \kappa_{21} = \kappa$. The solutions of Eq. (2.71) and (2.72) for a codirectional coupler are

$$A(z) = \left\{ \left[\cos(\rho z) + j \frac{\delta}{\rho} \sin(\rho z) \right] A(0) - j \frac{\kappa}{\rho} \sin(\rho z) B(0) \right\} e^{-j\delta z} \tag{2.73}$$

$$B(z) = \left\{ -j \frac{\kappa}{\rho} \sin(\rho z) A(0) + \left[\cos(\rho z) - j \frac{\delta}{\rho} \sin(\rho z) \right] B(0) \right\} e^{j\delta z}, \tag{2.74}$$

where

$$\rho = \sqrt{\kappa^2 + \delta^2}. \tag{2.75}$$

If the light is only in the waveguide 1 at $z = 0$, then the optical power in each waveguide at other positions are given by

$$P_1(z) = 1 - F \sin^2(\rho z) \tag{2.76}$$

$$P_2(z) = F \sin^2(\rho z), \tag{2.77}$$

where F represents the maximum power coupling efficiency and is defined by

$$F = \left(\frac{\kappa}{\rho}\right)^2 = \frac{1}{1 + (\delta/\kappa)^2}. \quad (2.78)$$

From Eq. (2.77), we can see that the maximum power transferring occurs at

$$z = \frac{\pi}{2\rho} = \frac{\pi}{2\sqrt{\kappa^2 + \delta^2}}(2m + 1) \quad (m = 0, 1, 2, \dots). \quad (2.79)$$

The coupling length is defined as the distance between two adjacent maximum power transferring points and is given by

$$L_c = \frac{\pi}{2\sqrt{\kappa^2 + \delta^2}} \quad (2.80)$$

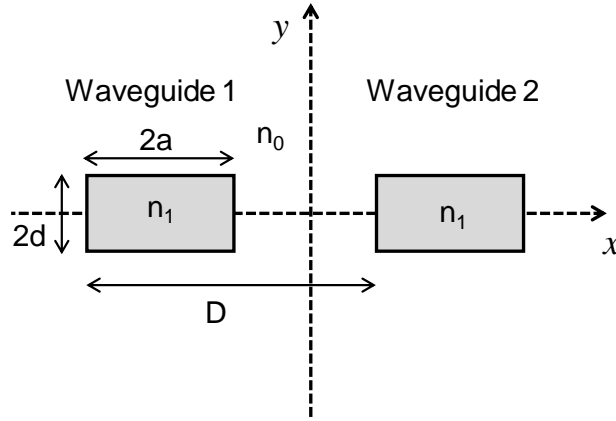


Fig. 2.12. A directional coupler comprised of two identical channel waveguides.

For the directional coupler shown in Fig. 2.12, where the two waveguides are the same, the mode coupling coefficient for the E_{11}^x mode is expressed by

$$\kappa = \frac{(k_x a)^2 (\gamma_x a)^2 \sqrt{2\Delta}}{a v^3 (1 + \gamma_x a)} e^{-\gamma_x (D-2a)}, \quad (2.81)$$

where

$$\Delta = \frac{n_1^2 - n_0^2}{2n_1^2} \quad (2.82)$$

$$v = k n_1 a \sqrt{2\Delta}, \quad (2.83)$$

k_x and γ_x can be calculated from Eq. (2.36) and (2.37).

2.3.3 Multimode interference (MMI) coupler

An MMI coupler is a coupler that can split the input light based on the self-imaging effect in a multimode waveguide [45]. MMI couplers have been widely used in optical switches [46, 47, 48], polarization splitters [49, 50] and sensors [51, 52, 53]. In this section, we analyze the mechanism and input-output relations of an $N \times N$ MMI coupler.

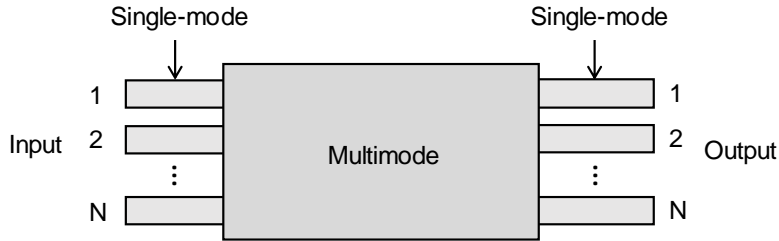


Fig. 2.13. Schematic of an $N \times N$ MMI coupler.

An MMI coupler consists of single-mode input and output waveguides and a multimode waveguide section, as shown in Fig. 2.13. The input light is decomposed into the eigenmodes of the multimode waveguide. In theory, we need an infinite number of guided modes in the multimode waveguide for complete decomposition. However, for strongly-confined structures, most of the input light can be decomposed into the guided modes and the remaining components are negligible [54]. The profiles of several guided modes in a multimode waveguide are shown in Fig. 2.14. For the convenience of following analyses, an antisymmetric virtual section is added to the left of the real waveguide and the section $[-W, W]$ is assumed to extend periodically along the whole x axis, where W is the width of the multimode waveguide. The guided eigenmodes of a strongly-confined multimode waveguide have the form

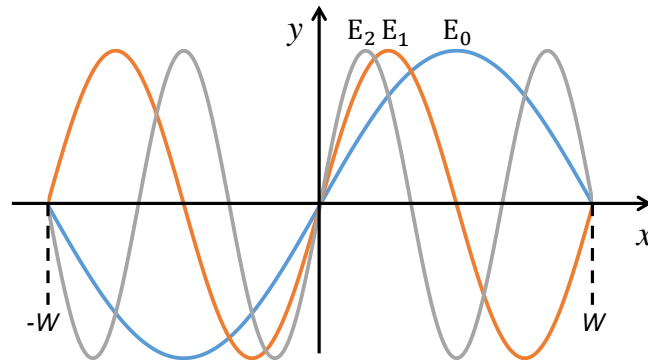


Fig. 2.14. Profiles of several guided modes in a multimode waveguide. An antisymmetric virtual section is added to the left of the real waveguide section $[0, W]$. The section $[-W, W]$ is assumed to extend periodically along the whole x axis.

$$E_i(x) = \sin \left[\pi(i+1) \frac{x}{W} \right] \quad (i = 0, 1, 2, \dots). \quad (2.84)$$

The propagation constant of each mode β_i can be calculated by the paraxial approximation:

$$\beta_i \cong nk_0 - \frac{k_{xi}^2}{2nk_0} = nk_0 - \frac{\pi^2(i+1)^2}{2nk_0W^2}, \quad (2.85)$$

where k_0 is angular wavenumber in vacuum, k_{xi} is the lateral wavenumber, and n is the refractive index of the core. From Eq. (2.85), we obtain the beat length of the two lowest-order modes

$$L_c = \frac{\pi}{\beta_0 - \beta_1} \cong \frac{2nk_0W^2}{3\pi}. \quad (2.86)$$

Next, we analyze the self-imaging effects in the multimode waveguide section. An input field profile $f_{\text{in}}(x)$ will be decomposed into the guided modes of the multimode waveguide:

$$f_{\text{in}}(x) = \sum_i a_i E_i(x), \quad (2.87)$$

where $E_i(x)$ is the i -th mode of the multimode waveguide, a_i is the mode excitation efficient and can be calculated from

$$a_i = \frac{2}{W} \int_0^W f_{\text{in}}(x) E_i^*(x) dx. \quad (2.88)$$

The field profile at the distance L is then given by

$$f(x, L) = \sum_i a_i E_i(x) e^{j(\omega t - \beta_i L)}. \quad (2.89)$$

Ignore the time dependency in Eq. (2.89) and set the absolute phase of the fundamental mode to zero, Equation (2.89) can be rewritten as

$$f(x, L) = \sum_i a_i E_i(x) e^{j(\beta_0 - \beta_i)L} = \sum_i a_i E_i(x) e^{j \frac{i(i+2)}{3L_c} L}. \quad (2.90)$$

From Eq. (2.90), it can be seen that the field $f(x, L)$ will be a reproduction of $f_{\text{in}}(x)$ under certain circumstances [55]. If

$$e^{j \frac{i(i+2)}{3L_c} L} = 1, \quad (2.91)$$

the image is a direct replica of the input field; if

$$e^{j\frac{i(i+2)}{3L_c}L} = (-1)^i, \quad (2.92)$$

the image is mirrored with respect to the plane $x = W/2$. Equation (2.91) and (2.92) are satisfied when

$$L = 3mL_c \quad (m = 0, 1, 2, \dots), \quad (2.93)$$

where an even and odd m corresponds to a direct and mirrored image of the input field, respectively.

At the positions

$$L = \frac{3mL_c}{2} \quad (m = 1, 3, 5, \dots), \quad (2.94)$$

the field $f(x, L)$ becomes

$$\begin{aligned} f(x, L) &= \sum_i a_i E_i(x) e^{j\frac{i(i+2)}{2}m\pi} = \sum_{\text{even } i} a_i E_i(x) + \sum_{\text{odd } i} (-1)^i a_i E_i(x) \\ &= \frac{1 + (-j)^m}{2} f(x, 0) + \frac{1 - (-j)^m}{2} f(W - x, 0) \quad (m = 1, 3, 5, \dots). \end{aligned} \quad (2.95)$$

Equation (2.95) represents a pair of images of the input field with amplitudes of $1/\sqrt{2}$, as illustrated in Fig. 2.15.

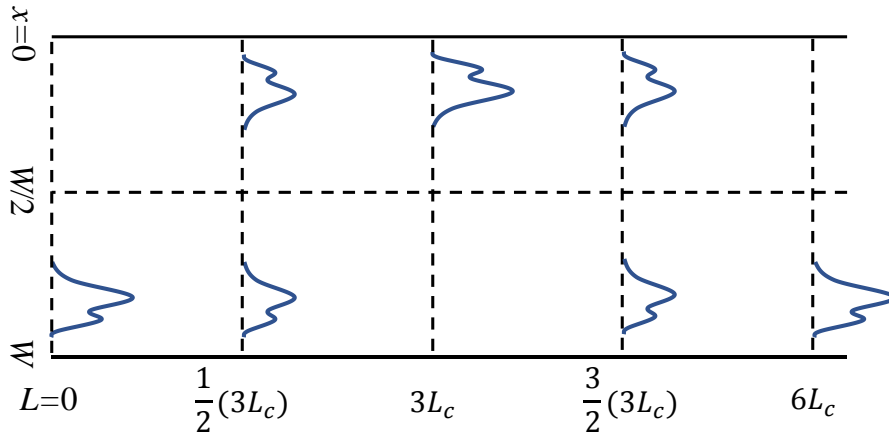


Fig. 2.15. Self-imaging effect inside a multimode waveguide.

We further consider the case of N -fold images. At the positions

$$L_N = \frac{3L_c}{N}, \quad (2.96)$$

the field is given by

$$f(x, L) = \sum_i a_i E_i(x) e^{-j\beta_i L N} = \sum_i a_i B_i E_i(x), \quad (2.97)$$

where

$$B_i = e^{-j\beta_0 L N + j\frac{i(i+2)}{N}\pi}. \quad (2.98)$$

According to [54], Equation (2.97) can be rewritten as

$$f(x, L) = \frac{1}{C} \sum_{k=0}^{N-1} f_{\text{in}}(x - x_k) e^{j\varphi_k}, \quad (2.99)$$

where

$$x_k = (2k - N) \frac{W}{N} \quad (2.100)$$

$$\varphi_k = k(N - k) \frac{\pi}{N} \quad (2.101)$$

$$C = \sqrt{N} e^{j[\beta_0 L N + \frac{\pi}{N} + \frac{\pi}{4}(N-1)]}. \quad (2.102)$$

Equation (2.99) represents N -fold images with equal amplitudes. The position and phase of the k -th image are given by x_k and φ_k , respectively. From Eq. (2.99) – (2.102), we can obtain the transfer matrix \mathbf{M} for electric fields of the $N \times N$ MMI coupler shown in Fig. 2.13. Each element of \mathbf{M} is given by

$$\mathbf{M}_{nm} = \begin{cases} \frac{1}{\sqrt{N}} e^{j\pi[1 + \frac{1}{4N}(n-N-1+m)(3N-n+1-m)]} & (N - m + n) \text{ is odd} \\ \frac{1}{\sqrt{N}} e^{j\pi[\frac{1}{4N}(n+N-m)(N-n+m)]} & (N - m + n) \text{ is even,} \end{cases} \quad (2.103)$$

where \mathbf{M}_{nm} represents the coupling ratio of the electric field from the input port m to the output port n .

The above analyses show the operation principle and give some basic properties of an ideal MMI coupler. In real devices, the insertion loss, device length, and operation bandwidth are three important parameters that characterize an MMI coupler. The insertion loss originates from the propagation loss and the coupling loss at the interface

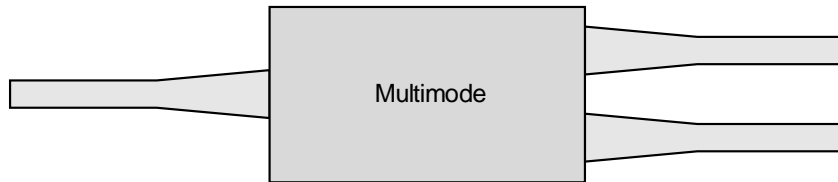


Fig. 2.16. A 1×2 MMI coupler that uses tapers to reduce the insertion loss.

between the single-mode and multimode waveguide. Waveguide tapers can be used to reduce the coupling loss at the interface [56, 57, 58], as shown in Fig. 2.16. A 2×2 MMI coupler with an insertion loss of 0.15 ± 0.01 dB has been reported in [59].

The MMI length can be reduced by using tapered multimode waveguide sections [60, 61, 62]. Figure 2.17 shows the schematic of a parabolically tapered $N \times N$ MMI coupler. The decrease in the average waveguide width leads to a reduction in the imaging length [60]. In the case of 2×2 MMI couplers, a length reduction up to a factor of 3~4 can be expected with a proper taper design [62].

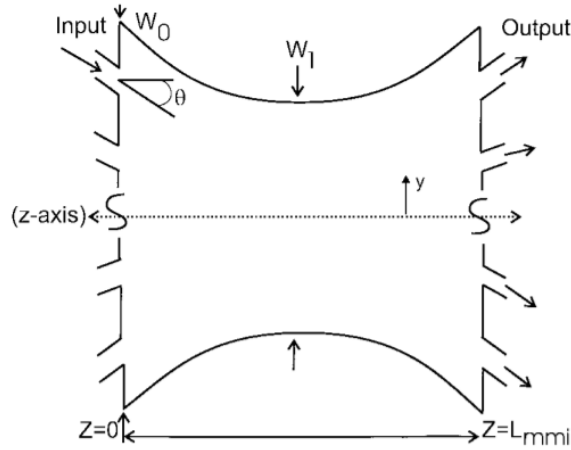


Fig. 2.17. An $N \times N$ MMI coupler that uses a parabolically tapered structure to reduce the length [60].

2.3.4 Phase shifter

As the name implies, a phase shifter is a component that shifts the phase of the light passing through it. The underlying mechanism is to change the refractive index of the optical waveguide, which can be realized through the thermo-optic effect, the electro-optic effect or the plasma dispersion effect.

The electro-optic effect enables modulation speeds above 10 GHz [63, 64, 65] and has been widely used in bulky free-space light modulators. An electro-optic phase modulator contains a nonlinear crystal. The refractive index of the nonlinear crystal is modulated by an external electric field, based on the linear electro-optic effect (also known as the Pockels effect). Typical nonlinear crystal materials used in electro-optic modulators include LiNbO_3 (lithium niobate), BTO (Barium titanate), KTP (potassium titanyl phosphate), BBO (beta-barium borate), special polymers, and so on. Although great efforts have been devoted to developing Pockels-effect-based phase shifters on

the SOI platform [66, 67, 68], it is hard to simultaneously achieve a high modulation efficiency and the CMOS process compatibility, because of the small electro-optic coefficient of silicon [14]. Therefore, phase shifters based on the thermo-optic effect or the plasma dispersion effect dominate on the SOI platform.

Table 2.1 Thermo-optic coefficients of various materials

Material	dn/dT (K^{-1})	Temperature (K)	Wavelength (nm)	Reference
Si	1.8×10^{-4}	300	1550	[69]
SiO ₂	1.178×10^{-5}	243~343	1550	[70]
SiON	1.84×10^{-5}	301	1550	[71]
Si ₃ N ₄	2.45×10^{-5}	300	1550	[72]

The thermo-optic coefficient (dn/dT) of silicon is $\sim 10^{-8} K^{-1}$ at 300 K, which is greater than those of SiO₂, SiON, Si₃N₄, as listed in Table 2.1. Therefore, thermo-optic phase shifters for silicon waveguides are more efficient than those for waveguides made of other materials. A thermo-optic phase shifter uses either an external thin-film heater

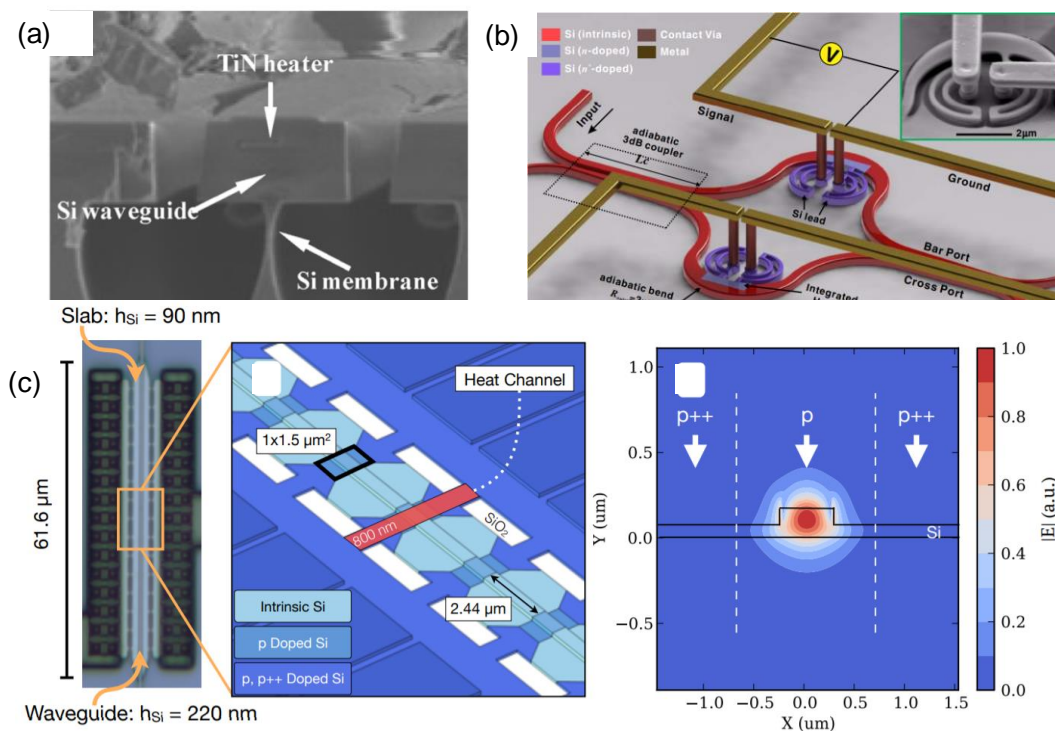


Fig. 2.16. Examples of thermo-optic silicon phase shifters. (a) A TiN heater on top of the silicon layer [73]. (b) Doped silicon leads heat the silicon core directly [74]. (c) Partly-doped silicon ridge waveguide [75].

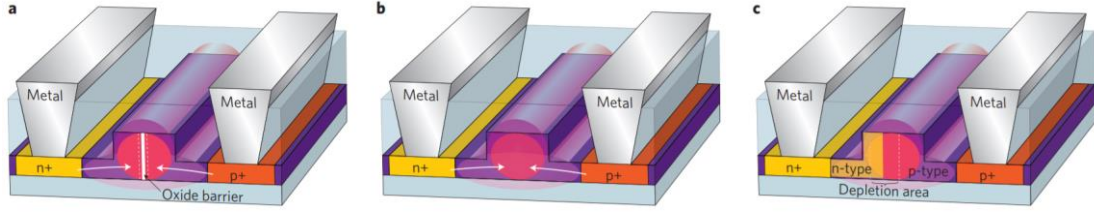


Fig. 2.17. (a) Carrier-accumulation-based phase shifter. The oxide barrier in the waveguide is used to form a capacitor structure. (b) Carrier-injection-based phase shifter. Forward bias voltage is applied to inject free carriers into the waveguide. (c) Carrier-depletion-based phase shifter. Reverse bias voltage is applied to deplete free carriers in the waveguide [14].

on top of the silicon layer or doped silicon regions that connect directly to the silicon core to heat the waveguide, as shown in Fig. 2.16 [73, 74, 75]. Typical power consumptions of thermo-optic phase shifters range from 10 mW to 50 mW for a π -shift shift [74, 75, 76].

Phase shifters based on the plasma dispersion effect electrically manipulate the free carrier concentrations in the waveguide to change the refractive index. According to the device structure and the applied bias voltage, these phase shifters can be divided into carrier-accumulation, carrier-injection, and carrier-depletion-based phase shifters, as shown in Fig. 2.17 [14]. Plasma-dispersion-based phase shifters enable high-speed modulations (> 10 GHz) [77, 78, 79], but usually have larger insertion losses and long device lengths than thermo-optic phase shifters.

2.3.5 Mach-Zehnder interferometer

Mach-Zehnder interferometers (MZIs) are widely used in optical amplitude modulators [80, 81], sensors [82, 83, 84, 85], optical metrologies [86, 87] and quantum applications [88, 89, 90, 91, 92]. A tunable MZI consists of two 50:50 optical couplers and a phase shifter on one of the two arms between the couplers. The complex transfer matrix of an ideal 50:50 optical coupler is

$$\frac{1}{\sqrt{2}} \begin{pmatrix} 1 & j \\ j & 1 \end{pmatrix}. \quad (2.104)$$

Therefore, the complex transfer matrix of a tunable MZI is given by

$$\mathbf{T}_{\text{MZI}} = \frac{1}{2} \begin{pmatrix} 1 & j \\ j & 1 \end{pmatrix} \begin{pmatrix} e^{j\theta} & 0 \\ 0 & 1 \end{pmatrix} \begin{pmatrix} 1 & j \\ j & 1 \end{pmatrix} = j e^{j\frac{\theta}{2}} \begin{pmatrix} \sin \frac{\theta}{2} & \cos \frac{\theta}{2} \\ \cos \frac{\theta}{2} & -\sin \frac{\theta}{2} \end{pmatrix}, \quad (2.105)$$

where θ is the phase difference between the two arms. Depending on the path length differences of the two arms, MZIs can be categorized as symmetric MZIs and

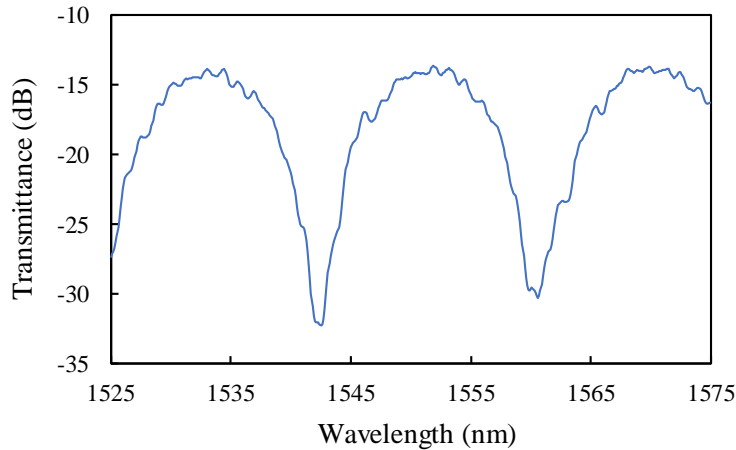


Fig. 2.18. Measured transmission spectra of an asymmetric MZI with $\Delta L = 30 \mu\text{m}$. The free spectral range (FSR) of this MZI is $\sim 19 \text{ nm}$.

asymmetric MZIs, where the two path lengths are the same in symmetric MZIs and are different in asymmetric MZIs. In an asymmetric MZI, the phase difference θ is a function of the wavelength and the path length difference ΔL . Figure 2.18 shows the measured transmission spectra of an asymmetric MZI with $\Delta L = 30 \mu\text{m}$. The free spectral range (FSR) of this MZI is $\sim 19 \text{ nm}$.

An important parameter of a tunable MZI is the extinction ratio, which is the difference between the maximum transmittance and the minimum transmittance. Larger extinction ratios can be obtained by reducing the insertion loss of the phase shifter and optimizing the 50:50 optical couplers. For example, an MZI with a 66-dB extinction ratio has been reported in [17]. In addition, an additional tunable MZI can be inserted to compensate for the fabrication imperfections, as proposed in [93]. An MZI with a 60-dB extinction ratio has been reported based on this method [94].

2.3.6 Spot-size converter

The mode field diameter of a single-mode silicon waveguide is significantly smaller than that of a standard single-mode optical fiber. Significant coupling losses can occur due to the mode mismatching. The spot-size converter can be used to reduce the coupling loss between silicon waveguides and optical fibers by enlarging the mode field diameter of the waveguide.

Various structures have been proposed and demonstrated to realize low-loss spot-size converters [95, 96, 97, 98, 99]. A typical structure is the inverse taper, as shown in Fig. 2.19. The optical mode gradually expands outside the core region due to the weaker confinement caused by the gradually decreasing waveguide width. The mode diameter

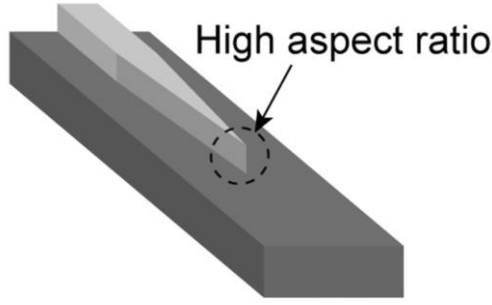


Fig. 2.19. Typical structure of the spot-size converter based on an inverse taper [97].

can be expanded to several microns by the spot-size converter, thus significantly improving the coupling efficiency between a silicon waveguide and an optical fiber.

2.4 Multi-plane light conversion

This section introduces the theory of MPLC and is mainly based on [23]. Suppose a beam of light with a monochromatic wavelength (λ) and polarization is propagating along the z -axis. The transverse mode profile $E(x, y)$ can be decomposed in the transverse electromagnetic (TEM) mode basis:

$$E(x, y) = \sum_{m \in \mathbb{N}, n \in \mathbb{N}} a_{mn} \text{TEM}_{mn}(x, y), \quad (2.106)$$

where a_{mn} is the complex coefficient of the TEM_{mn} mode. A phase plate transforms the transverse profile into

$$e^{j\phi(x,y)} E(x, y), \quad (2.107)$$

where

$$\phi(x, y) = 2\pi \frac{z(x, y)}{\lambda}. \quad (2.108)$$

Within the region of interest, the transverse profile can be discretized using a pixel basis: the region is discretized into $N \times N$ pixels, and the electric field at pixel (i, j) is represented by E_{ij} . As long as the pixels are small enough, this discretization can adequately describe $E(x, y)$. E_{ij} can then be reorganized row by row into a single vector \mathbf{E} , with each element corresponding to a pixel in the region. $e^{j\phi(x,y)}$ now can be described by a matrix \mathbf{U}_ϕ :

$$\mathbf{U}_\phi = \begin{pmatrix} e^{j\phi_1} & 0 & \dots & 0 \\ 0 & e^{j\phi_2} & \dots & 0 \\ \vdots & \vdots & \ddots & \vdots \\ 0 & 0 & \dots & e^{j\phi_{N^2}} \end{pmatrix}. \quad (2.109)$$

A lens with a focal length of f_0 can perform the Fourier transformation by a simple free-space light propagation from the front focal plane to the back focal plane. This transformation can also be discretized using a matrix \mathbf{U}_{FT} . \mathbf{U}_{FT} is as close as possible to the discrete Fourier transform (DFT) matrix as long as the pixel number N_{pix} and pixel size Δ_{pix} satisfy the condition:

$$N_{\text{pix}}\Delta_{\text{pix}}^2 = 2\pi\lambda f_0. \quad (2.110)$$

According to [100], it is possible to create the matrix $\mathbf{T}_{ij}(\theta)$ for any i, j , and θ using a succession of \mathbf{U}_{FT} and \mathbf{U}_ϕ , where

$$\mathbf{T}_{ij}(\theta) = \begin{pmatrix} 1 & 0 & \dots & 0 & \dots & 0 & \dots & 0 \\ 0 & 1 & \dots & 0 & \dots & 0 & \dots & 0 \\ \vdots & \vdots & \ddots & \vdots & \dots & \vdots & \dots & \vdots \\ 0 & 0 & \dots & \cos(\theta) & \dots & \sin(\theta) & \dots & 0 \\ \vdots & \vdots & \vdots & \vdots & \dots & 1 & \dots & \vdots \\ 0 & 0 & \dots & -\sin(\theta) & \dots & \cos(\theta) & \dots & 0 \\ \vdots & \vdots & \vdots & \vdots & \dots & \vdots & \dots & \vdots \\ 0 & 0 & \dots & 0 & \dots & 0 & \dots & 0 \\ 0 & 0 & \dots & 0 & \dots & 0 & \dots & 1 \end{pmatrix}, \quad (2.111)$$

i and j are the row and column numbers of the $\sin(\theta)$ and $\cos(\theta)$ terms. It is known that a succession of $\mathbf{T}_{ij}(\theta)$ and \mathbf{U}_ϕ can build any unitary matrix [13, 101]. Therefore, a finite sequence of \mathbf{U}_{FT} and \mathbf{U}_ϕ is sufficient to build any unitary matrix. Experimentally, the number of required sequences depends on the required transformation fidelity.

2.5 Summary

In this chapter, we first introduced the fundamental theories of photonic integrated circuits (PICs), including the analysis of optical waveguides, several simulation methods, and waveguide-based components. The waveguide analysis gives the basic properties of optical waveguides, especially the concept of polarization and mode. The finite difference method (FDM) is suitable for complicated waveguide analysis and the eigenmode expansion method (EME) is suitable for simulating passive photonic devices with periodic structures. The operation principles of MMI coupler, directional

coupler, phase shifter, Mach-Zehnder interferometer (MZI), and spot-size converter are explained in detail. All these components will be used in this work.

Next, we introduced the theory of multi-plane light conversion (MPLC). Any unitary transformation can be realized by a finite sequence of phase plate and Fourier transformation. In the matrix representation, the phase plate is represented by a unitary matrix with only diagonal elements, the Fourier transformation is represented by the DFT matrix. The diagonal unitary matrix is responsible for changing the phases and the DFT matrix is responsible for mixing both the amplitudes and phases. From this point of view, other unitary matrices that can mix both the amplitudes and phases may also work.

Chapter 3 Wideband integrated OUC using MMI couplers

In this chapter, we first propose a wideband integrated OUC using MMI couplers, then present the design and device characterization of a 3×3 integrated OUC based on the proposed structure.

3.1 Proposed structure

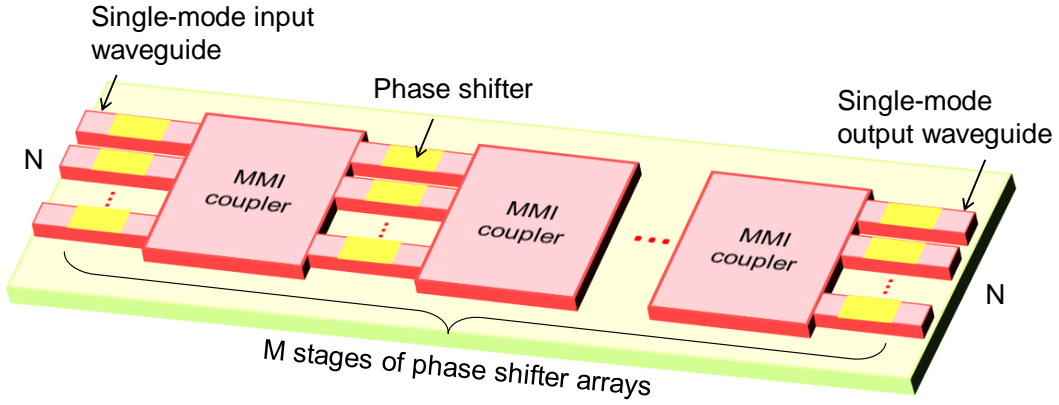


Fig. 3.1. The proposed OUC structure for wideband operations.

The schematic structure is shown in Fig. 3.1, which consists of series of $N \times N$ MMI couplers and phase shifter arrays. The $N \times N$ transfer matrix \mathbf{T} , which describes the coupling of the electric fields from the input ports to the output ports, is expressed as

$$\mathbf{T} = \Phi_M \cdot \mathbf{M} \cdot \Phi_{M-1} \cdots \mathbf{M} \cdot \Phi_1, \quad (3.1)$$

where M is the total number of phase shifter stages, \mathbf{M} and Φ_i are the transfer matrices of MMI couplers and the i -th stage phase shifter array, respectively. Φ_i is a unitary matrix with non-zero diagonal elements and \mathbf{M} is a unitary matrix when neglecting the path-dependent coupling loss [54]. Similar to the principle of MPLC, it is possible to set \mathbf{T} to any unitary matrix by configuring the phase shifters. Because of the symmetric structure and relatively wide bandwidths of MMI couplers, we can expect wider operation bandwidths than those based on the Reck's scheme.

3.2 Numerical analysis

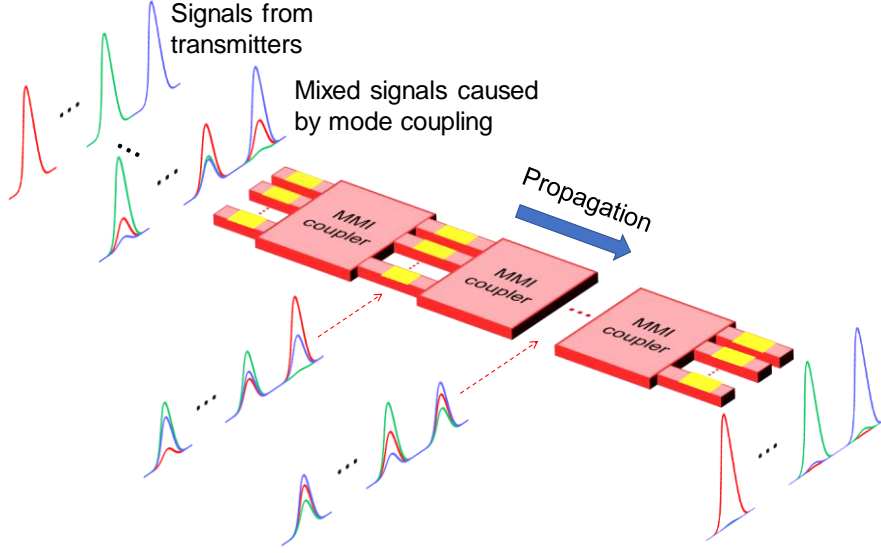


Fig. 3.2. Schematic of applying the OUC into mode unscrambling.

Numerical simulations are performed to verify the validity of this scheme. We evaluate the difference between the desired matrix \mathbf{T} and the generated matrix \mathbf{T}' by calculating the mean squared error (MSE):

$$\text{MSE} = \frac{1}{N^2} \sum_{i=1, j=1}^{N, N} |T'_{ij} - T_{ij}|^2, \quad (3.2)$$

where i and j are the row and column number, respectively.

In the case of applying the OUC into mode unscrambling, as illustrated in Fig. 3.2, the modal crosstalk is a better performance indicator, which is given by

$$\begin{aligned} \mathbf{C} &= (C_{ij}) = \mathbf{T}'\mathbf{U}, \\ \text{Crosstalk} &= \max(|C_{ij}/C_{ii}|^2) \quad (i \neq j), \end{aligned} \quad (3.3)$$

where \mathbf{U} is a unitary matrix that represents the mode coupling effect and \mathbf{T}' is generated matrix to unscramble the coupled modes.

3.2.1 Simulated annealing algorithm

In order to set the transfer matrix \mathbf{T} to any desired unitary matrix, all the phase shifts need be properly configured. In this work, we use the simulated annealing algorithm to optimize the phase shifters. Simulated annealing is a stochastic method that can be used to approximate the global optimum of a function. Its name originates from the analogy

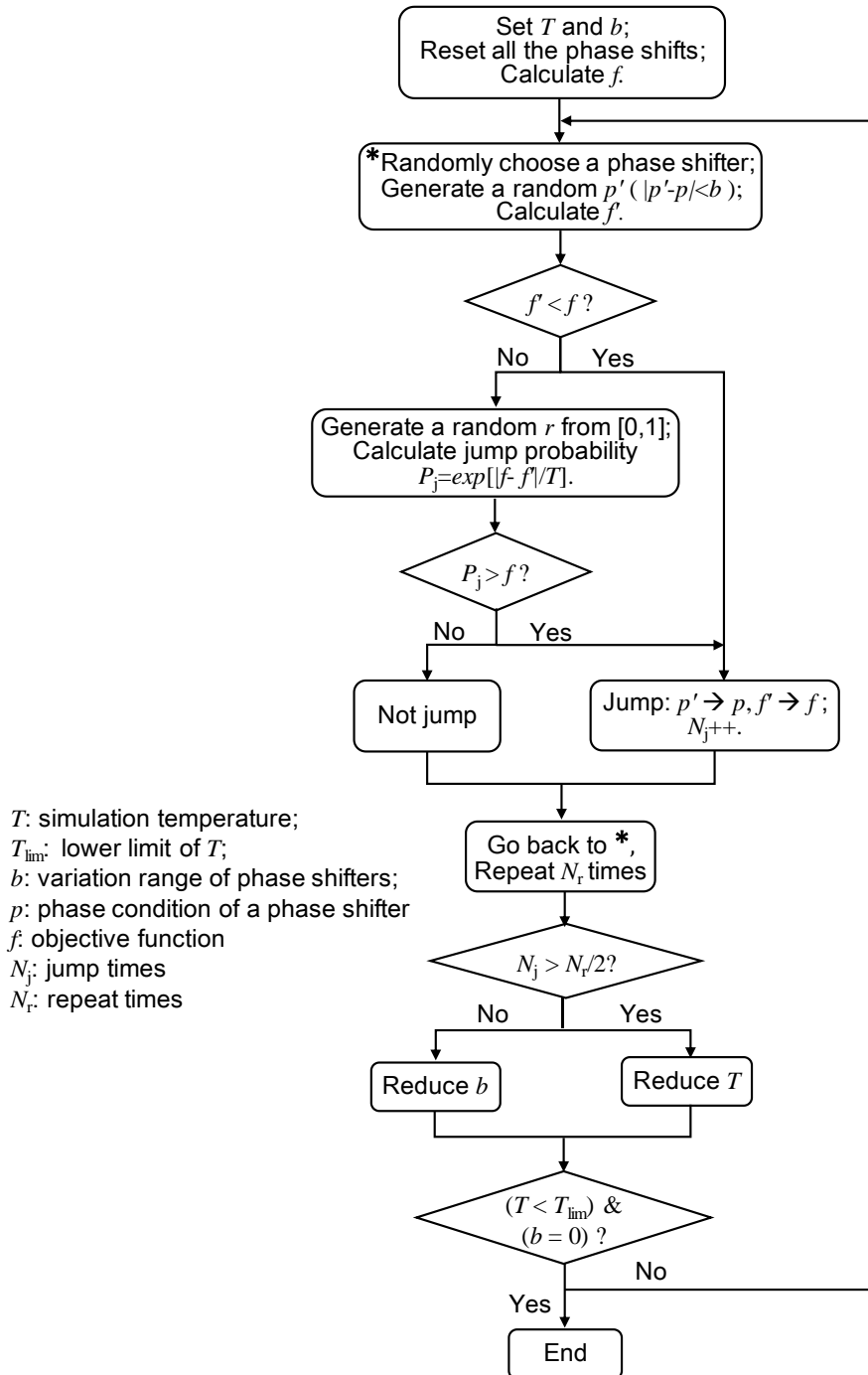


Fig. 3.3. Flow chart of using the simulated annealing algorithm to optimize the phase shifters.

between the simulation of annealing in metallurgy and the problem of solving combinatorial optimization problems [102].

The flow chart of using the simulated annealing algorithm to optimize the phase shifters is shown in Fig. 3.3. The algorithm first sets the simulation temperature (T) and the variation range of phase shifters (b), then resets all the phase shifts and calculates the objective function or figure of merit (f). f can be the MSE or other functions,

depending on the simulation scenario. Next, a phase shifter is randomly chosen and a random condition p' is applied to that phase shifter ($|p' - p| < b$). The updated objective function f' is calculated and compared with f . If f' is better, the new phase condition p' will be adopted, and the jump time N_j increases by 1; if worse, the algorithm calculates the jump probability P_j

$$P_j = \exp\left(\frac{|f' - f|}{T}\right), \quad (3.4)$$

and compares P_j with a random generated r ($r \in [0, 1]$). If P_j is greater than r , the new phase condition p' will be adopted and the jump time N_j increases by 1, otherwise the old phase condition p will be kept. The use of jump probability gives the algorithm the ability to jump out of local optimums. The above procedure is repeated for N_r times. If N_j is greater than half of N_r , then reduces T ; otherwise reduces b . The above procedure is again repeated, until T is less than the lower limit T_{lim} and b reaches 0.

3.2.2 Mean squared error

For each N ($N = 4, 8, 16$), 100 $N \times N$ unitary matrices are randomly generated [103] and used as the desired matrix T , respectively. For each T , the algorithm uses the MSE as f to optimize all the phase shifters. One python code example is given in Appendix I. Figure 3.4 shows the averaged results of MSEs after optimization, under various conditions. M is the stage number of phase shifter arrays. Different colors represent different accuracies of phase control (0.1 rad, 0.01 rad, 0.001 rad).

Overall, we can see that the MSEs gradually decreases with increasing M , which indicates that increasing the degrees of freedom can improve the transformation fidelity and is consistent with the principle of MPLC. In real applications, using more stages also increases the insertion loss. Therefore, there is a trade-off between the insertion loss and the transformation fidelity. For the same N , better phase accuracies result in lower MSEs and the curve converges slower than those with worse accuracies. For results with the same phase accuracy but different N , we can see that $|d(\text{MSE})/dM|$ decreases with increasing N , because the increased degrees of freedom per stage is inversely proportional to N . In all cases, all the desired matrix can be correctly generated with low MSEs (< -60 dB), given an enough phase accuracy (0.001 rad). Therefore, we can conclude that this new OUC scheme is feasible.

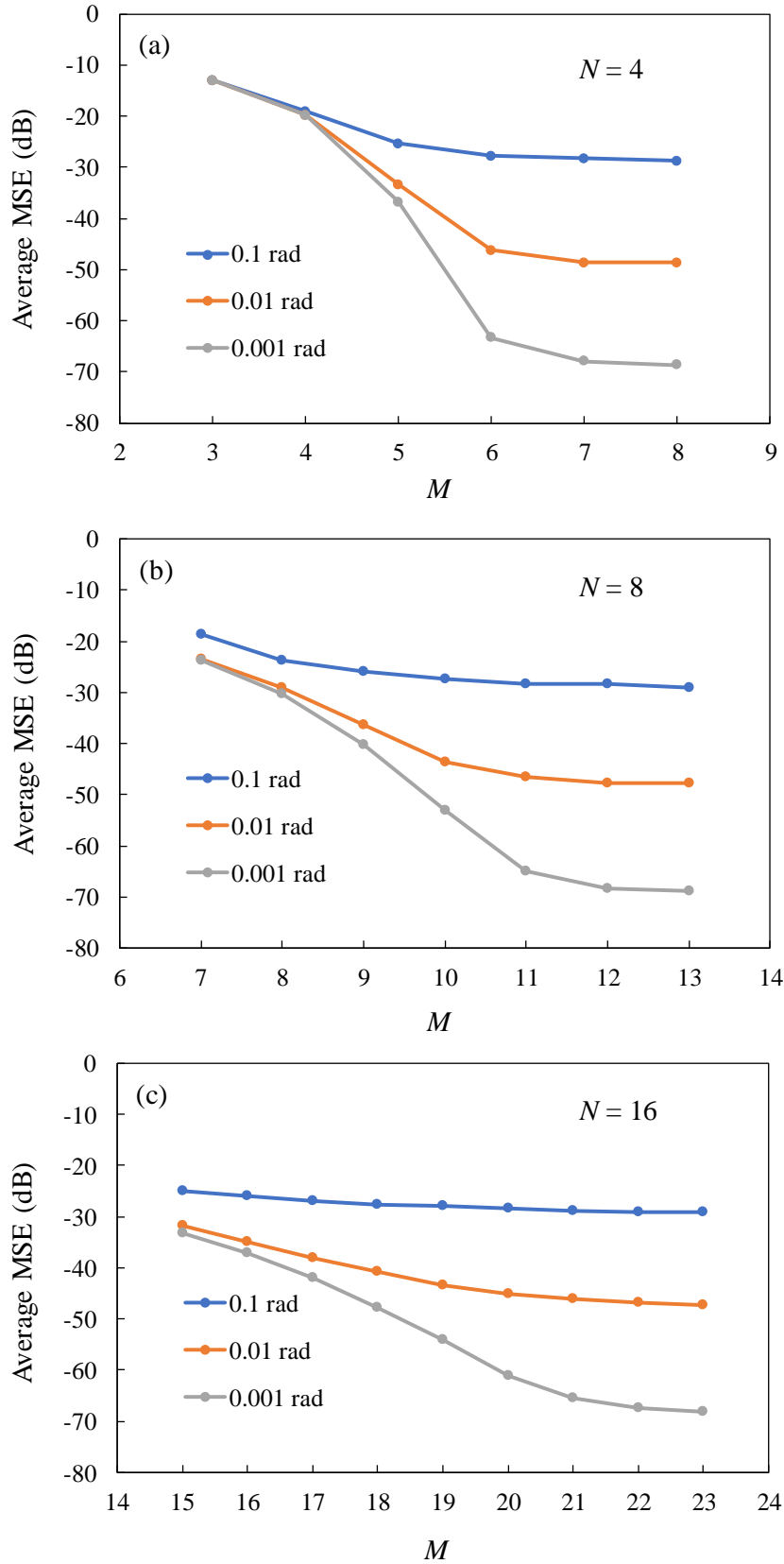


Fig. 3.4. Average MSEs as a function of M , under various conditions. (a) $N = 4$. (b) $N = 8$. (c) $N = 16$.

3.2.3 Modal crosstalk

Let us further consider the cases where OUCs are used to unscramble coupled modes. The 100 random unitary matrices in Sec. 3.2.2 are used as the mode coupling matrix \mathbf{U} , respectively. The simulated annealing algorithm again optimizes the phase shifters to unscramble the modes. Here, instead of directly using the modal crosstalk as f , we use the following function to simplify the calculations:

$$f = 1 - \frac{1}{N} \sum_{i=0}^N |C_{ii}|^2, \quad (3.5)$$

where C_{ii} is the diagonal elements of \mathbf{C} . Note that the last phase shifter array only affects the phases of the output light. Because the output phases are not important in the cases of mode unscrambling, the last phase shifter array is not activated in the calculations. Figure 3.5 shows the averaged results of modal crosstalk after optimization, under various conditions. We can observe similar results as the MSE: the modal crosstalk gradually decreases with increasing N ; for the same N , better phase accuracies result in lower crosstalks and the curve converges slower than those with worse accuracies. With a phase accuracy no worse than 0.01 rad, we can obtain less than -20 dB modal crosstalk using no less than N stages.

As an example of 16-mode unscrambling, Figure 3.6(a) and 3.6(b) plot the absolute square of all elements of \mathbf{U} and $\mathbf{T}'\mathbf{U}$, respectively, where $N, M = 16$ and the phase accuracy is 0.01 rad. We can see that the off-diagonal components are significantly suppressed in Fig. 3.6(b), which means that the modes are unscrambled effectively by the device. In addition to the simple mode unscrambling, reconfigurable mode switching can also be easily realized by implementing the matrix $\mathbf{V}\mathbf{T}'$, where \mathbf{V} is a permutation matrix representing the desired mode switching. Figure 3.6(c) plots one example of the absolute square of matrix elements after mode switching. We can see that the input modes are unscrambled and switched to different channels at the output. These results imply the applicability of the proposed device to flexible large-scale mode switchable optical networks [104].

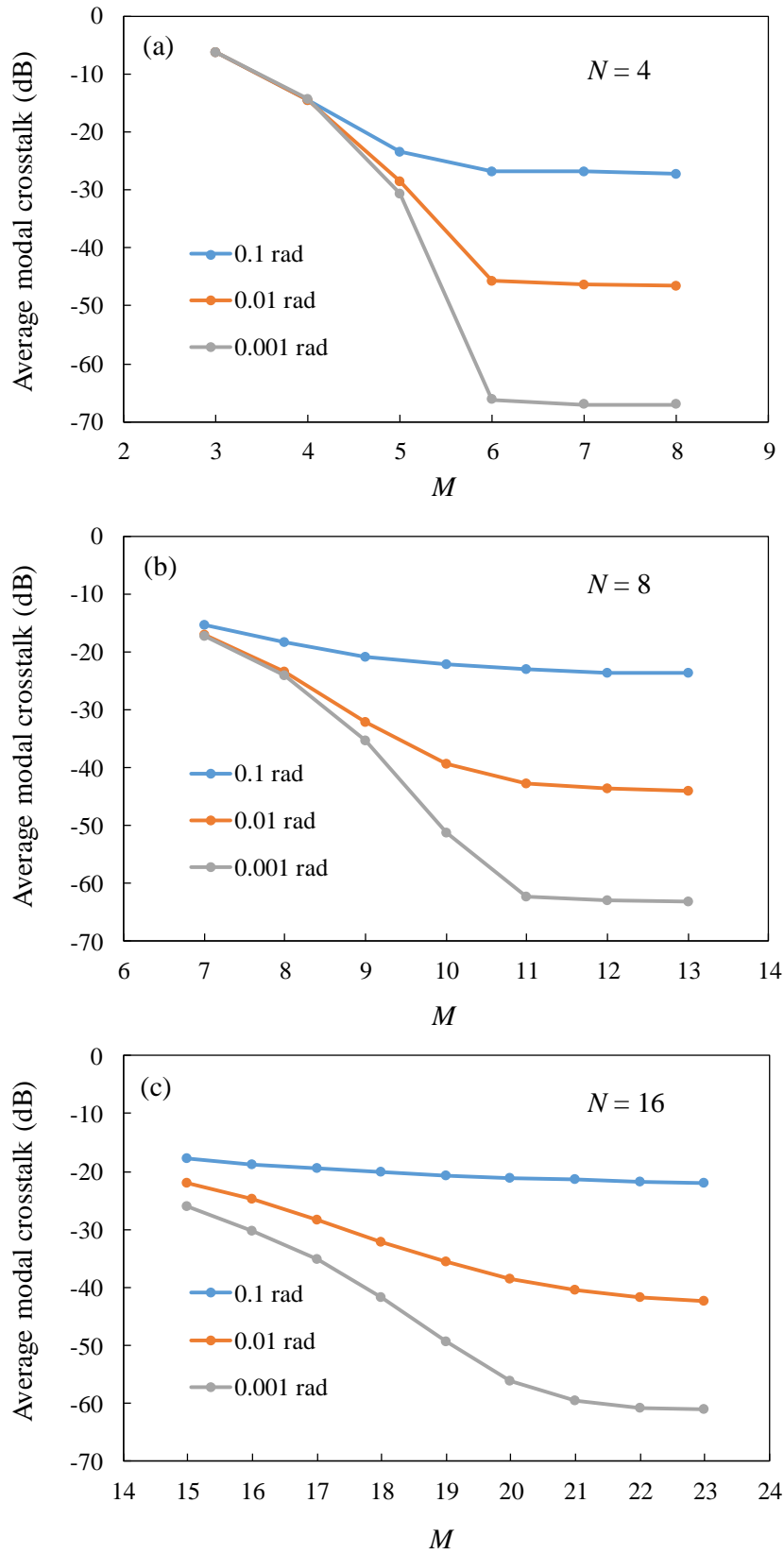


Fig. 3.5. Average modal crosstalks as a function of M , under various conditions. (a) $N = 4$. (b) $N = 8$. (c) $N = 16$.

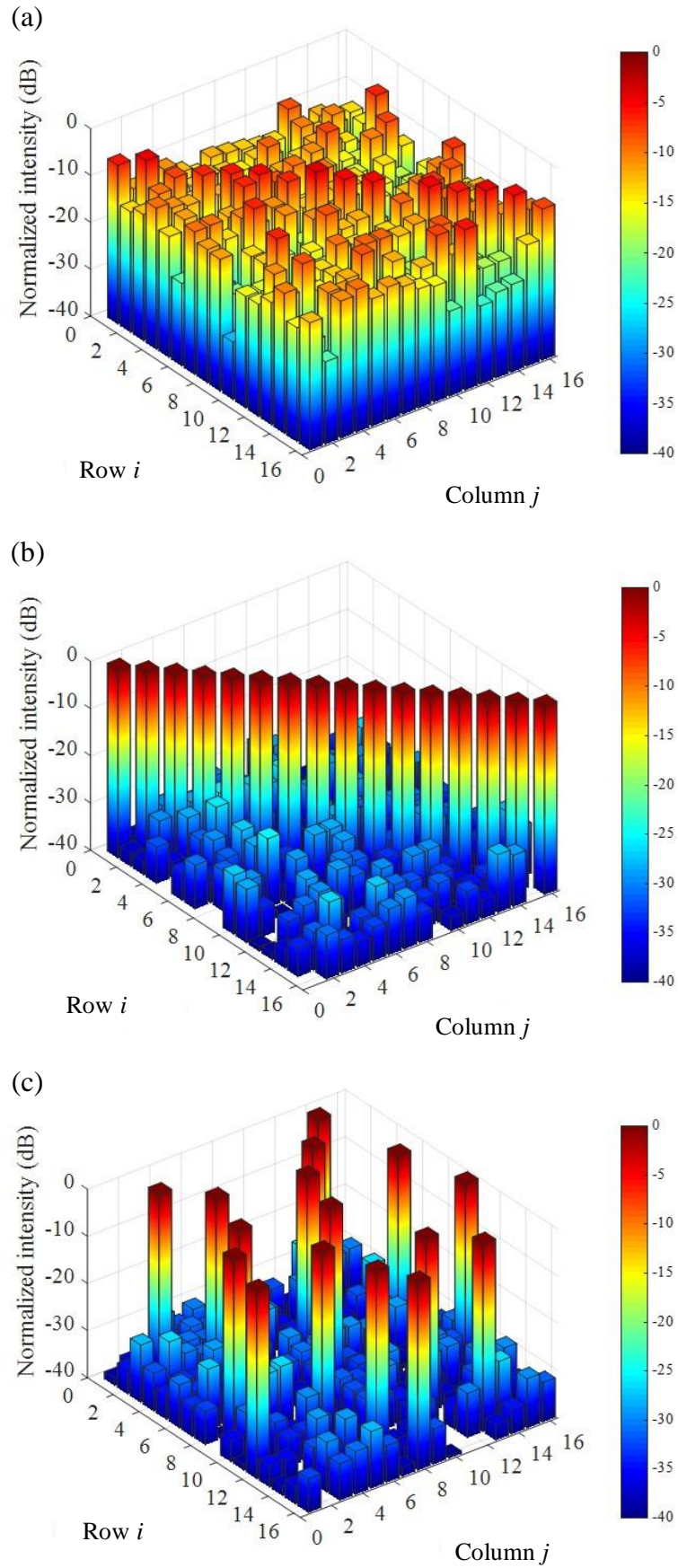


Fig. 3.6. Normalized intensity (absolute square) of matrix elements of (a) \mathbf{U} (device input), (b) $\mathbf{T}'\mathbf{U}$ (device input), (c) $N=16$.

3.3 Device design

In this section, we design a 3×3 OUC on the SOI platform for the proof-of-concept demonstration.

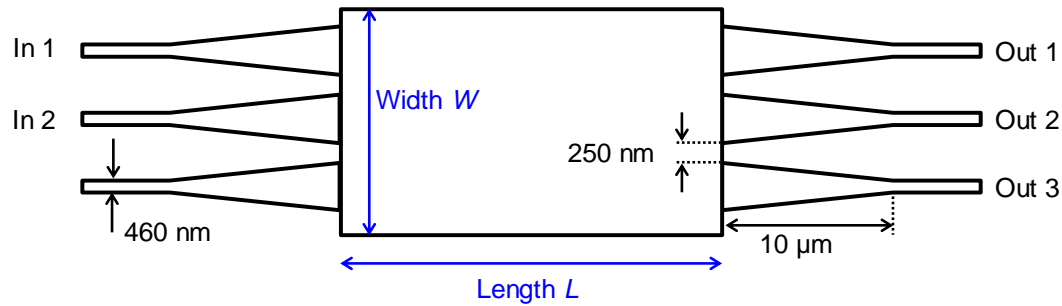


Fig. 3.7. Simulation model of the 3×3 MMI coupler.

3.3.1 3×3 MMI coupler

One of the most important passive components is the 3×3 MMI coupler. I use the Lumerical Mode Solutions to simulate the MMI coupler shown in Fig. 3.7. 10-μm-long tapers are used to connect the single-mode waveguides with the multimode waveguide.

Table 3.1 Simulation parameters of the 3×3 MMI coupler

Parameter	Value
Wavelength	1550 nm
Temperature	300 K
Refractive index (Si)	3.477
Refractive index (SiO ₂ , bottom cladding)	1.444
Refractive index (SiO ₂ , top cladding)	1.434
Mesh size (y-axis, non-taper region)	40 nm
Mesh size (y-axis, taper region)	20 nm
Mesh size (z-axis)	20 nm
Mode number (Input/output ports region)	6
Mode number (Input/output taper region)	22
Mode number (multimode waveguide region)	45
Subcell method	CVCS
EME convergence tolerance	10 ⁻¹²

The width of single-mode waveguides is 460 nm and the minimum spacing between adjacent tapers is 250 nm. EME simulations are carried out to optimize the width W and the length L of the multimode waveguide section. The input and output taper section are divided into 20 subcells, respectively. In each subcell, the mode profiles are calculated separately based on a continuously varying cross-sectional subcell (CVCS) method, which can avoid the staircasing approximation effect at the subcell interfaces

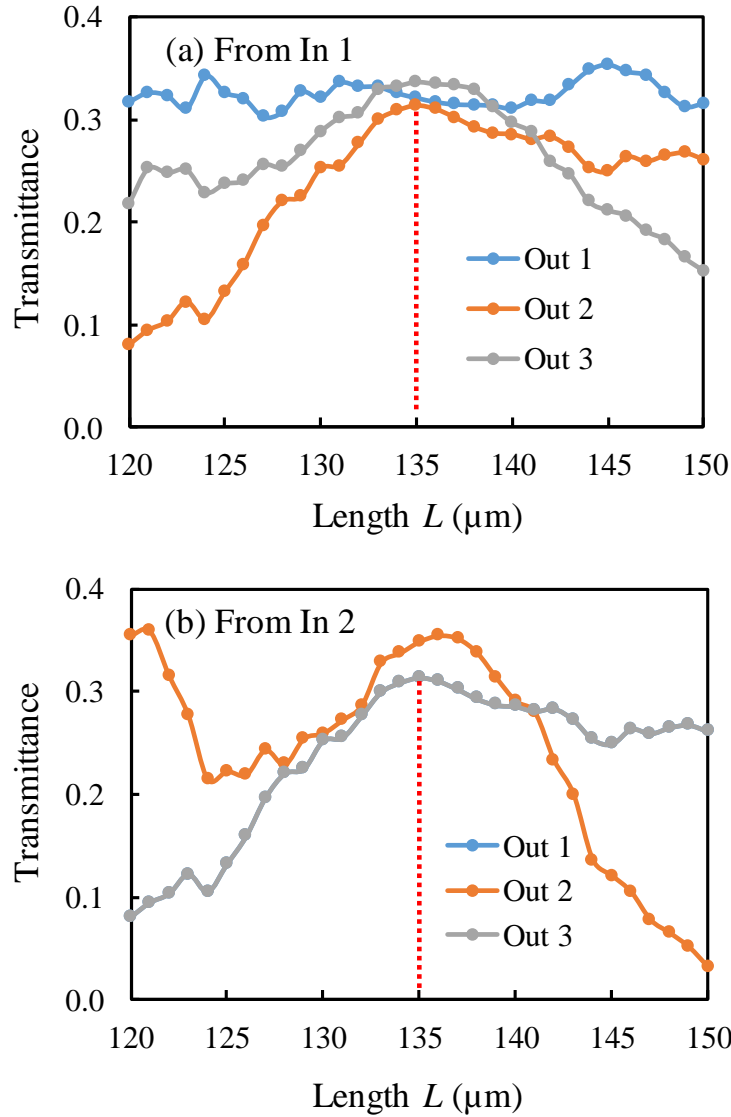


Fig. 3.8. Simulated transmittances from (a) In 1 and (b) In 2 to each output port .

[105]. The simulation parameters are listed in Table 3.1.

Figure 3.8 shows the simulated power transmittances from the top and middle input port to each output port, as a function of L when $W = 7.5 \mu\text{m}$. We can see that the total transmittance reaches the maximum at $L = 135 \mu\text{m}$. Let the insertion loss be defined as

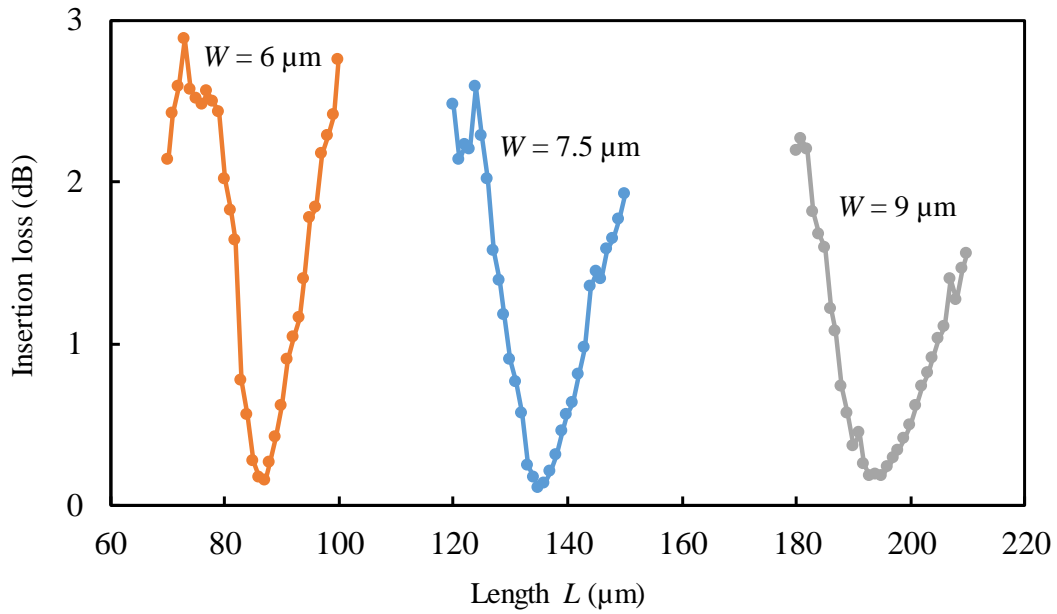


Fig. 3.9. Simulated insertion losses as a function of L .

the averaged optical power loss at the output ports when light is injected into In 1 and In 2, respectively. The insertion loss is 0.11 dB when $W = 7.5 \mu\text{m}$ and $L = 135 \mu\text{m}$. Following the same procedure, W is varied and the optimal lengths are found, as shown in Fig. 3.9. The optimal lengths are $87 \mu\text{m}$, $135 \mu\text{m}$ and $195 \mu\text{m}$ for $W = 6 \mu\text{m}$, $7.5 \mu\text{m}$ and $9 \mu\text{m}$, respectively. In addition to insertion loss, the power imbalance between the three output ports is also important, which is defined as

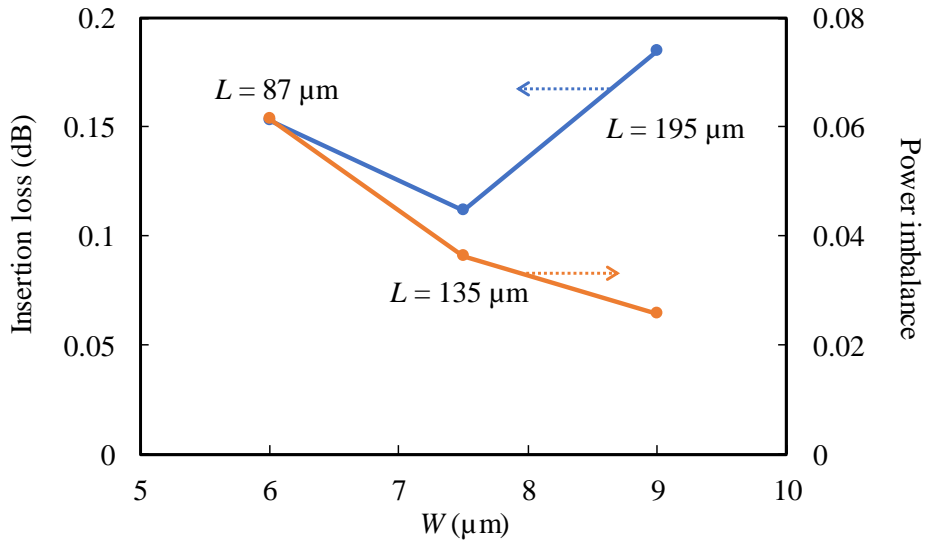


Fig. 3.10. Simulated insertion losses and power imbalances at three optimal points.

$$\frac{1}{2} \left(\sum_{i=1}^3 |t_{i1} - \bar{t}_1| + \sum_{i=1}^3 |t_{i2} - \bar{t}_2| \right), \quad (3.6)$$

where t_{i1} and t_{i2} are the power transmittance from input port 1 and 2 to output port i , respectively, \bar{t}_1 and \bar{t}_2 are given by

$$\bar{t}_m = \frac{1}{3} (t_{1m} + t_{2m} + t_{3m}) \quad (m = 1, 2). \quad (3.7)$$

Figure 3.10 shows the insertion loss and power imbalance at the three optimal points. While the power imbalance is better with a larger W , $W = 7.5 \mu\text{m}$ is chosen in order to achieve a lower insertion loss and a relatively compact size. Figure 3.11 plots the light propagation inside the 3×3 MMI coupler when $W = 7.5 \mu\text{m}$ and $L = 135 \mu\text{m}$. We can see that the light is almost equally split at the three output ports.

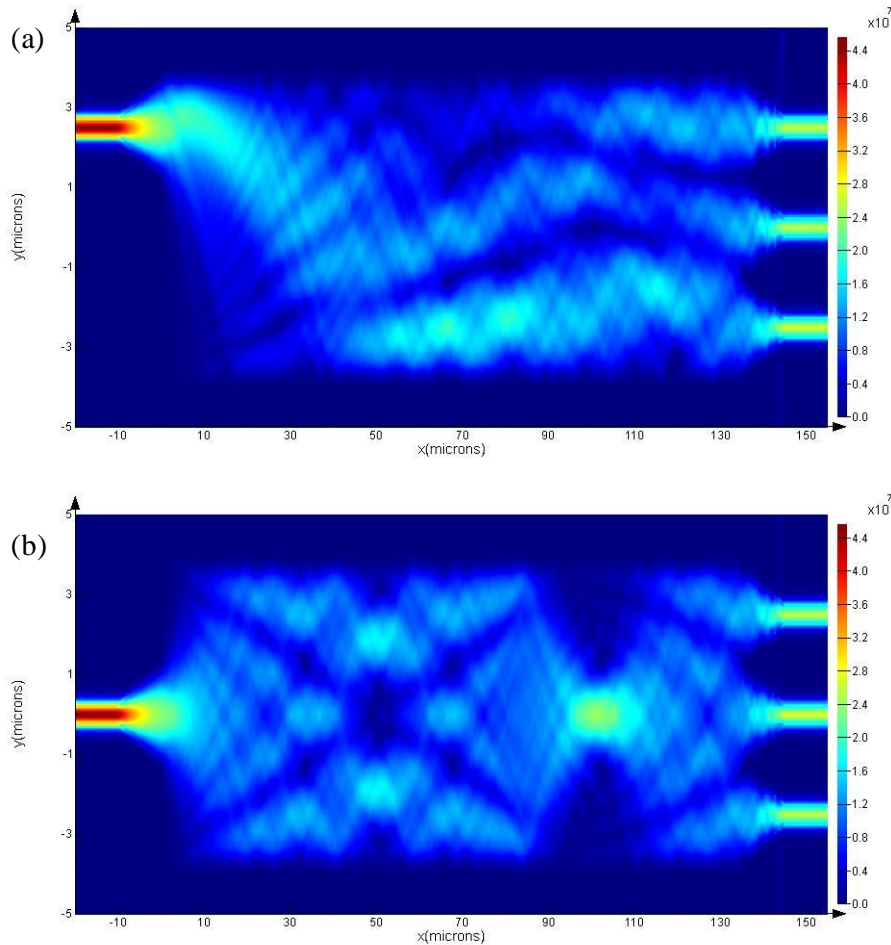


Fig. 3.11. Simulated light propagation inside the 3×3 MMI coupler when $W = 7.5 \mu\text{m}$ and $L = 135 \mu\text{m}$. (a) Light is injected into In 1. (b) Light is injected into In 2.

3.3.2 3×3 OUC

Using the 3×3 MMI coupler, we design a 3×3 OUC and a mode mixer on a SOI chip, as shown in Fig. 3.12(a). The 3×3 OUC consists of 4 stages of MMI couplers and 5 stages of phase shifter arrays. The mode mixer is used to mimic the mode coupling effect in the multimode fiber and is made of two 3×3 MMI couplers. The mode mixer scrambles the input light and the OUC will be optimized to unscramble the modes. Figure 3.12(b) and 3.12(c) show one MMI coupler and one phase shifter, respectively. The design of the phase shifter is provided by my collaborators at National Institute of Advanced Industrial Science and Technology (AIST). The three paths are length-matched by inserting an additional delay line in the middle path, as shown in Fig. 3.12(d). The length-matched paths can maximize the operation bandwidth of this device. The minimum bending radius in this design is 20 μm , so the associated bending loss is negligible. The pitch of the input and output edge coupler array is 127 μm . Each edge coupler consists of a taper region that the width of which decreases gradually from 460 nm to 180 nm. The two outer edge couplers are used to facilitate the coupling with fiber arrays. Because the absolute optical phases are not important in this case, there are only two phase shifters in each phase shifter array. The two phase shifters share the same ground pad on the chip.

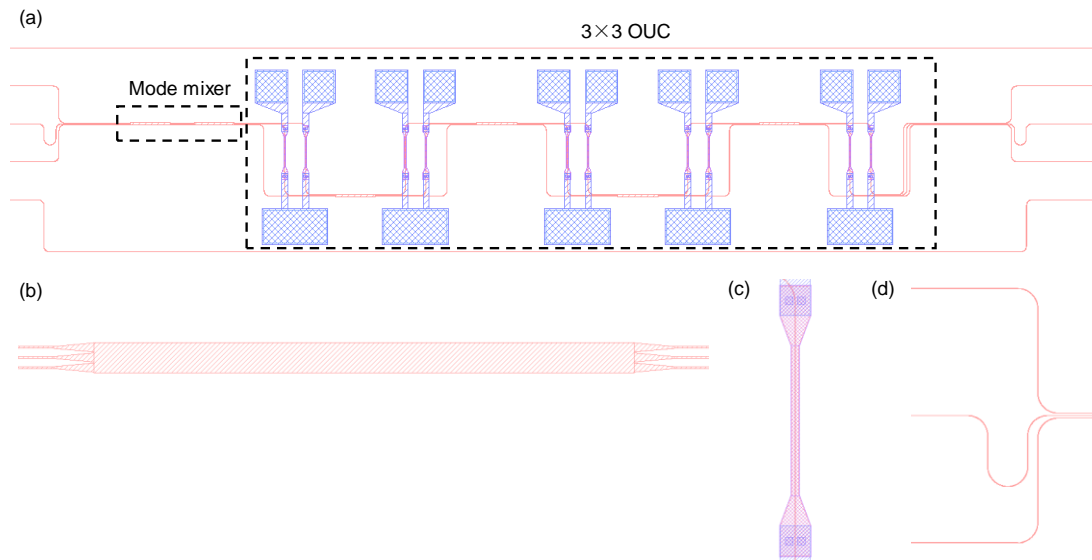


Fig. 3.12. (a) A 3×3 OUC and a mode mixer designed on the SOI platform. (b) Single 3×3 MMI coupler. (c) Single thermo-optic phase shifter. (d) A delay line is inserted to the middle path to equalize the lengths of the three paths.

3.4 Fabricated device

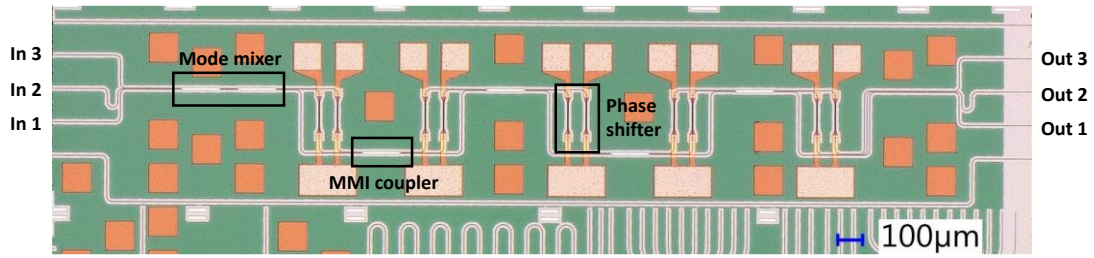


Fig. 3.13. A microscope image of the fabricated chip.

The designed device is fabricated by my collaborators at AIST. Figure 3.13 shows the microscope image of the fabricated device. The core size of the silicon waveguide is $460 \times 220 \text{ nm}^2$. The thermo-optic phase shifters are made of thin TiN films. The device size is $3.8 \times 1.2 \text{ mm}^2$. Originally, there are other devices on the same chip, such as MZIs. The device in Fig. 3.13 is therefore cut from the chip by a dicing machine. However, the input facet is not flat enough after the dicing, which results in a large coupling loss with the fiber array.

3.5 Device characterization

3.5.1 Propagation loss

The propagation loss of light in the single-mode waveguide is firstly characterized. There are three single-mode waveguides with different lengths on the same chip, as illustrated in Fig. 3.14. we inject light into the three waveguides using a lensed fiber and measure the power at the output, respectively. However, one facet of one

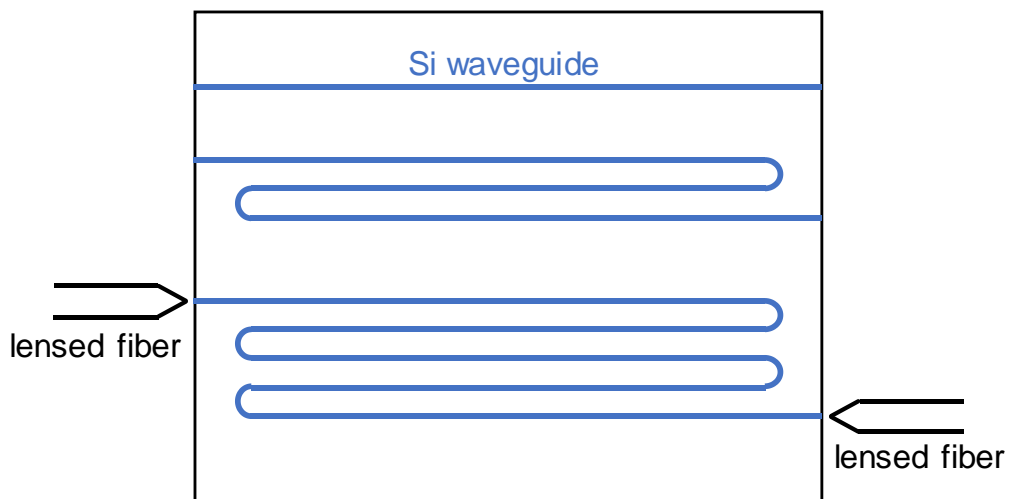


Fig. 3.14. Measuring the propagation loss of light.

Table 3.2 Measured transmittances of two silicon waveguides

Length (cm)	Transmittance, TE (dB)	Transmittance, TM (dB)
0.651	-8.11	-6.41
3.1761	-13.31	-10.91

waveguide is damaged during the dicing process, so only the measured data of the other two waveguides are used. The measured power transmittances are given in Table 3.2. Applying a linear fitting to the results, the propagation losses of TE and TM light are 2.06 dB/cm and 1.78 dB/cm, respectively.

3.5.2 Phase shifter

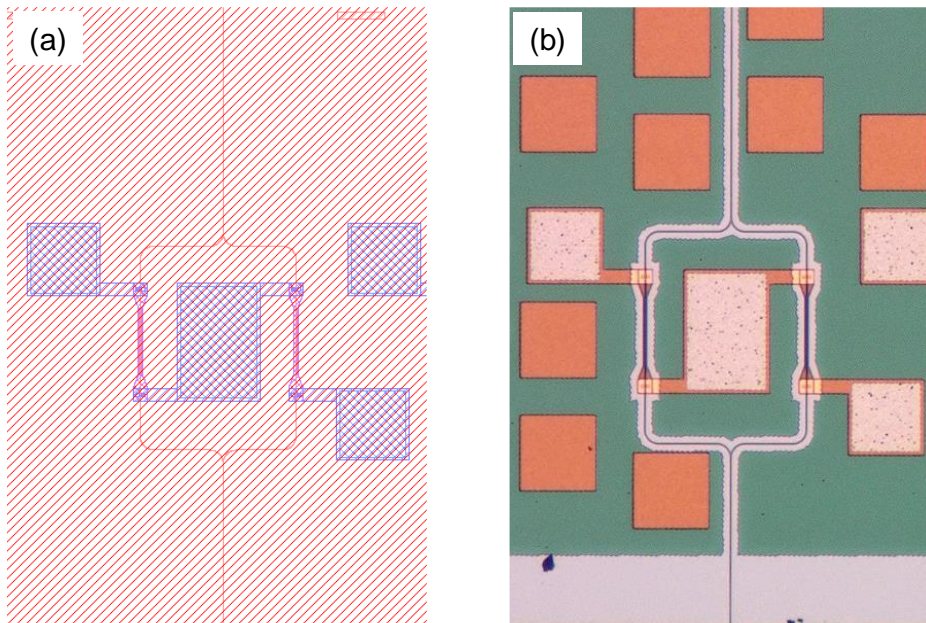


Fig. 3.15. (a) Designed MZI. (b) Microscope image of the MZI.

The phase shifter is characterized using an asymmetric MZI on the same chip, as shown in Fig. 3.15. The path length difference of the two arms is $30\ \mu\text{m}$, which corresponds to an FSR of $\sim 19\ \text{nm}$. The bonding pads of one arm are wire-bonded and connected with an external voltage source. The I-V characteristics of the phase shifter is characterized and the result is shown in Fig. 3.16. The measured resistance is $\sim 280\ \Omega$.

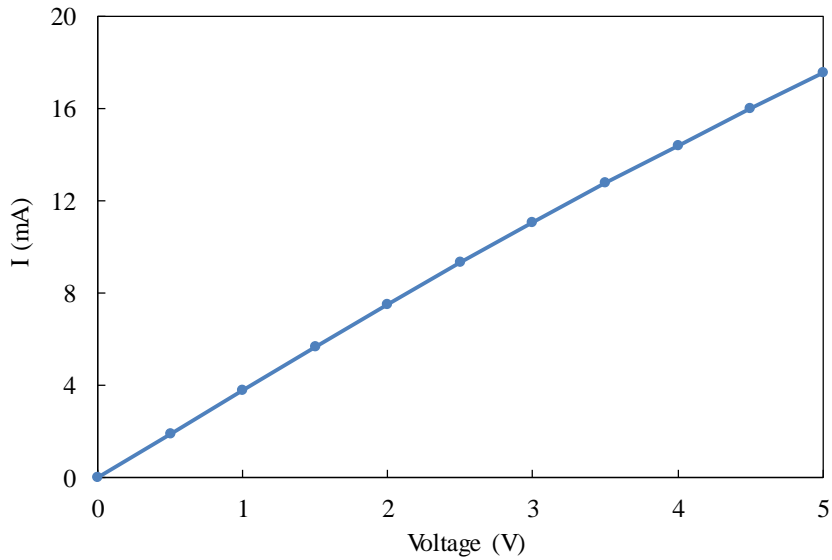


Fig. 3.16. Measured I-V characteristics of the phase shifter.

Next, the voltage applied to the phase shifter is changed and the transmission spectra of the MZI are measured using a tunable laser. Figure 3.17 shows the measured transmission spectra under various voltages. When increasing the applied voltage, the transmission shifts toward the long-wavelength side. We can see that under a voltage between 3 V and 3.5 V, the spectrum shifts back to the same position where no voltage is applied. Therefore, the 2π -phase-shift voltage is between 3 V and 3.5 V.

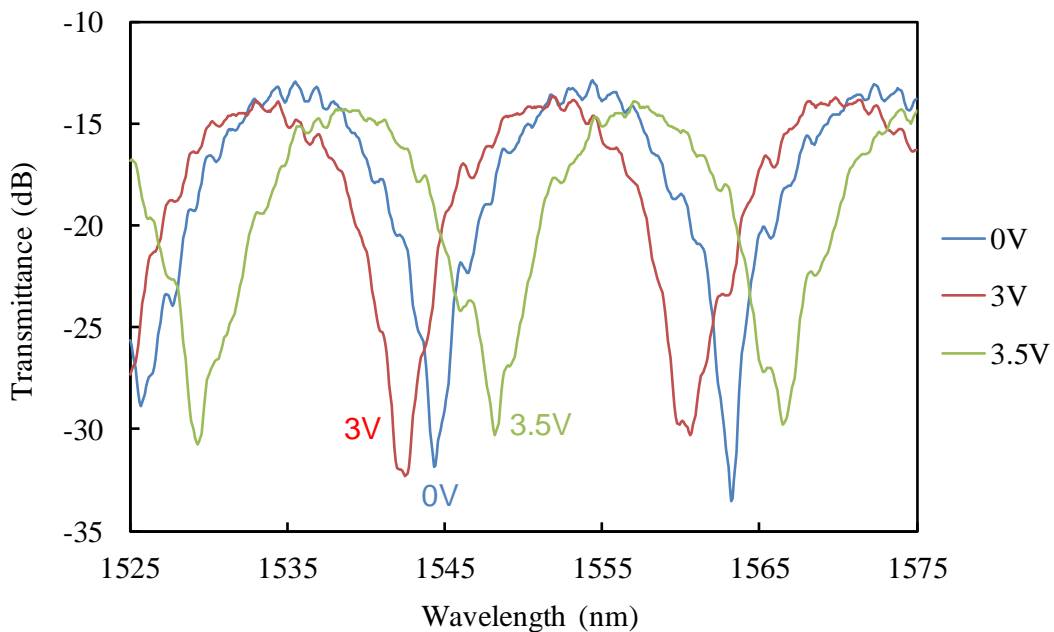


Fig. 3.17. Measured transmission spectra of the asymmetric MZI.

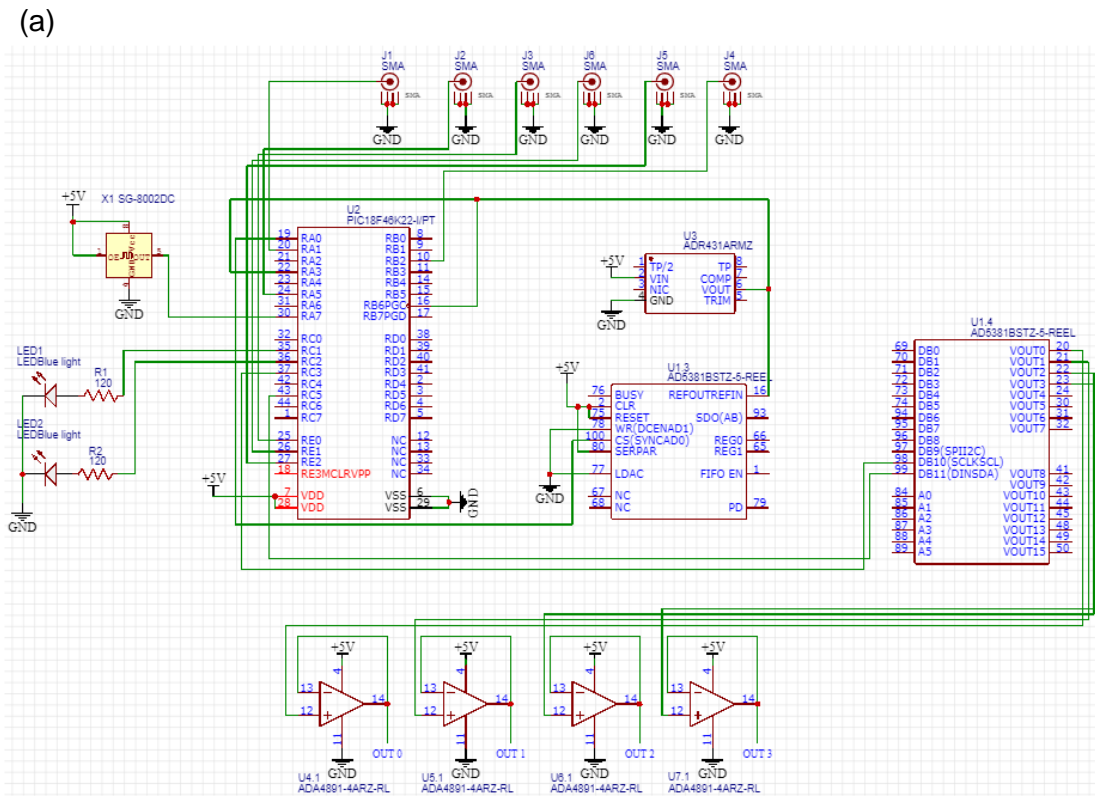
3.5.3 Custom-designed electronic circuit

Table 3.3 Main electronic components used in the custom-designed electronic circuit

Component	Manufacturer	Model number
Microcontroller	Microchip	PIC18F46K22
Crystal oscillator	Epson	SG-8002DC
DAC	Analog Devices	AD5381
Voltage reference	Analog Devices	ADR431A
Operational amplifier	Analog devices	ADA4891-4
FFC connector	Molex	5025983993

In order to optimize the phase shifters in the real device, we need a real-time electronic circuit to experimentally implement the simulated annealing algorithm. More specifically, the circuit needs to detect the output optical power at the three output ports, process the data based on the algorithm and controls the voltages applied to all the phase shifters accordingly. However, there are no available commercial products that can provide these functions. An alternative way is to build the voltage-output module and the optical power detection module separately and use a computer to process the data and control the modules. However, this scheme will increase the optimization time due to the relatively-long time delay during the communication between the computer and the modules. We therefore develop a custom-designed electronic circuit that integrates all the modules on a single board.

The main electronic components used in the circuit are listed in Table 3.3. The microcontroller is the key component in the circuit, which executes the algorithm and controls all the peripheral devices. In this work, we use the PIC18F46K22 from Microchip, which supports up to 16 million instructions per second (MIPS) operation. Programs are written into the microcontroller through an external debugger (PICkit 3). The crystal oscillator (Epson, SG-8002DC) provides a 20-MHz clock signal to the microcontroller. 6 built-in analog-to-digital converter (ADC) channels of the microcontroller are used, each channel samples the input voltage at a 10-bit resolution.



(b)

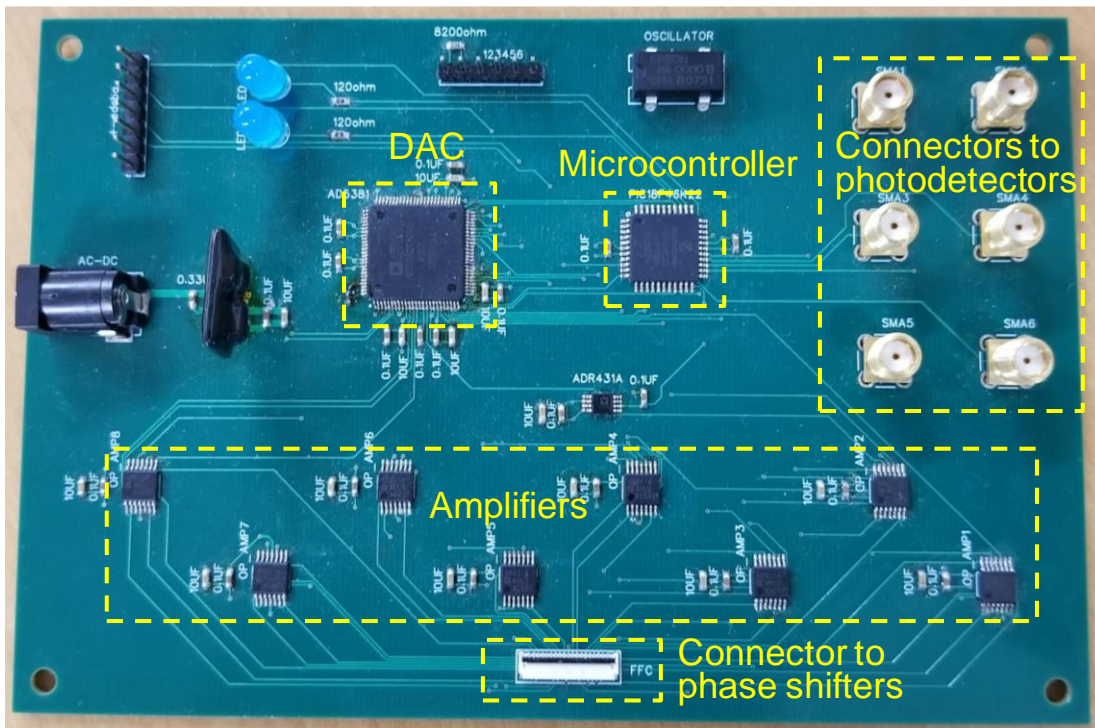


Fig. 3.18. (a) Schematic of the electronic circuit. Not all of the components are shown. (b) Image of the PCB. The FFC connector is soldered by a reflow soldering process, the other components are soldered by hand.

The microcontroller controls an external digital-to-analog converter (DAC) through the serial peripheral interface (SPI) communication protocol. The DAC (Analog Devices,

AD5381) has 40 output channels, each channel provides a 12-bit output voltage between 0 V to 5 V. This voltage range is enough for the operation of thermo-optic phase shifters. The voltage reference (Analog Devices, ADR431A) provides a standard 2.5 V reference for the DAC. The first 32 DAC output channels are amplified by the operational amplifiers (Analog Devices, ADA4891-4) because the load current of the DAC is only 1 mA, which is not enough for the phase shifter. The operational amplifiers are configured to function as voltage followers and can provide up to 125-mA current. The amplified DAC outputs then go through an FFC connector (Molex, 5025983993) and an FFC cable to another bridge PCB, which connects with a custom-designed chip carrier through wire bonding.

The schematic of the electronic circuit and the printed circuit board (PCB) are shown in Fig. 3.18. Not all of the components are shown in the schematic. The PCB has 4 layers, the two inner layers are the voltage-plane and ground-plane layer, respectively, the top and bottom layers are signal layers. All the components are soldered by hand on the top layer, except for the FFC connector, which is soldered by a reflow soldering process. There are two LEDs on the board, which are used to indicate the status of the ongoing optimization algorithm. Several capacitors are used to filter out noises in the power supply.

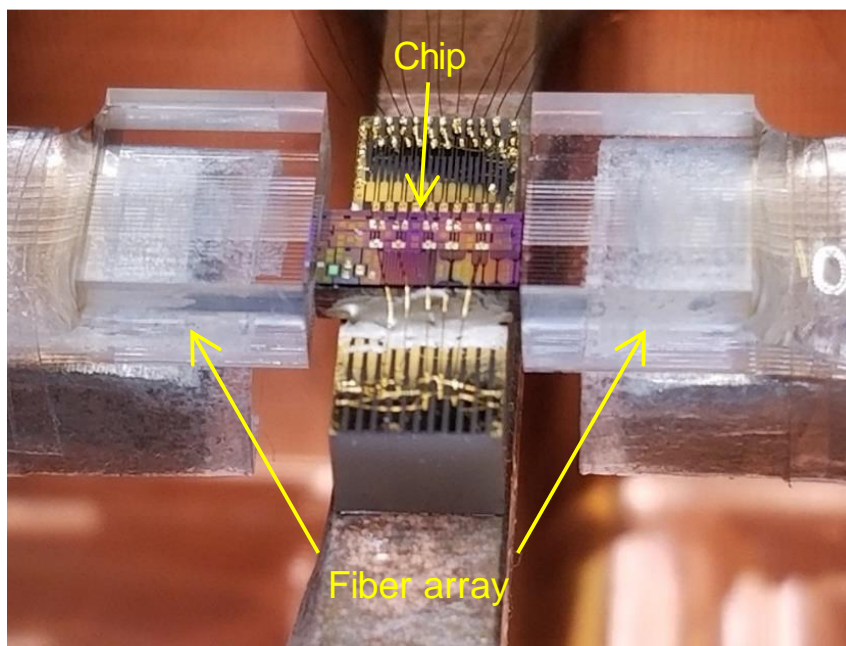


Fig. 3.19. Image of coupling light into and out from the chip through two fiber arrays. The chip is wire-bonded with a chip carrier.

3.5.4 Mode unscrambling experiments

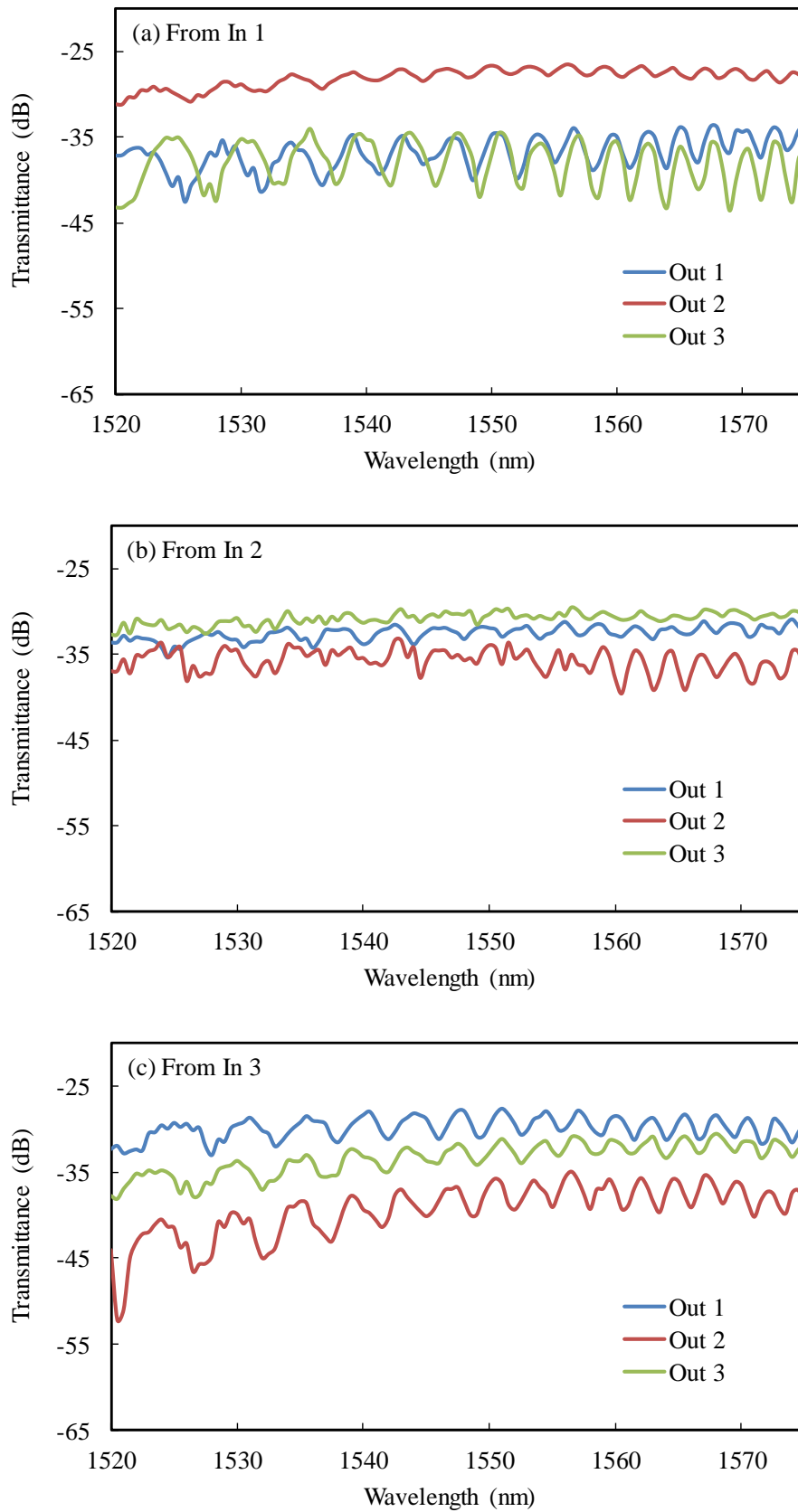


Fig. 3.20. Measured transmission spectra before optimizing the phase shifters when the light is input into (a) In 1, (b) In 2 and (c) In 3, respectively.

We first measured the transmission spectra of the device before optimizing the phase shifters. The light is coupled into and out from the chip through two fiber arrays, as shown in Fig. 3.19. Each fiber array has 12 high-index-difference optical fibers. The chip is wire-bonded with a chip carrier, which is further wire-bonded with the bridge PCB mentioned in Sec. 3.5.3. Before the optimization, the input light is adjusted to the TE polarization and injected into each input port, then the transmission spectra at the three output ports are measured. The results are shown in Fig. 3.20. We can see that the modes are severely mixed at the outputs, especially in Fig. 3.20(b). If we modulate the input light directly, no signals can be retrieved due to the strong modal crosstalk. From a separate measurement, the coupling between the fiber array and the chip is measured to be around 12~14 dB/facet, which can be significantly reduced by improving the design of the edge couplers. The on-chip loss is estimated to be 1~2 dB at the 1550-nm wavelength.

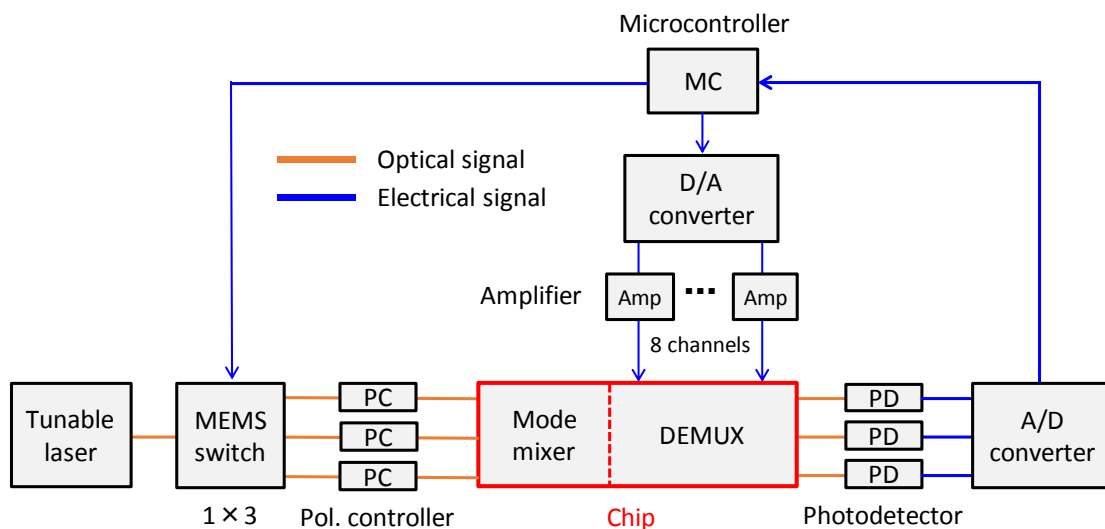


Fig. 3.21. Experimental setup for optimizing the phase shifters.

We then use the PCB to implement the simulated annealing algorithm, in order to unscramble the mixed modes. The experimental setup is shown in Fig. 3.21. The micro-electromechanical system (MEMS) switch is built using multiple 1×2 MEMS switches (Thorlabs, OSW12-1310-SM). The microcontroller sequentially selects one input optical port (In 1, 2, or 3) by controlling the MEMS switch (switching time: ~ 1 ms) and collects the output signals from the three photodetector (PD) modules. Each PD module (New Focus, 1811) has a built-in transimpedance amplifier (TIA), and the relation

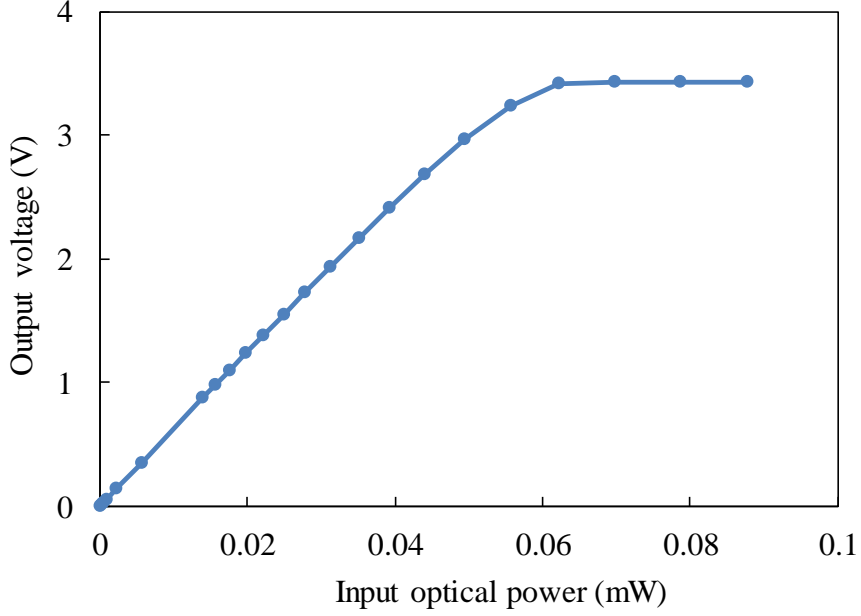


Fig. 3.22. Output voltage versus input optical power characteristics of the PD module. The output voltage saturates from ~ 0.07 -mW (-11.6 -dBm) input optical power.

between the output voltage and input optical power is characterized in Fig. 3.22. We can see that the output voltage saturates from ~ 0.07 -mW (-11.6 -dBm) input optical power. During the optimization, the output power of the tunable laser (Santec, TSL-510) is adjusted so that the maximum output power from the chip output is lower than -11 dBm. The objective function f depends on the desired unscrambling pattern. For example, if we want to direct the light from In 1 to Out 1, In 2 to Out 2 and In 3 to Out 3, respectively, f can be

$$f = a_1 t_{11} + a_2 t_{22} + a_3 t_{33}, \quad (3.8)$$

where t_{ii} is the power transmittance from input port i to output port i , a_i is a coefficient used to compensate for the port-dependent insertion loss. The optimization algorithm is written in C and one example of the source code is shown in Appendix II. Each iteration in the experiment takes about 5 ms, which is limited by the switching time of the MEMS switch (~ 3 ms for testing three ports). The entire optimization converges typically after about 30 s (~ 6000 iterations). For large-scale chips with more input and output ports, instead of using an optical switch to test all the channels one by one, we can add a small amplitude modulation to each channel with a different pilot tone [16, 106], so that light from each input port can be distinguished at the output ports simultaneously. After the algorithm has converged, all the phase shifters are set to the optimized condition. Since the simulated annealing algorithm is a probabilistic

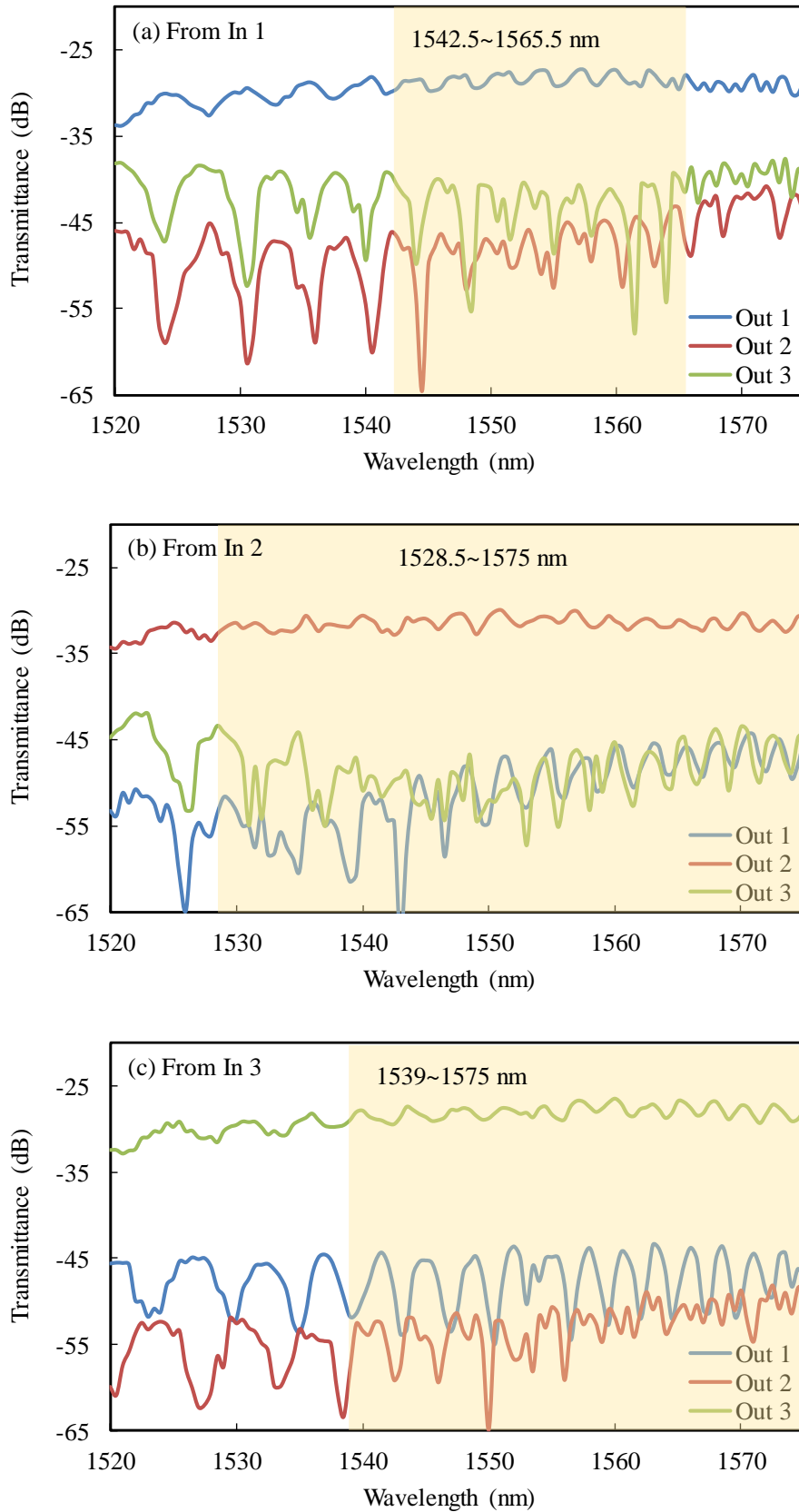


Fig. 3.23. Measured transmission spectra when the phase shifters are optimized so that the light from (a) In 1, (b) In 2 and (c) In 3 are demultiplexed to Out 1, Out 2 and Out 3, respectively. The shadowed regions represent the regimes with less than 3 dB wavelength-dependent loss and less than -10 dB modal crosstalk.

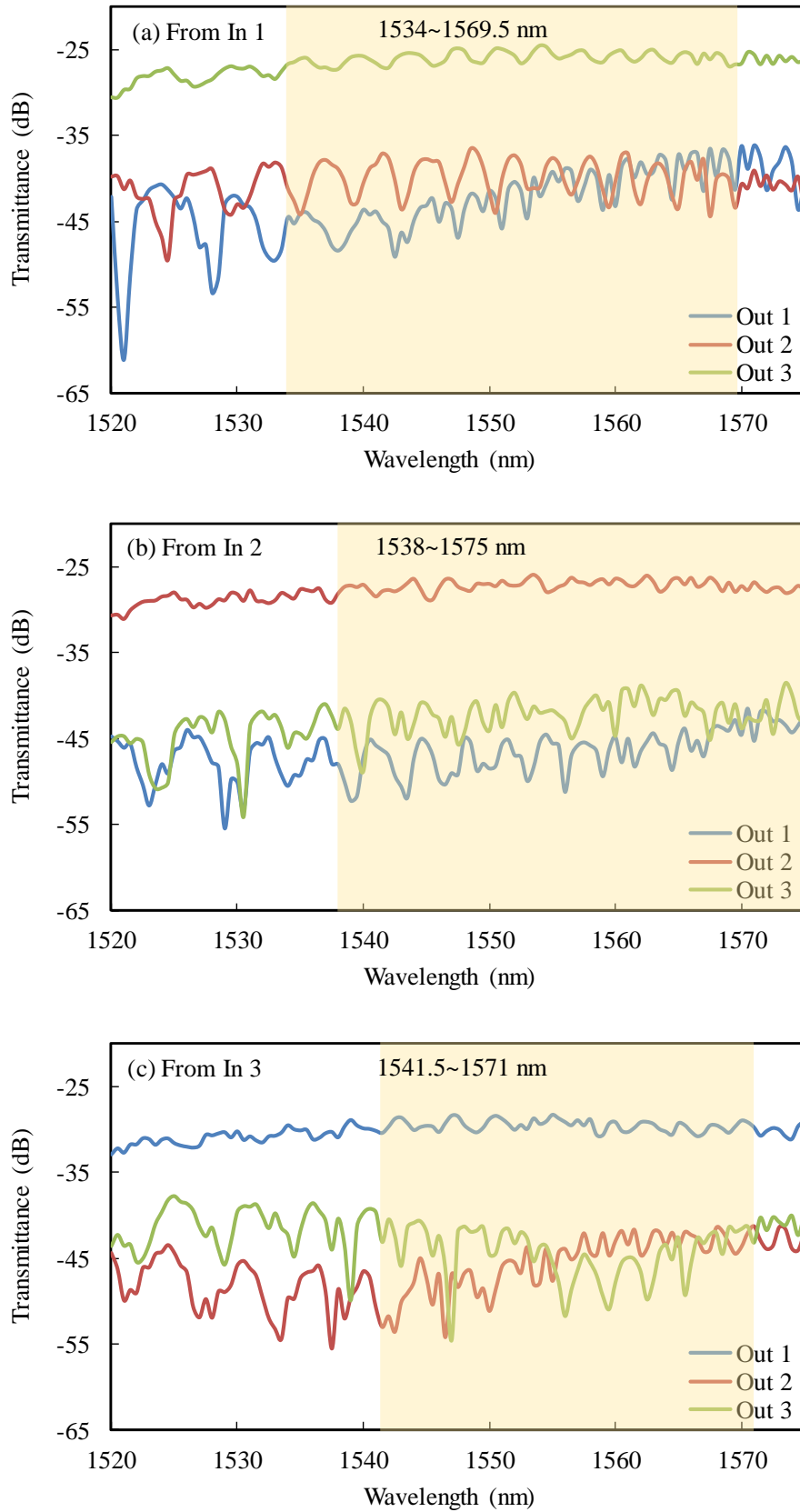


Fig. 3.24. Measured transmission spectra when the phase shifters are optimized so that the light from (a) In 1, (b) In 2 and (c) In 3 are demultiplexed to Out 3, Out 2 and Out 1, respectively.

algorithm, the derived phase conditions generally differ after each execution. However, We have observed that the modal crosstalks at the output ports converge to similar values after the optimization. One advantage of using the simulated annealing algorithm is that even when some of the phase shifters do not operate efficiently, the algorithm can still converge to a near-optimal condition. Although the overall performance will degrade gradually with reduced number of effective phase shifters, the robustness of this scheme can be attractive when the device is employed in real systems.

Figure 3.23 shows the measured transmission spectra of the device when the phase shifters are optimized so that the light from In 1, In 2 and In 3 are demultiplexed to Out 1, Out 2 and Out 3, respectively. Similarly, Figure 3.24 shows the case where the light from In 1, In 2 and In 3 are demultiplexed to Out 3, Out 2 and Out 1, respectively. In all cases, over a wide operation wavelength range of 1542.5~1565.5 nm, we obtain modal crosstalks of less than -10 dB and wavelength-dependent losses of less than 3 dB. On the other hand, residual periodic fluctuations are observed in the transmission spectra, which is the main factor that limits the operation bandwidth of this device. The fluctuation is attributed a Fabry-Perot interference inside the MMI couplers, similar to those observed in the device based on 2×2 MMI couplers [19]. By optimizing the structure of the MMI coupler, such as using wider and longer taper waveguides [107, 108], the reflection inside the MMI coupler can be suppressed. Therefore, smaller crosstalks and wider operation bandwidths can be expected.

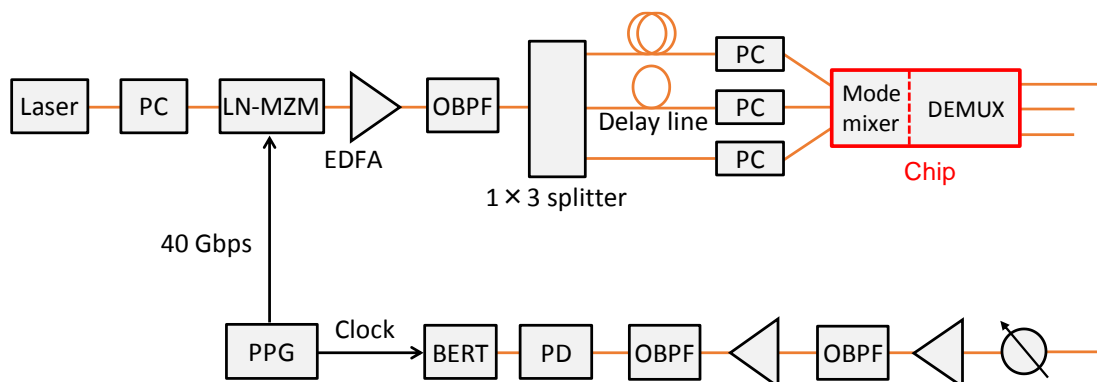


Fig. 3.25. Experimental setup used for mode demultiplexing of 40 Gbps signals (PPG: pulse pattern generator, LN-MZM: LiNbO₃ Mach-Zehnder modulator, PC: polarization controller, EDFA: erbium-doped fiber amplifier, OBPF: optical bandpass filter, VOA: variable optical attenuator).

3.5.5 40-Gbps signal demultiplexing

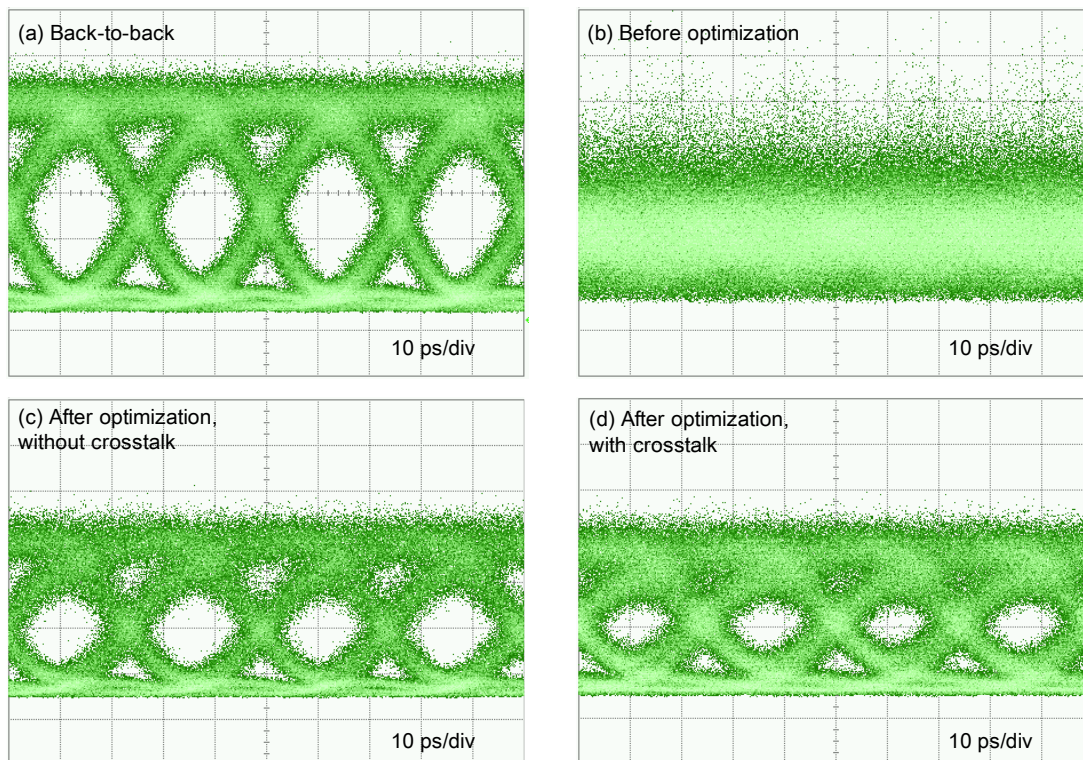


Fig. 3.26. Eye diagrams of 40 Gbps NRZ signals at 1550-nm wavelength measured (a) back-to-back, (b) at Out 1 before the optimization, (c) at Out 1 after optimizing the chip to demultiplex the light from In 1 to Out 1, the crosstalks from other input ports are switched off, (d) at Out 1 after optimizing the chip to demultiplex the light from In 1 and Out 1, the crosstalks from other input ports are switched on.

After the static mode unscrambling in Sec 3.5.4, we send 40 Gbps signals into the device and characterize the output signals. Figure 3.25 shows the experimental setup. Three 40 Gbps non-return-to-zero (NRZ) intensity-modulated signals at the 1550-nm wavelength are sent into all channels, where optical fibers of different lengths are employed to decorrelate the signals. The transmitted signals are then amplified and filtered for eye diagram and bit error rate (BER) characterization. Figure 3.26 shows the eye diagrams of signals measured under various conditions. Before optimizing the chip, we can see from Fig. 3.26(b) that the signal is severely distorted due to the crosstalks from other channels. In contrast, Figure 3.26(c) and 3.26(d) show that the signal from In 1 is successfully demultiplexed to Out 1 after the optimization. Although the eye diagram degrades in Fig. 3.26(d) due to crosstalks from other channels, we can still observe a clear eye opening.

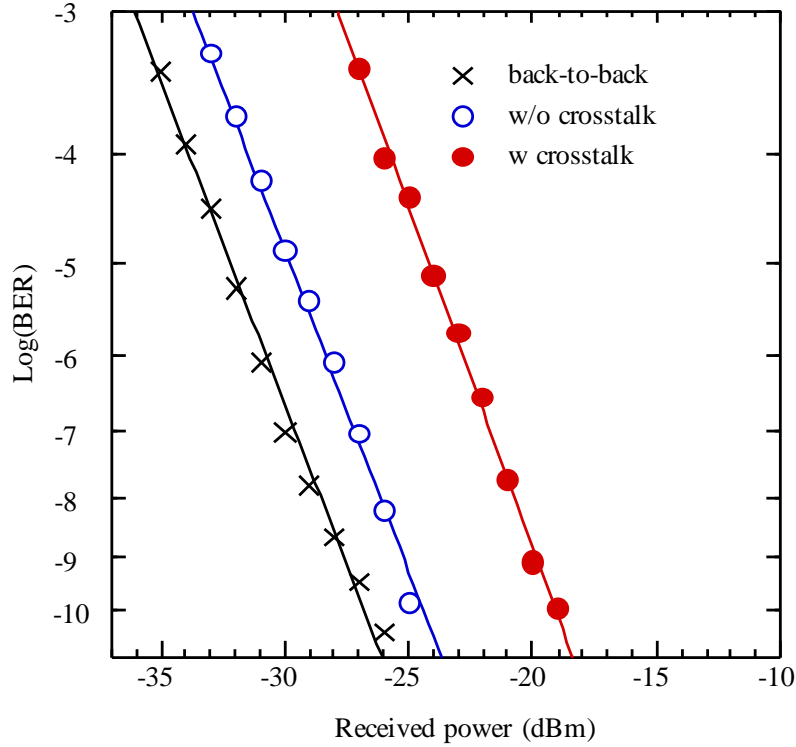


Fig. 3.27. BERs of mode-demultiplexed 40 Gbps signals measured at various conditions.

The measured BERs under various conditions are plotted in Fig. 3.27. We can see that even under the presence of crosstalks from other input channels, a BER less than 10^{-9} is achieved. The received power penalty is 8 dB, which can be reduced by further optimizing the extinction ratio and suppressing the internal reflection of MMI couplers.

3.6 Summary

In this chapter, we proposed a novel OUC using cascaded stages of MMI couplers and phase shifter arrays. From the numerical analysis, we showed that given enough stages and phase accuracy, the transfer matrix of the OUC can be configured to desired unitary matrices with high fidelities.

Next, we experimentally demonstrated a 3×3 OUC on a compact silicon chip. By optimizing the phase shifters with a custom-designed PCB, reconfigurable 3-mode demultiplexing was realized with a wavelength-dependent loss of less than 3 dB and a modal crosstalk of less than -10 dB over 23-nm wavelength range. Besides, error-free demultiplexing of 40 Gbps signals was successfully demonstrated. This is the first experimental demonstration of an integrated OUC based on MPLC.

Compared with previous results of mode unscrambling using a 4×4 OUC based on the Reck's scheme [16], the operation of our chip is less wavelength-sensitive, thanks to the symmetric structure and wideband MMI couplers. While the modal crosstalk after demultiplexing and the optimization time need be further improved, this scheme may be attractive for applications in optical communication systems because of the wide operation bandwidth and smaller path-dependent loss. On the other hand, for applications in quantum information processing and optical neural networks, a wide operation bandwidth may not be required. Other properties, such as insertion loss and fabrication tolerance, may be more important. The OUC using MMI couplers, however, is not robust enough because the operation of the MMI coupler is relatively sensitive to fabrication errors. Therefore, a different OUC structure is needed for robust operations.

Chapter 4 Robust integrated OUC using multiport direction couplers

In Chapter 3, we presented the principle, design, and characterization of the wideband integrated OUC using MMI couplers. MMI couplers bring a wide operation bandwidth but are relatively sensitive to fabrication errors. In fact, all existing OUCs suffer from a common problem: the device performance is sensitive to fabrication inaccuracies. More specifically, a perfect $N \times N$ OUC requires either perfect 50:50 splitters in MZIs, or perfect $N \times N$ MMI couplers. However, both of these are sensitive to fabrication errors. Even a slight deviation from their ideal conditions, caused by fabrication errors, accumulates in the cascaded stages, thus presenting a great challenge to realize large-scale OUCs with high performance. Inserting additional rows of MZI [109] or using near-perfect MZIs [93, 94] can substantially improve the tolerance to fabrication errors, but increases the number of phase shifters and complexity. Therefore, a new structure that is inherently tolerant to fabrication errors, without increasing the number of phase shifters, is highly desirable.

In this chapter, we propose a robust integrated OUC structure using multiport directional couplers (DCs) and present the design and device characterization of a 4×4 integrated OUC based on the proposed structure.

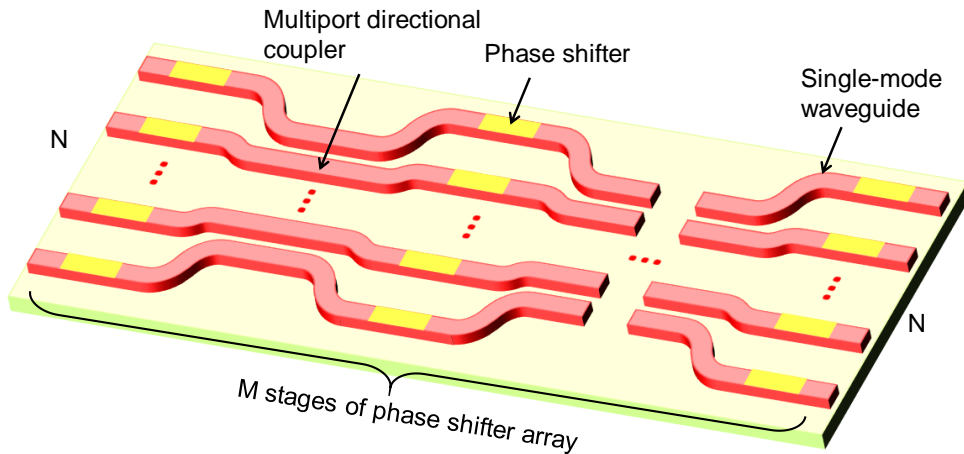


Fig. 4.1. Schematic of the proposed OUC. The OUC consists of cascaded stages of multiport directional couplers and phase shifter arrays.

4.1 Proposed structure

The schematic of the proposed structure is shown in Fig. 4.1, which consists of cascaded stages of $N \times N$ multiport DCs and phase shifter arrays. In each multiport DC,

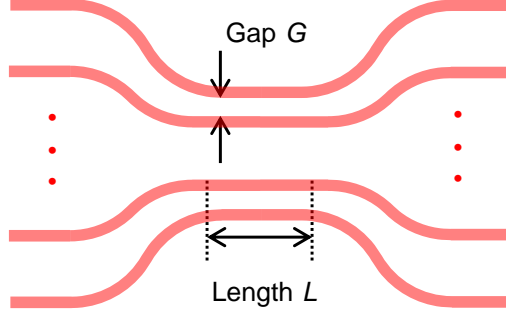


Fig. 4.2. Schematic of the multiport directional coupler. N straight waveguides are placed in parallel to each other with an equal gap of G and a length of L .

N straight waveguides are placed in parallel to each other with an equal gap of G and a length of L , as shown in Fig. 4.2. Similarly, the complex transfer matrix \mathbf{T} , which describes the coupling of the electric fields from the input ports to the output ports, is given by

$$\mathbf{T} = \Phi_M \cdot \mathbf{D} \cdot \Phi_{M-1} \cdots \mathbf{D} \cdot \Phi_1, \quad (4.1)$$

where \mathbf{D} and Φ_i are the complex transfer matrices of the multiport DC and the i -th stage phase shifter array, respectively, and M is the total number of phase shifter arrays. If the propagation loss is ignored, Φ_i is a unitary matrix with only diagonal elements, and \mathbf{D} is a unitary matrix regardless of the precise design of the multiport DC. According to the principle of MPLC, arbitrary unitary transformation can be implemented at least up to some fidelity, using a finite number of optimized phase-manipulating planes separated by some linear canonical transformations [23, 110, 111]. Here, a phase shifter array functions as a reconfigurable transmissive phase-manipulating plane, and the multiport DC provides a specific form of linear canonical transformation [112]. Therefore, using a finite number of phase shifter arrays and multiport DCs, we expect that \mathbf{T} can be configured at least approximately to arbitrary $N \times N$ unitary matrix by optimizing all the phase shifters. The required stage number M ,

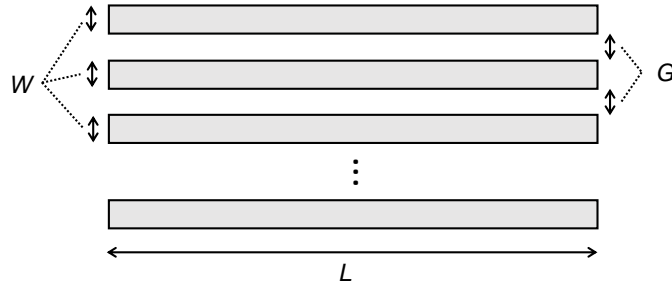


Fig. 4.3. Simulation model of the multiport DC. The curved part is neglected because it only affects the effective L .

however, is limited by the trade-off between fidelity and chip size. An increase in the number of stages increases the fidelity but requires larger chip sizes and increases the optimization complexity. Considering the necessary degrees of freedom, the stage number M should not be less than the port number N . By replacing the MMI coupler with the multiport DC, the port-dependent loss is eliminated because the transformation through the multiport DC is always unitary regardless of its precise design. Therefore, we anticipate that the proposed scheme based on the multiport DC can provide a wider design region to achieve nearly arbitrary unitary transformation.

4.2 Numerical analysis

In order to investigate the validity and robustness of this structure, we numerically analyze the performances of various OUC designs with different values of G and L at the multiport DC. First of all, the complex transfer matrix of the multiport directional coupler \mathbf{D} needs to be derived. Due to the limitation of the coupled-mode theory,

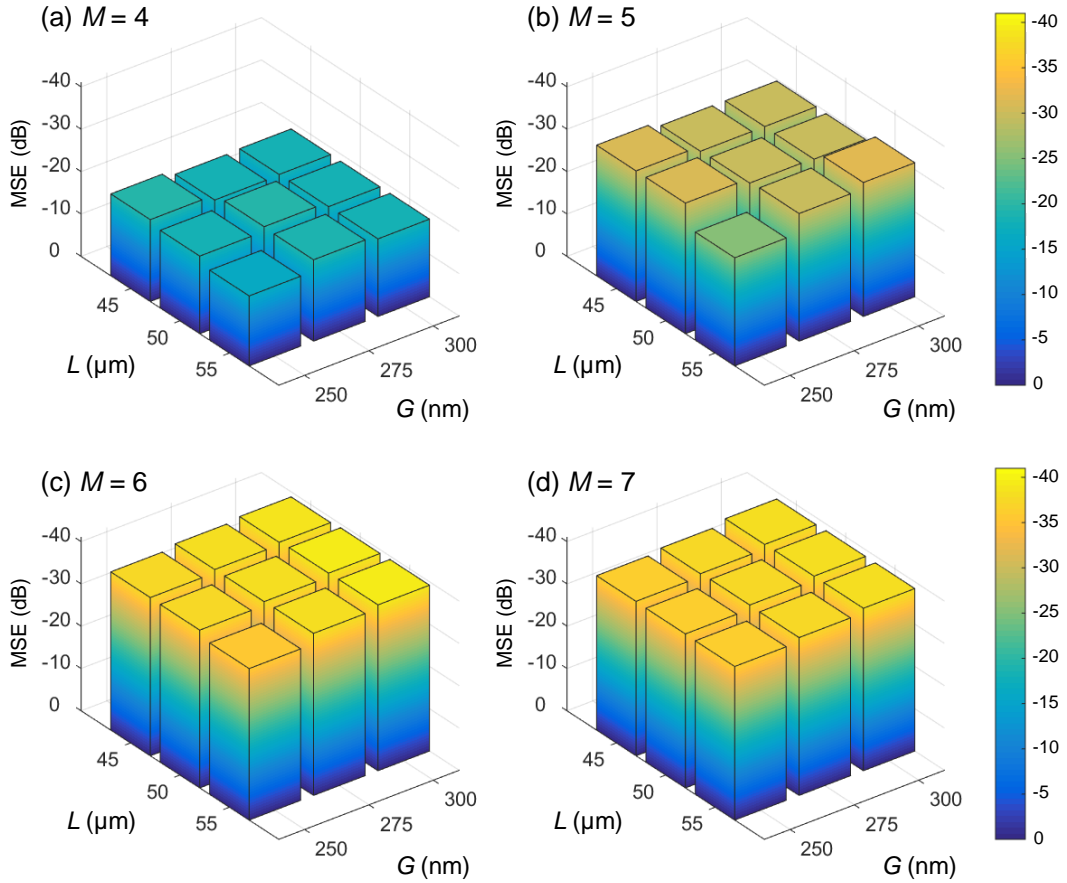


Fig. 4.4. Averaged MSEs after the optimization, under the condition of $N = 4$ and various G , L , and M . The phase accuracy is 0.01 rad.

especially when G is small (< 300 nm) [113], we use EME simulations to obtain \mathbf{D} . Although this structure does not depend on the waveguide material, the simulations are performed on the SOI platform for the sake of simplicity.

The simulation model is shown in Fig. 4.3. The curved part of the multiport DC is neglected because it only affects the effective L and does not change the conclusion of the simulations. According to the foundry, the top-cladding layer is SiO_x (refractive index: ~ 1.501), instead of SiO_2 . As an example, when $W = 460$ nm, $L = 50$ μm and $G = 275$ nm, \mathbf{D} is simulated to be

$$\begin{pmatrix} 0.128 + 0.07j & -0.319 + 0.478j & -0.513 - 0.371j & 0.308 - 0.380j \\ -0.319 + 0.478j & -0.430 - 0.255j & -0.075 + 0.064j & -0.513 - 0.371j \\ -0.513 - 0.371j & -0.075 + 0.064j & -0.430 - 0.255j & -0.319 + 0.478j \\ 0.308 - 0.380j & -0.513 - 0.371j & -0.319 + 0.478j & 0.128 + 0.07j \end{pmatrix}. \quad (4.2)$$

Note that the above matrix is not perfectly unitary, mainly due to the fact that a part of the light is localized between the waveguide cores, which causes a small insertion loss and port-dependent loss.

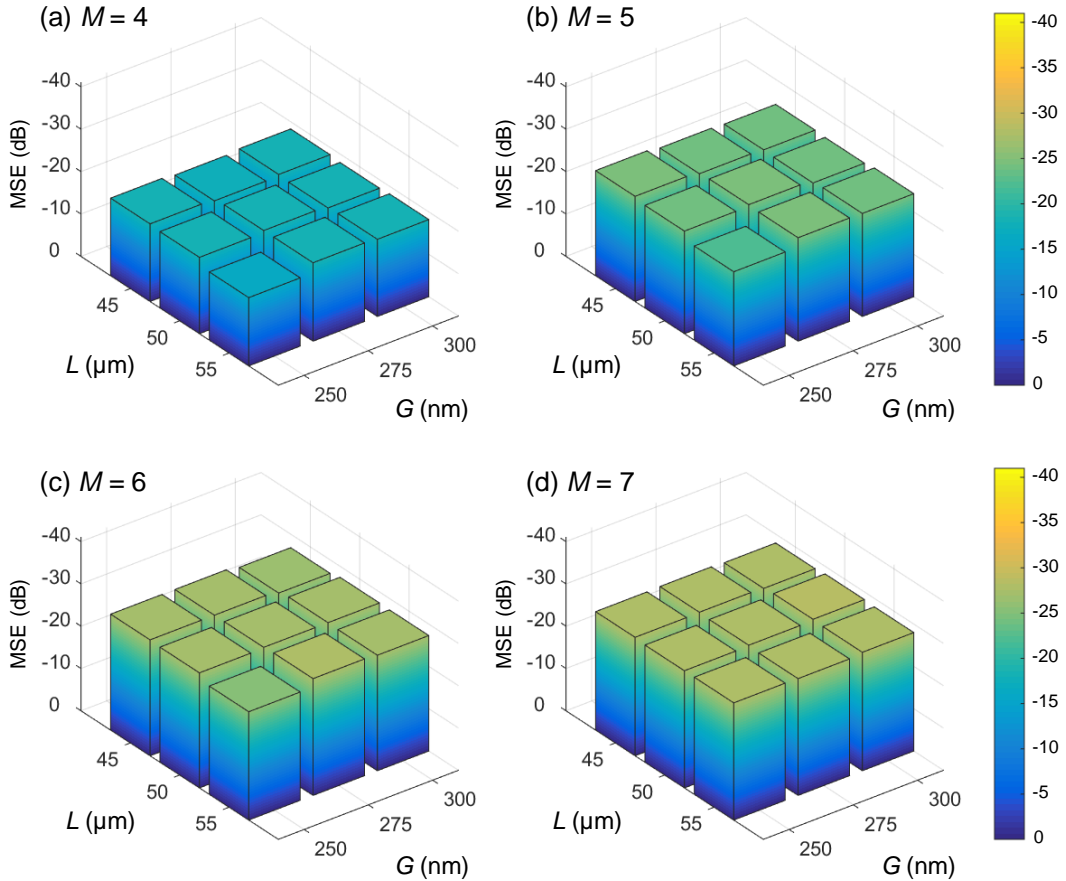


Fig. 4.5. Averaged MSEs after the optimization, under the condition of $N = 4$ and various G , L , and M . The phase accuracy is 0.1 rad.

4.2.1 Mean squared error

We set W to 460 nm and obtain the \mathbf{D} for various G and L . Again, the 100 randomly generated unitary matrices in Sec. 3.2.2 are used as the desired unitary matrix \mathbf{T} , respectively, and the simulated annealing algorithm is used to optimize the phase shifters to obtain the desired \mathbf{T} . Figure 4.4 shows the averaged MSEs after the optimization, under various G , L , and M . The phase accuracy is 0.01 rad. We can see that when increasing M from 4 to 6, the average MSEs become smaller. However, the average MSEs when $M = 7$ are slightly worse than those when $M = 6$. This is due to the small insertion loss associated with \mathbf{D} . Using more stages of the multiport DC increases the insertion loss, so the entire transfer matrix deviates more from the desired unitary matrix when $M = 7$. On the other hand, we can see that the differences of MSE under

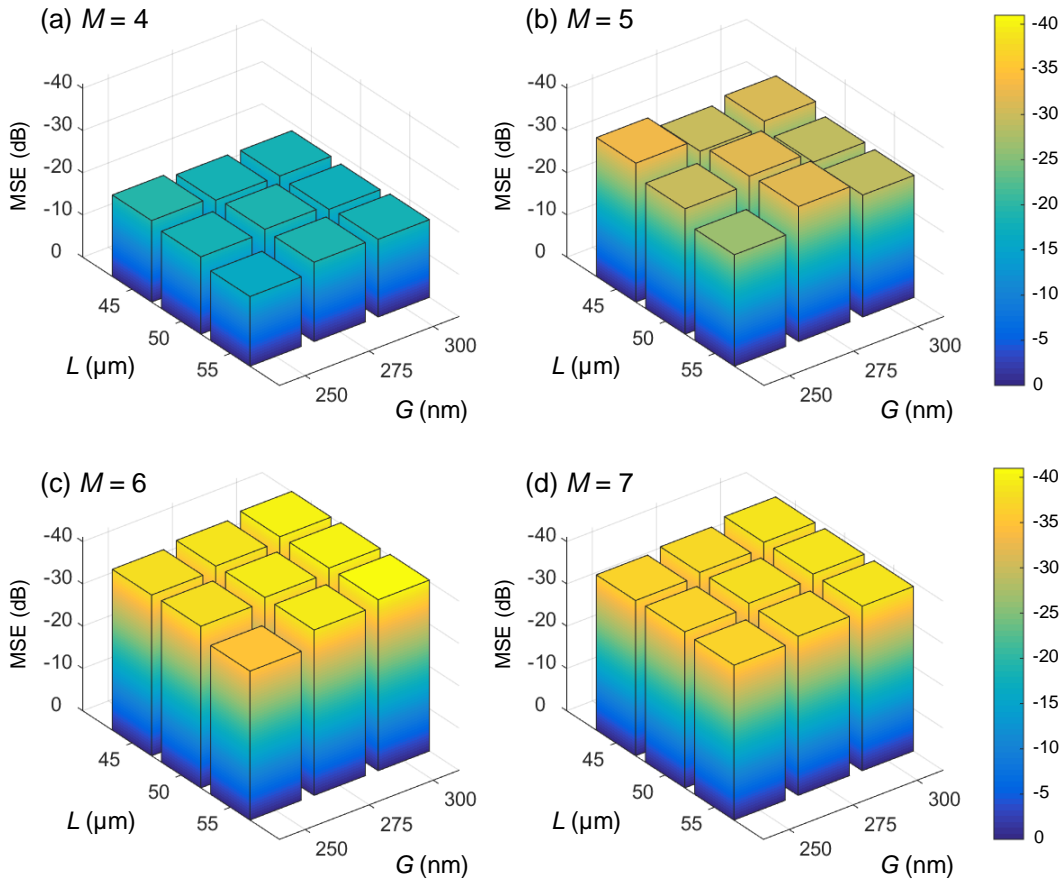
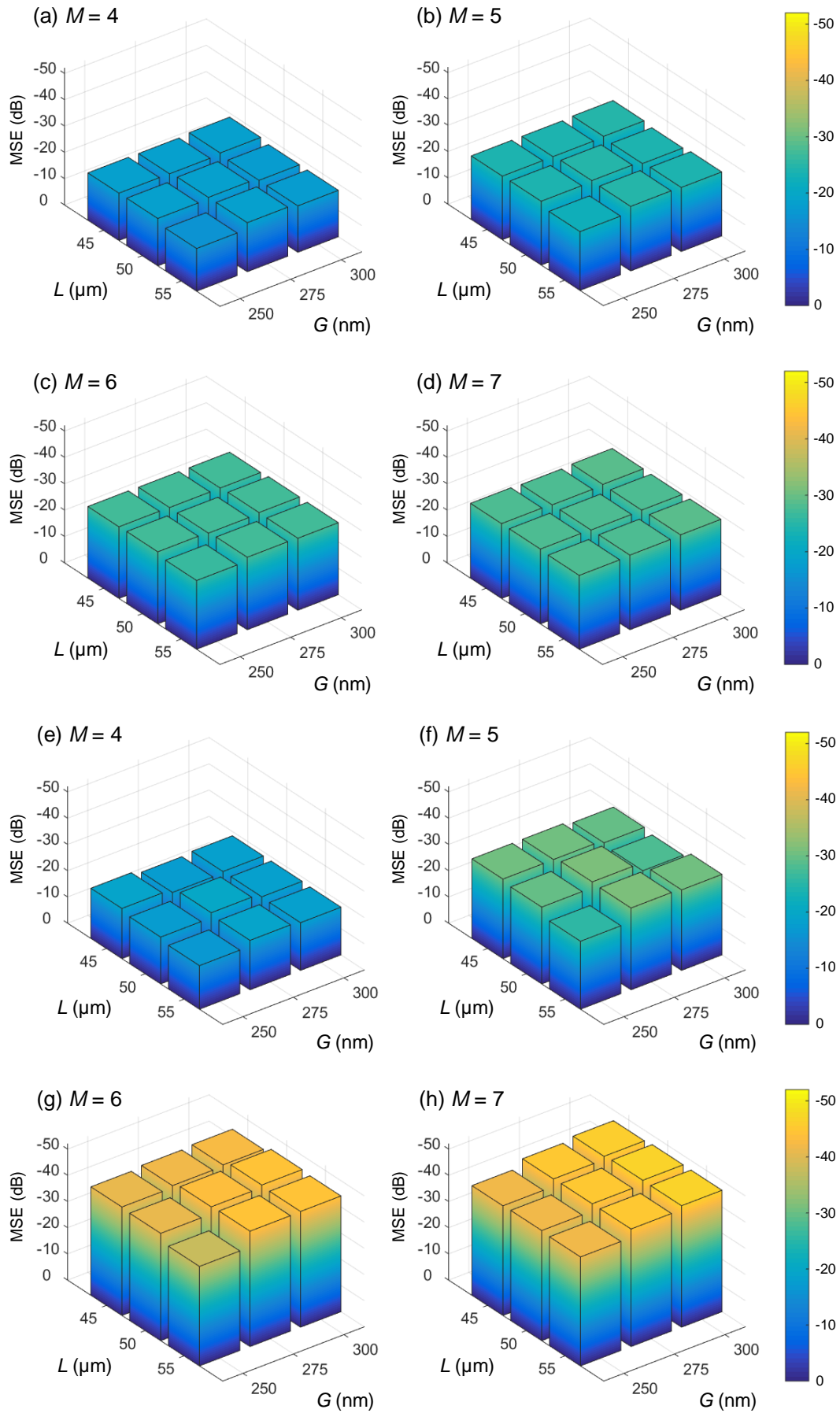


Fig. 4.6. Averaged MSEs after the optimization, under the condition of $N = 4$ and various G , L , and M . The phase accuracy is 0.001 rad.



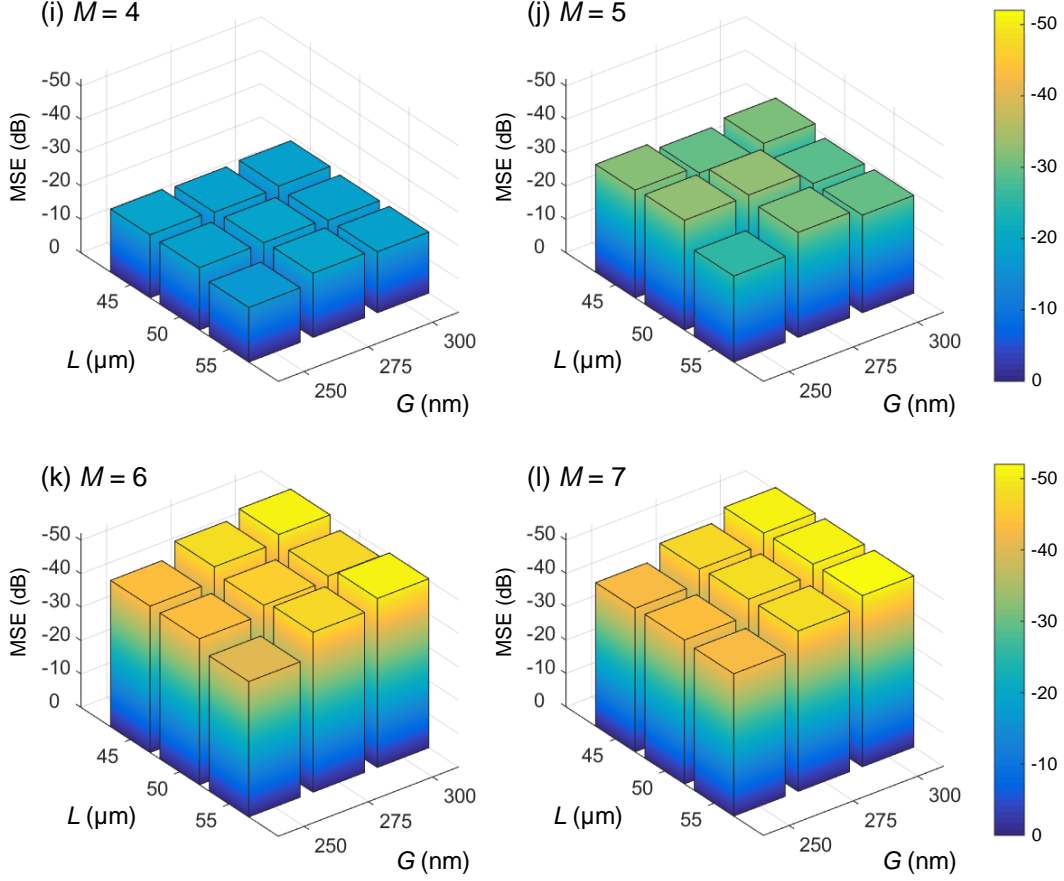


Fig. 4.7. Averaged MSEs after optimizing the phase shifters with \mathbf{D}' . The phase accuracies are (a)-(d) 0.1 rad, (e)-(h) 0.01 rad, and (i)-(l) 0.001 rad, respectively.

different G and L also become smaller when M increases from 5 to 7. We further alter the phase accuracy to 0.1 rad and 0.001 rad, respectively. The results are shown in Fig. 4.5 and Fig. 4.6, respectively. We can observe similar tendencies to the results in Fig. 4.4. If we neglect the insertion loss of the multiport DC and use

$$\mathbf{D}' = \sqrt{\frac{N}{\sum_{i=0}^N \sum_{j=0}^N |D_{ij}|^2}} \mathbf{D} \quad (4.3)$$

to replace \mathbf{D} , the entire transfer matrix becomes closer to a unitary matrix. Figure 4.7 shows the averaged MSEs after optimizing the phase shifters with \mathbf{D}' . Now we can see that the averaged MSEs decrease with an increasing M , which is consistent with the principle of MPLC. Besides, when $M = 7$ and the phase accuracy is 0.01 rad [Fig. 4.7(h)], the MSEs are similar among a wide range of G (250 ~ 300 nm) and L (45 ~ 55 μm). What's more, the results for a varying L and a fixed G (275 nm) is shown in Fig. 4.8. Note that increasing L is equivalent to reducing G , because both strengthen the coupling between adjacent waveguides. We choose to increase L for the sake of

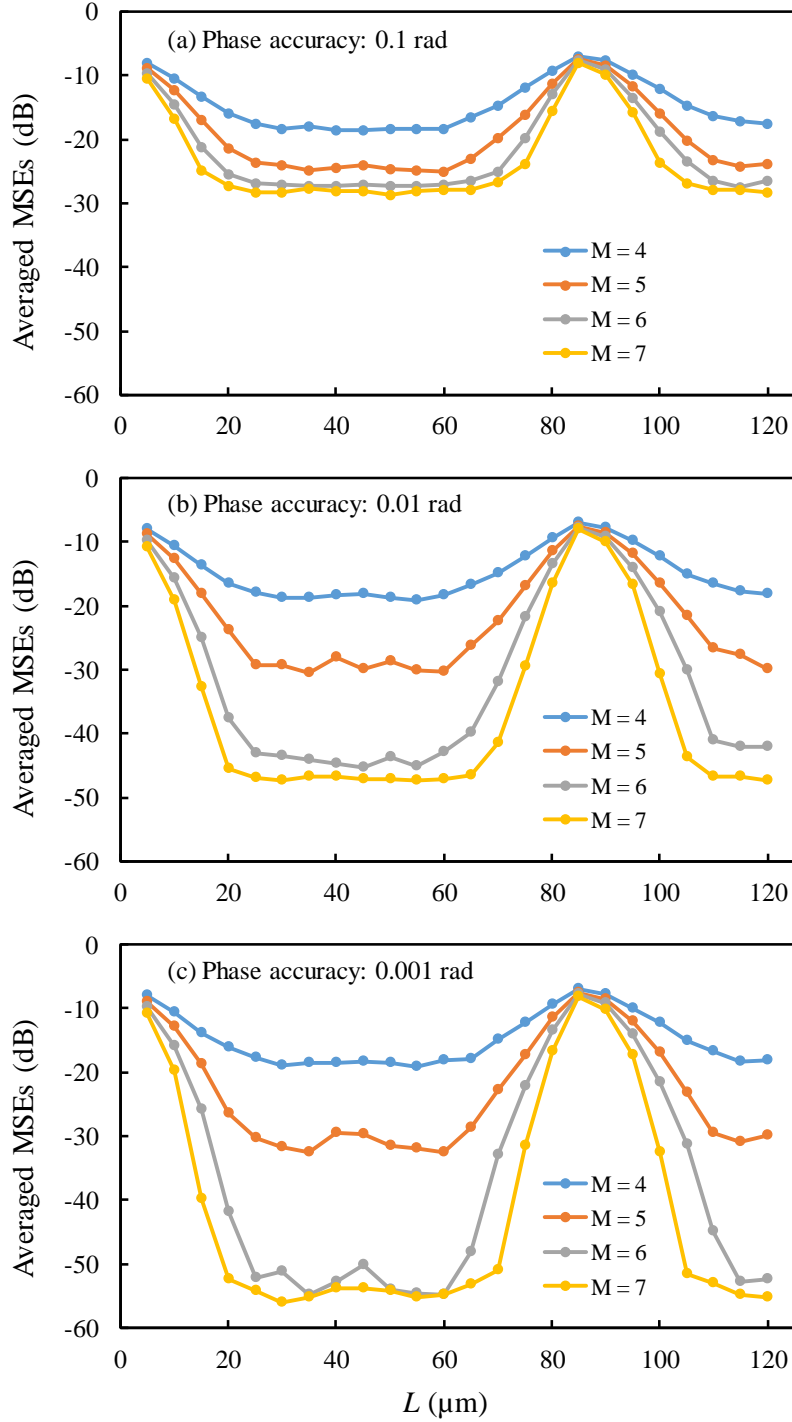


Fig. 4.8. Averaged MSEs when G is fixed at 275 nm and L is varied. The phase accuracies are (a) 0.1 rad, (b) 0.01 rad, and (c) 0.001 rad, respectively.

simplicity. We can see from Fig. 4.8 that when the phase accuracy is 0.01 rad and $M > 4$, a wide range of L can provide a low MSE of less than -20 dB. There are regions where low MSEs cannot be obtained, because the light is not properly split after propagating through the multiport DC. Nevertheless, the wide operating range of L provides the robustness against fabrication errors and great flexibility during the design.

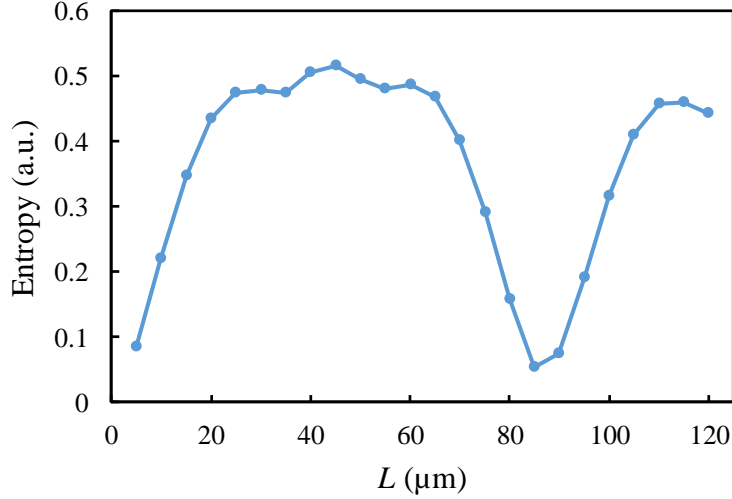


Fig. 4.9. Entropy of coupling as a function of L . G is fixed at 275 nm.

On the other hand, if we use the entropy of coupling to quantitatively describe the extent of coupling induced by the multiport DC:

$$\text{entropy} = -\frac{1}{N} \sum_{i=0}^N \sum_{j=0}^N |D_{ij}|^2 \log_{10} (|D_{ij}|^2) \quad (4.4)$$

we will find the averaged MSE is related to the entropy of coupling. Figure 4.9 shows the entropy as a function of L . Comparing Fig. 4.8 and Fig. 4.9, it is obvious that the MSE improves with the increase in the entropy. Therefore, as a general design rule, we can first set a proper G and waveguide width, then find a region of L where the entropy is relatively large and flat. The middle value of this L region can be used. Following this procedure, the entropy of coupling as a function of L for $N = 8, 16$ is shown in Fig. 4.10. In following calculations, we choose $L = 85 \mu\text{m}$ for $N = 8$ and $230 \mu\text{m}$ for $N =$

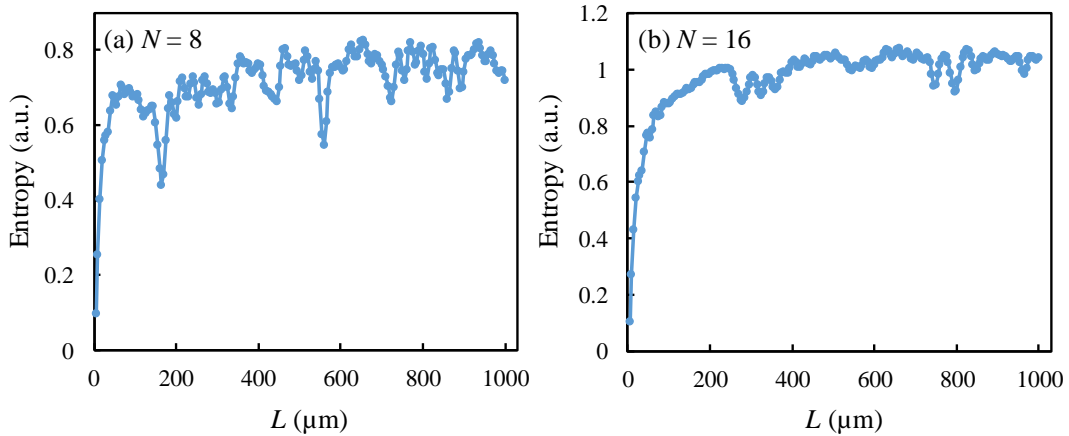


Fig. 4.10. Entropy of coupling as a function of L for $N = 8, 16$. G is fixed at 275 nm.

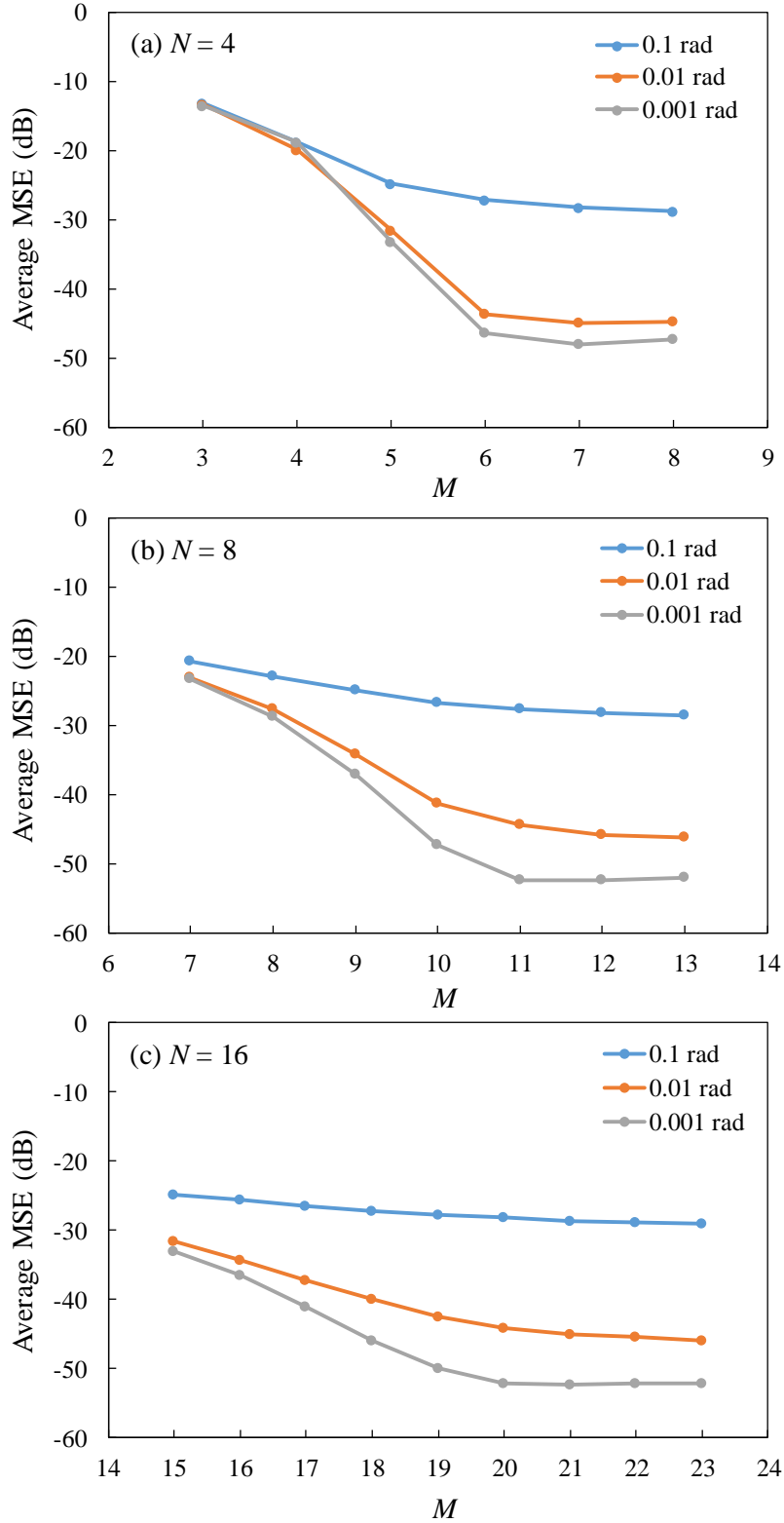
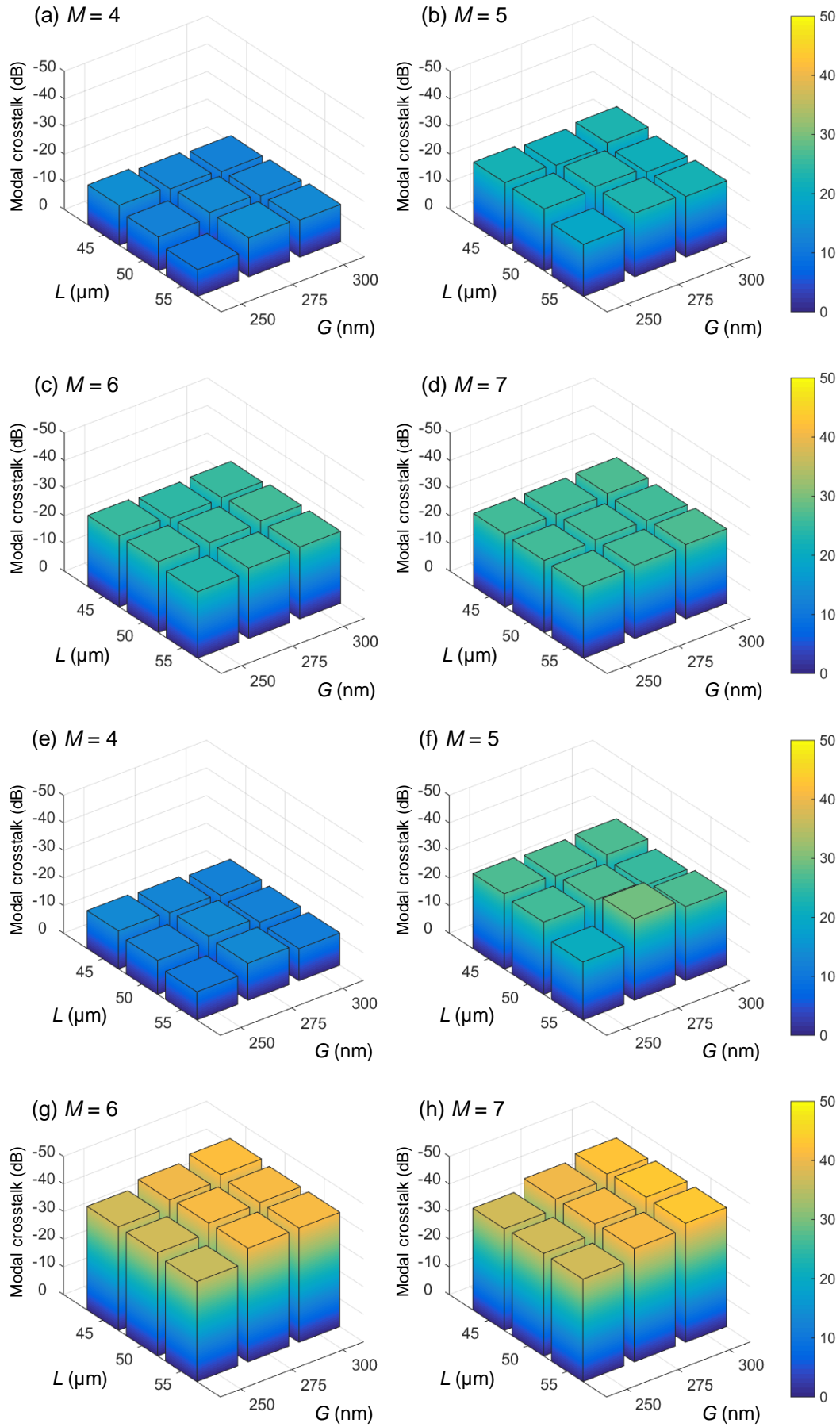


Fig. 4.11. Average MSEs as a function of M , under various conditions. G is fixed at 275 nm. (a) $N = 4$. (b) $N = 8$. (c) $N = 16$.

16, respectively. Using these designs, we further calculate the dependency of MSEs on M . The results are shown in Fig. 4.11. Similar to the results in Fig. 3.4, when M is



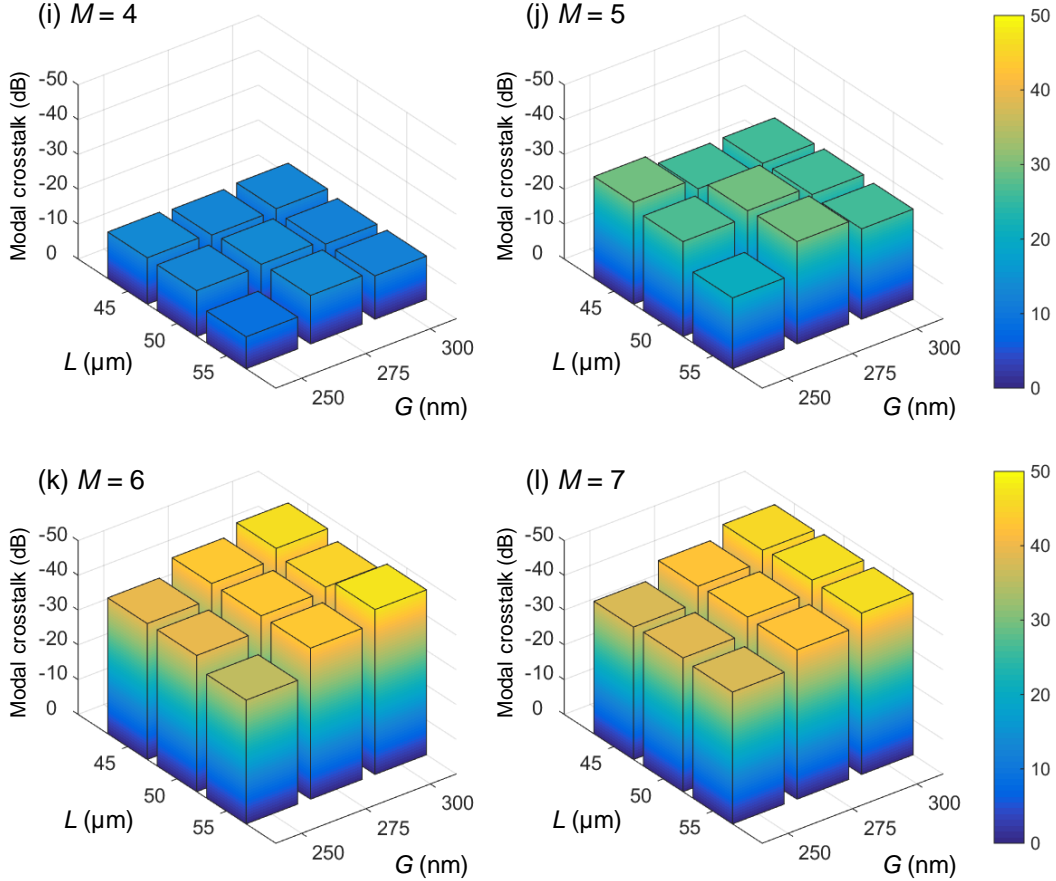


Fig. 4.12. Averaged crosstalks after mode unscrambling. The phase accuracies are (a)-(d) 0.1 rad, (e)-(h) 0.01 rad, and (i)-(l) 0.001 rad, respectively.

increased, the MSEs gradually improve and converge to a certain level. The converged value depends on the phase accuracy. Note that when the phase accuracy is 0.001 rad, after the MSE converges, it slightly increases if we further increase M . This results from the slight port-dependent loss in \mathbf{D}' . However, this may not be a problem in actual devices, since it is hard to achieve the phase accuracy of 0.001 rad due to the thermal drift, on-chip thermal crosstalk, and electronic noises.

4.2.2 Modal crosstalk

Similar to Sec. 4.2.1, we first consider the case of $N = 4$. Again, the 100 unitary matrices are used as the mode coupling matrix, respectively. Figure 4.12 shows the results of mode unscrambling under various conditions. Here, we use \mathbf{D} directly without compensating for the insertion loss, because the modal crosstalk does not depend on the insertion loss. In general, the modal crosstalk decreases when M or the phase accuracy is increased. When $M > 5$ and the phase accuracy is better than 0.1 rad, average modal crosstalk of less than -35 dB can be obtained over a wide range of G

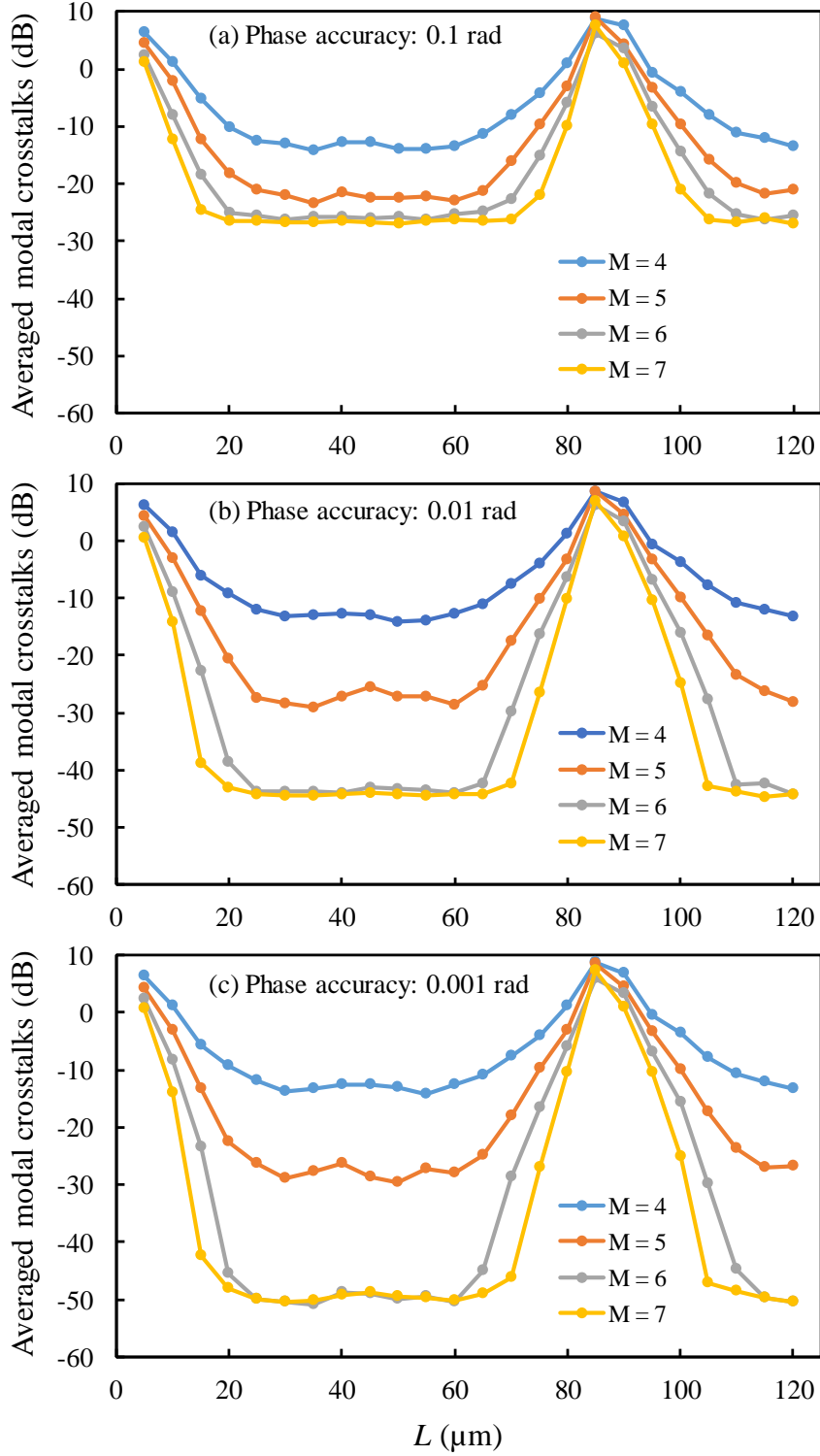


Fig. 4.13. Averaged modal crosstalks after mode unscrambling, when G is fixed at 275 nm and L is varied. The phase accuracies are (a) 0.1 rad, (b) 0.01 rad, and (c) 0.001 rad, respectively.

(250 ~ 300 nm) and L (45 ~ 55 μm). Next, G is fixed at 275 nm, the dependency of average modal crosstalk on L is calculated, as shown in Fig. 4.13. For each M , we can find a large range of L , where the modal crosstalk is relatively low and flat. This range again corresponds to the region where the coupling entropy of the multiport DC is

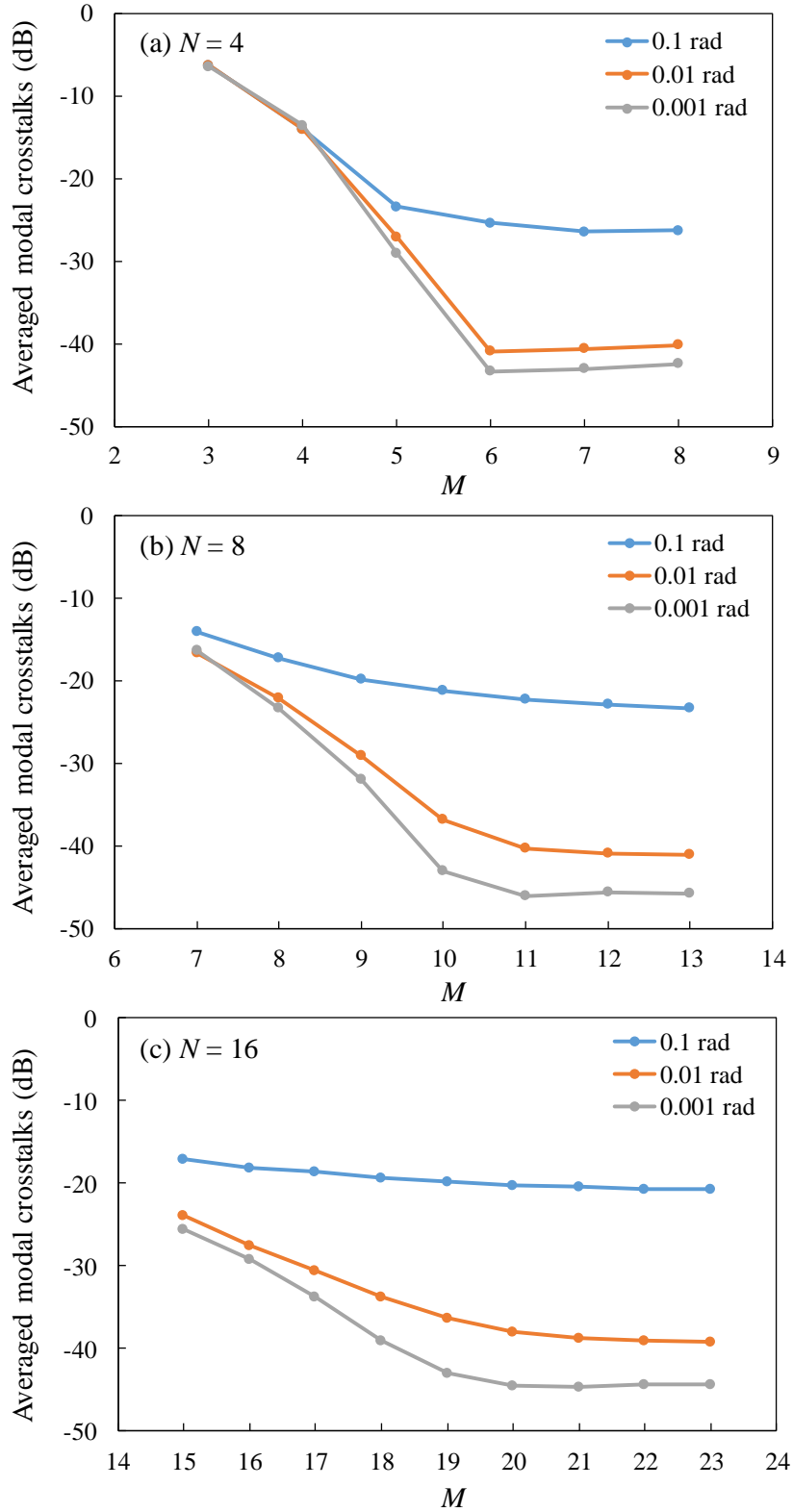


Fig. 4.14. Average MSEs as a function of M , under various conditions. G is fixed at 275 nm. (a) $N = 4$. (b) $N = 8$. (c) $N = 16$.

relatively large and flat. Next, we use the multiport DC designs in Sec. 4.2.1 for $N = 8$ and $N = 16$, respectively, and calculate the dependency of averaged modal crosstalks

on M . The results are shown in Fig. 4.14. The tendency is generally consistent with the results of MSE. We can also observe that in Fig. 4.14(a), the modal crosstalk increases slightly with the increase of M when $M \geq 6$. This is also caused by the slight port-dependent loss in **D**.

4.2.3 Discussion

The results of MSE and modal crosstalk of OUCs using the MMI coupler and the multiport DC are generally similar. However, we can see that for OUCs using the multiport DC, the MSE and modal crosstalk start increasing slightly beyond a certain M . This phenomenon does not show up in the results of OUCs using the MMI coupler because ideal transfer matrices of MMI couplers are used in the analysis. In actual devices, however, the port-dependent loss also exists in an MMI coupler and is most likely larger than that of a multiport DC with the same N . Therefore, this phenomenon should happen for both the structures. Nevertheless, it may not be a problem for actual devices because on one hand it is hard to achieve a high phase accuracy (0.001 rad) due to various noises (thermal drift, thermal crosstalk, electric noise, etc.), on the other hand an overlarge M increases both the control complexity and the chip size.

4.3 Device design and fabricated chip

For the proof-of-concept demonstration, we design a 4×4 OUC on the SOI platform. Based on the numerical analysis in Sec. 4.2, we choose $G = 275$ nm and $L = 50$ μm for the 4×4 multiport DC. The simulated light propagation inside this multiport DC is shown in Fig. 4.15. We can see that the optical power is split unequally at the multiport

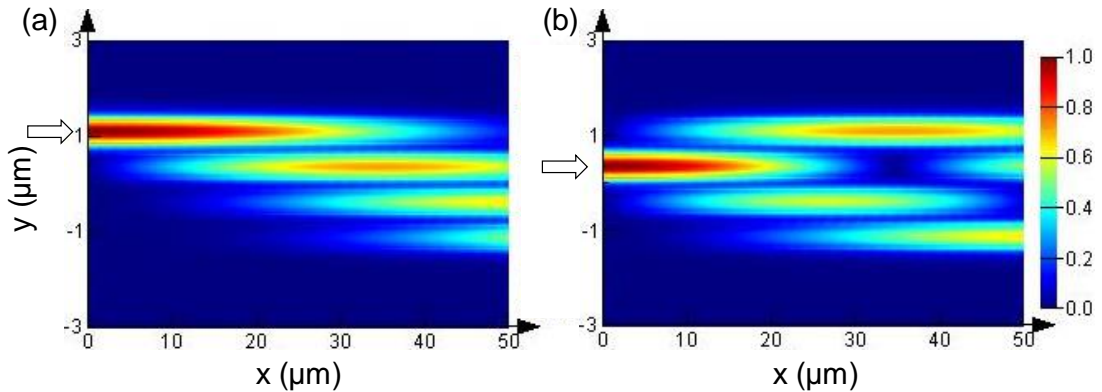


Fig. 4.15. Simulated light propagation inside the 4×4 multiport DC ($G = 275$ nm, $L = 50$ μm). Light is injected into (a) the top waveguide and (b) the second waveguide from the top, respectively.

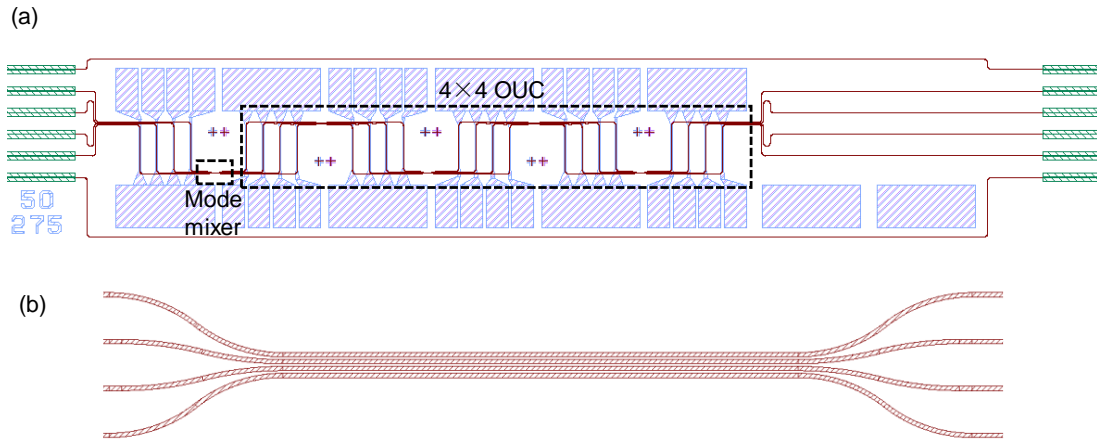


Fig. 4.16. (a) A 4×4 OUC ($N = 4$, $M = 5$) and a 4-mode mixer designed on the SOI platform. (b) Designed 4-port DC ($G = 275$ nm, $L = 50$ μm).

DC output, without the need for equal power splitting. Using this multiport DC and a 4-port phase shifter array as the basic building block, a 4×4 OUC ($N = 4$, $M = 5$) and a 4-mode mixer are designed, as shown in Fig. 4.16. The waveguide width is 460 nm. All the 4 channels are designed to have equal path lengths. The device is then fabricated on a 7.0×1.5 -mm² chip with a 220-nm thick silicon layer and a 3- μm buried oxide (BOX) layer. Figure 4.17 shows the top-view microscope image of the chip and scanning electron microscope (SEM) images of one 4-port DC. The measured G of the actual device is 297 nm, which is 22-nm wider than designed. The TO phase shifters are made of 250- μm -long Ta thin films. The mode mixer is a 4-port DC and is used to emulate the mode coupling effect in FMFs.

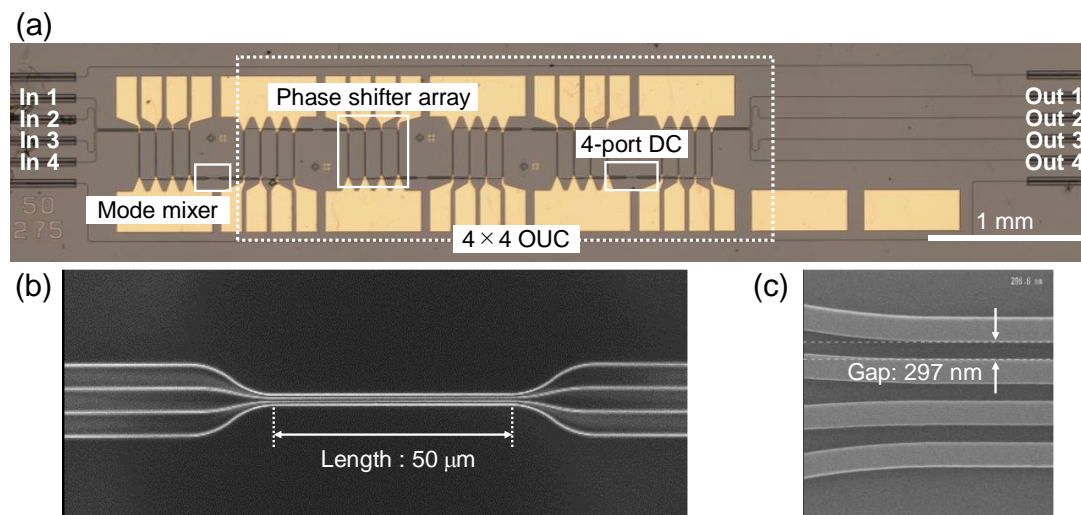


Fig. 4.17. Top-view microscope image (a) of the fabricated chip and scanning electron microscope (SEM) images (b, c) of one 4-port DC. The measured 297-nm G is 22-nm wider than designed.

4.4 Device characterization

4.4.1 Phase shifter

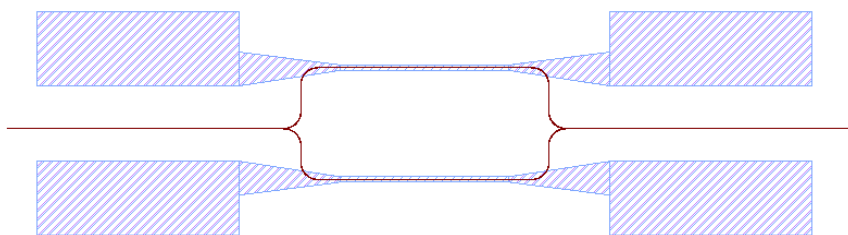


Fig. 4.18. An asymmetric MZI designed on the same chip. The path length difference of the two arms is $30\ \mu\text{m}$.

The phase shifter is characterized using an asymmetric MZI on the same chip, as shown in Fig. 4.18. The path length difference of the two arms is $30\ \mu\text{m}$, which corresponds to an FSR of $\sim 20\ \text{nm}$. Voltages are applied to the phase shifter on one arm and the transmission spectra at the output are measured, as shown in Fig. 4.19. We can see that the 2π -shift voltage is $\sim 4.4\ \text{V}$. By comparing the resistance of this phase shifter with those on the 4×4 OUC, we estimate the 2π -shift voltages of phase shifters on the OUC to be $\sim 4.8\ \text{V}$ (power consumption: $\sim 140\ \text{mW}$).

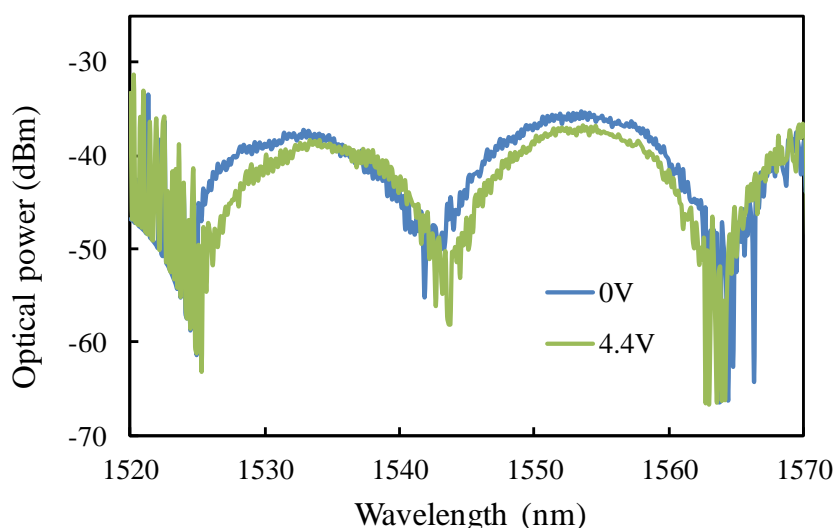


Fig. 4.19. Transmission spectra of the asymmetric MZI under various voltages.

4.4.2 Mode unscrambling experiments

We use the same custom-designed PCB to optimize the phase shifters, in order to unscramble the mixed modes caused by the mode mixer. Note that the output phases are not important in this experiment, so the last phase shifter array is not activated. A

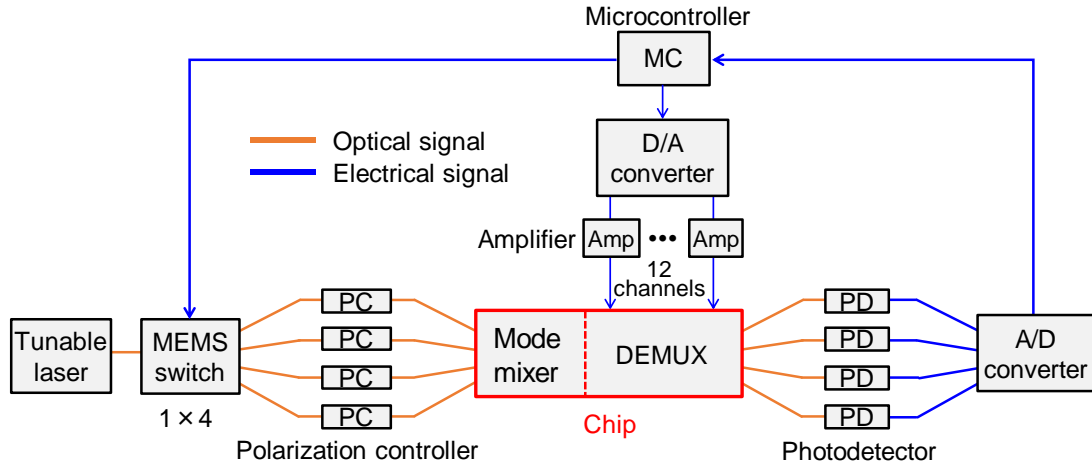


Fig. 4.20. Experimental setup used for the optimization process. Polarizations of the input light are all adjusted to TE. The microcontroller controls the MEMS switch and collects the signals from PDs to implement the simulated annealing algorithm.

similar experimental setup for the optimization is illustrated in Fig. 4.20. TE light is coupled into and out of the chip by two single-mode fiber arrays. Due to large mode mismatch between the fiber and the edge coupler, the average insertion loss of the 4 channels (including on-chip propagation loss and coupling loss at two chip facets) is measured to be 16.4 dB. The insertion loss can be significantly reduced by improving the design of the edge couplers to achieve sub-dB coupling loss [114]. During the optimization, each iteration takes about 5.6 ms, which is mainly limited by the ~ 2 ms switching time of the MEMS switch (~ 4 ms for testing 4 ports). The entire optimization typically converges in approximately 120 seconds (~ 12600 iterations).

Figure 4.21(a) shows the normalized optical power transmittance from each input port (In 1, 2, 3, and 4) to each output port (Out 1, 2, 3, and 4) before optimization, measured at the wavelength of 1550 nm. Severe crosstalk is observed at the output ports. In contrast, Figure 4.21(b) shows the results obtained after the chip is optimized to switch light from In 1, 2, 3, 4 to Out 1, 2, 3, 4, respectively. Similar results are obtained when light from In 1, 2, 3, 4 are switched to Out 4, 1, 2, 3, respectively, as shown in Fig. 4.21(c). The crosstalks in Fig. 4.21(b) and 4.21(c) are suppressed to less than -14.6 dB and -10.5 dB, respectively. The deviation from the numerical analysis can be attributed to the fact that each phase shifter can only be driven up to 1.3π , due to the limitation of the driver circuit. Furthermore, the measured transmission spectra before and after optimizing the chip at 1550 nm are shown in Fig. 4.22. The insertion loss of In 2 is larger than other ports due to the nonuniformity of the diced chip facets. On the other hand, the relatively large wavelength dependency can be attributed to the

wavelength-sensitive multiport DCs. The wavelength dependencies of the MMI coupler and the multiport DC are discussed in Appendix III.

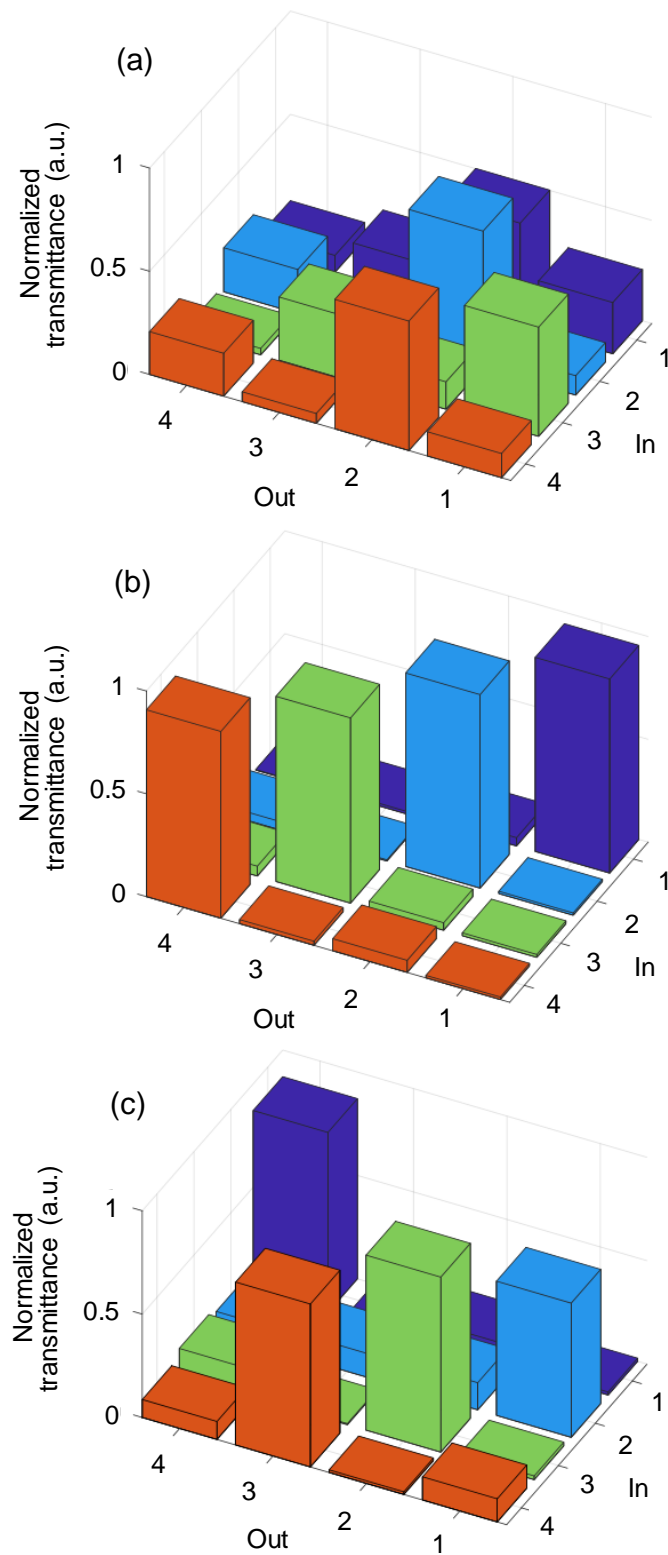
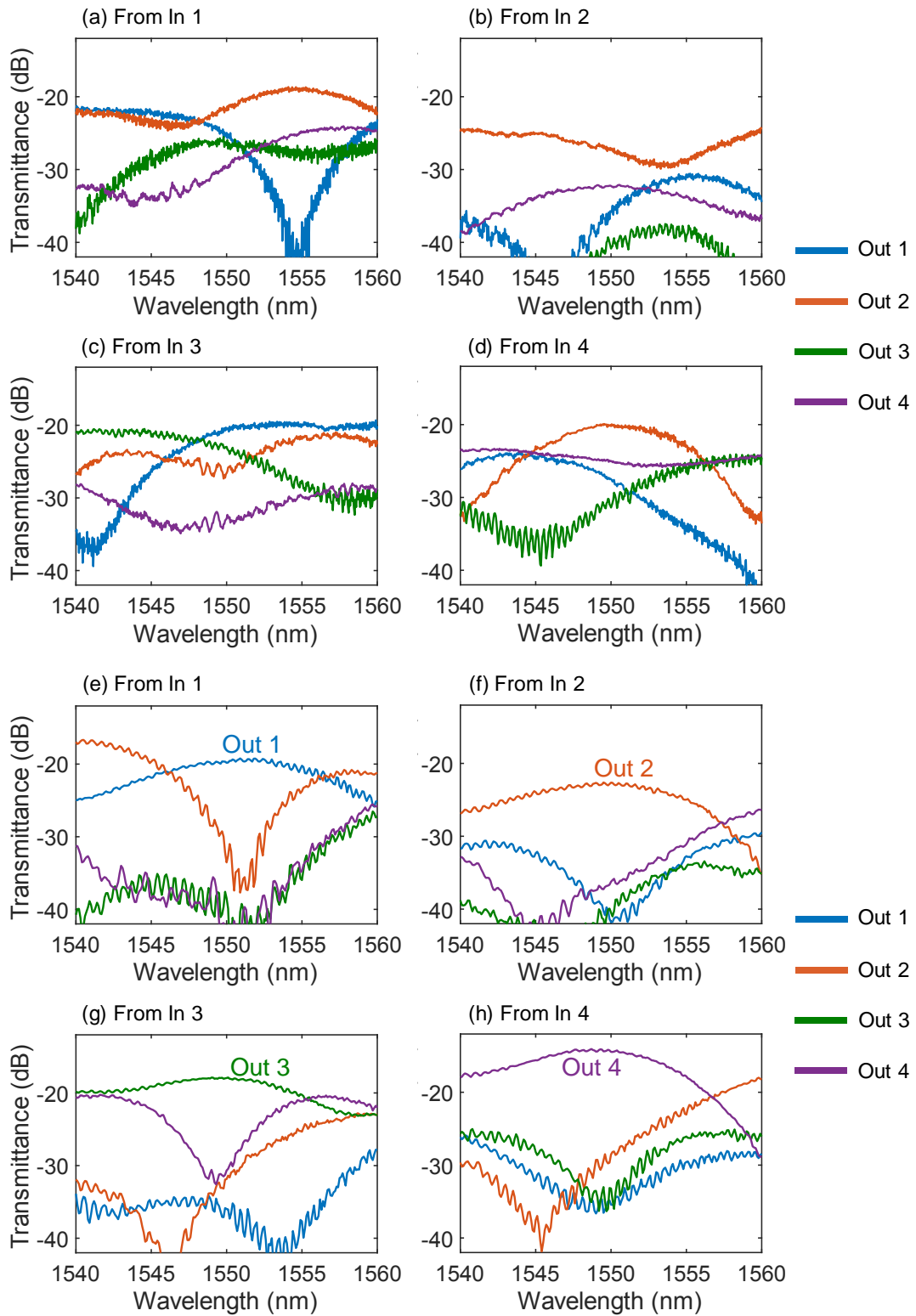


Fig. 4.21. Measured optical power transmittances at the wavelength of 1550 nm from each input port to each output port (a) before optimization, (b) after optimization to switch In 1, 2, 3, 4 to Out 1, 2, 3, 4, respectively, and (c) after optimization to switch In 1, 2, 3, 4 to Out 4, 1, 2, 3, respectively.



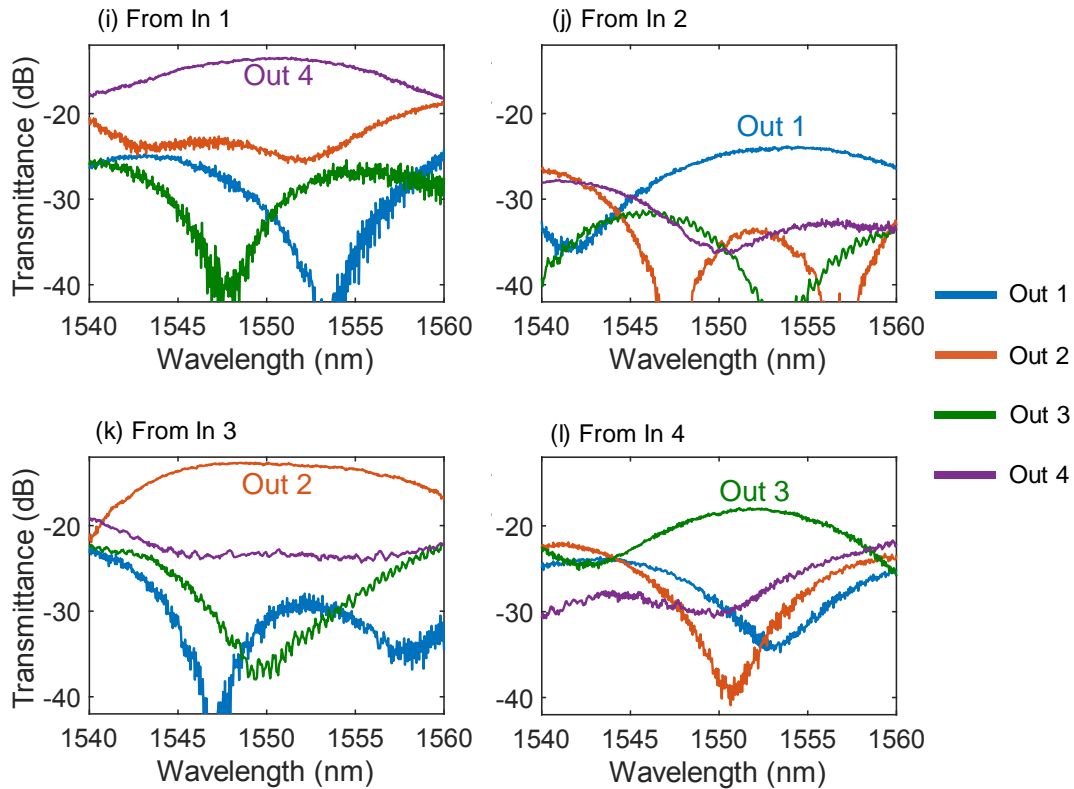


Fig. 4.22. Measured transmission spectra from each input port to each output port (a-d) before optimization, (e-h) after optimization to switch In 1, 2, 3, 4 to Out 1, 2, 3, 4, respectively, and (i-l) after optimization to switch In 1, 2, 3, 4 to Out 4, 1, 2, 3, respectively.

4.4.3 40-Gbps signal demultiplexing

40 Gbps NRZ signals are input to the device and the output signals are characterized using a similar setup shown in Fig. 4.23. Fiber delay lines are used to generate uncorrelated signals at the same wavelength (1550 nm), which are then input to all ports simultaneously. Figure 4.24 shows the eye diagrams observed at Out 1 at various

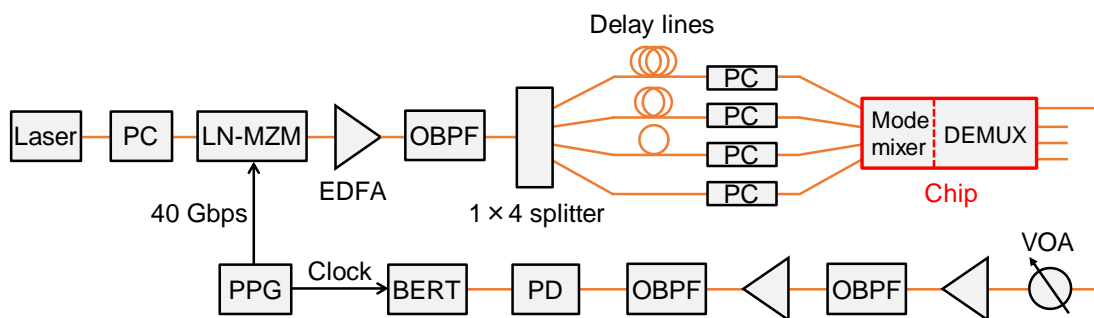


Fig. 4.23. Experimental setup used for demultiplexing of 40 Gbps signals. (PPG: pulse pattern generator; LN-MZM: LiNbO₃ Mach-Zehnder modulator; PC: polarization controller; EDFA: erbium-doped fiber amplifier; OBPF: optical bandpass filter; VOA: variable optical attenuator; BERT: bit error rate tester)

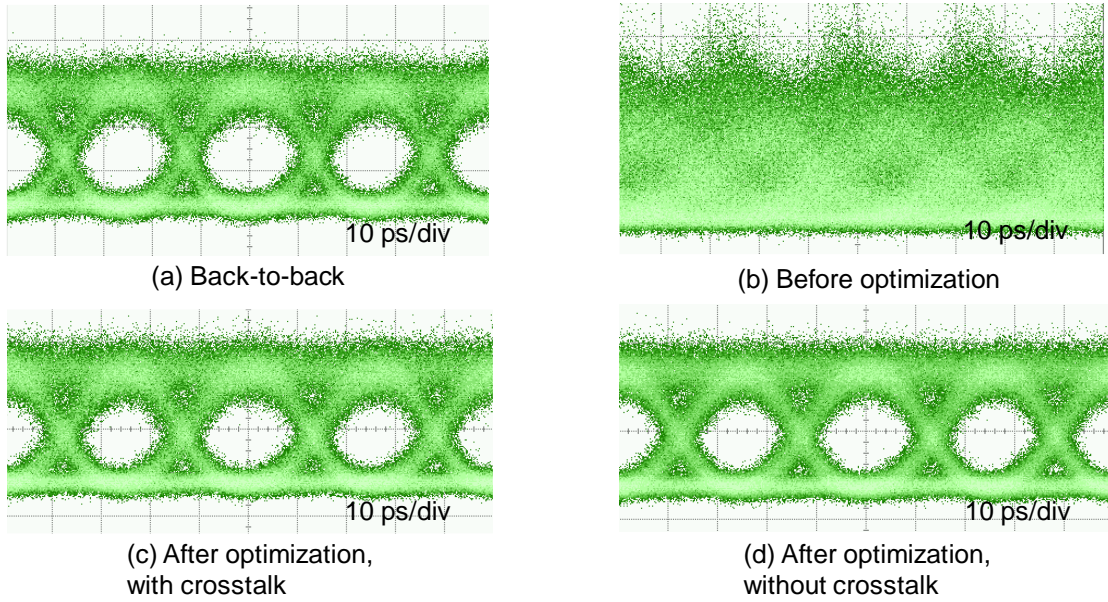


Fig. 4.24. Eye diagrams of 40 Gbps NRZ signals observed (a) back-to-back, (b) before optimization, and (c-d) after optimization with crosstalk from other input ports switched on in (c) and off in (d).

conditions. Before optimization [Fig. 4.24(b)], no eye opening is observed due to severe crosstalk from other channels. In contrast, clear eye openings in Fig. 4.24(c) show that the signal from In 1 is successfully demultiplexed to Out 1 after optimization. As a reference, Fig. 4.24(d) shows the case where the input signals to other ports are turned off. The measured BERs at respective conditions are shown in Fig. 4.25. Error-free

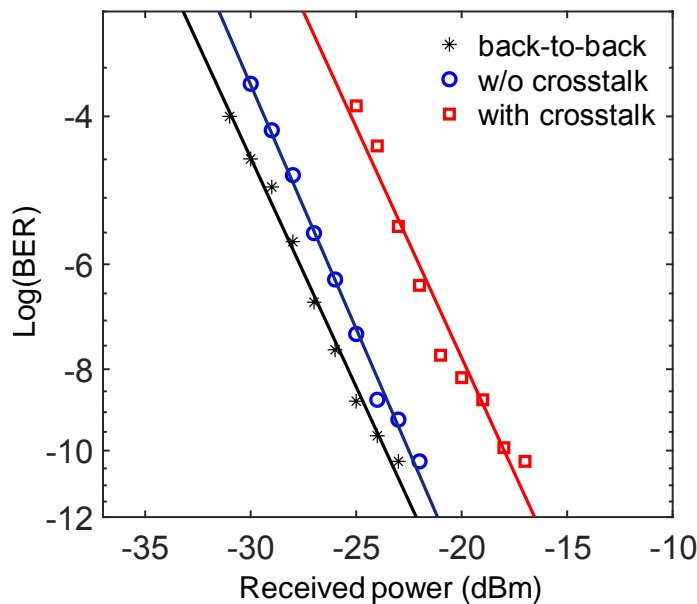


Fig. 4.25. Measured BERs of 40 Gbps NRZ signals at different conditions.

demultiplexing with $\text{BER} < 10^{-9}$ is achieved after optimization. The received power penalty is 6.5 dB, which can be reduced by further improving the extinction ratio.

4.5 Summary

In this chapter, we first proposed a robust integrated OUC using cascaded stages of multiport DCs and phase shifter arrays. From numerical analysis, we showed that given an enough stage number and phase accuracy, the transfer matrix of the OUC can be configured to desired unitary matrices with high fidelities. The robustness is attributed to the inherent property of the multiport DC because the port-dependent loss is nearly eliminated. The numerical analysis further shows that the device performance is related to the entropy of coupling of the multiport DC. We can find a wide range of waveguide gap (G) and length (L) of the multiport DC that can yield a relatively good device performance.

Next, we experimentally demonstrated a 4×4 OUC on a compact silicon chip. By optimizing all the phase shifters, reconfigurable 4-mode demultiplexing was realized with a modal crosstalk of less than -10.5 dB at the 1550-nm wavelength. The relatively large modal crosstalk resulted from the limitation of the driver circuit, which can drive each phase shifter only up to 1.3π . Error-free demultiplexing of 40 Gbps signals was also demonstrated.

Chapter 5 Large-scale integrated OUC using multiport directional couplers

Based on the successful proof-of-concept demonstration in Chapter 4, we present the design and preliminary characterization of a large-scale ($N = 10$) integrated OUC using multiport DCs in this chapter.

5.1 Device design and fabricated chip

The 10-port DC is first designed. Figure 5.1 shows the calculated coupling entropy of the DC as a function of L , when the waveguide width is 400 nm and $G = 300$ nm. Here, the 400-nm waveguide width is used to enhance the coupling between adjacent

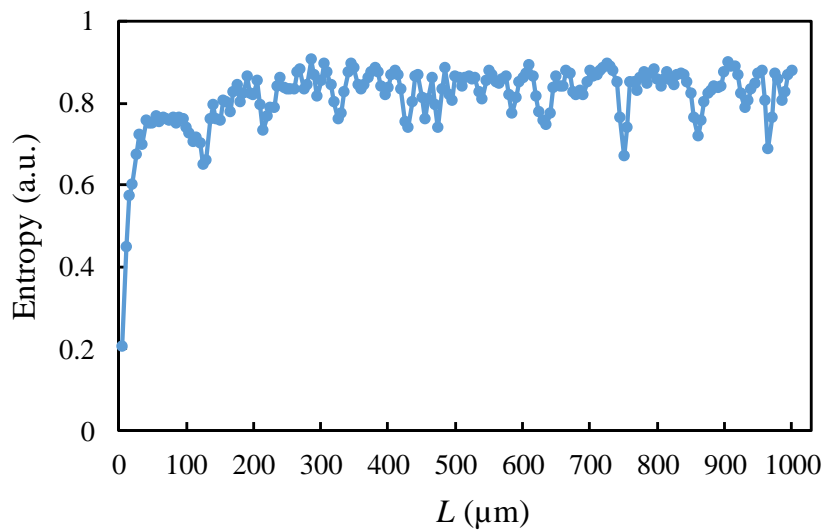


Fig. 5.1. Coupling entropy of the 10-port DC as a function of L , when the waveguide width is 400 nm and $G = 300$ nm.

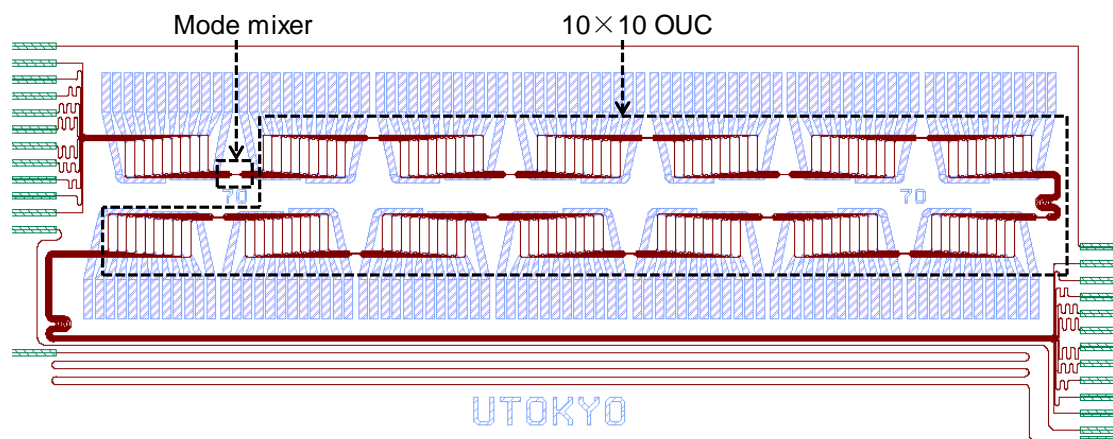


Fig. 5.2. A designed 10×10 OUC. $L = 70 \mu\text{m}$.

waveguides, thus reducing the coupling length. To achieve a balance between a relatively compact size and a low MSE, $L = 60, 70, 80, 90 \mu\text{m}$ are chosen as the design of 10-port DC, respectively.

Four 10×10 OUCs are designed, using $L = 60, 70, 80, 90 \mu\text{m}$, respectively. Figure 5.2 shows the designed device when $L = 70 \mu\text{m}$. Each OUC consists of 13 stages of phase shifter array ($M = 13$). All the 10 channels are designed to have equal path lengths. For each OUC, a mode mixer is added into the input side to scramble the input light. Figure 5.3 shows the microscope image of the device and SEM image of the 10-port DC. The measured G is 298.4 nm , only 1.6-nm narrower than the designed value. The two facets are polished in order to achieve low and uniform coupling losses.

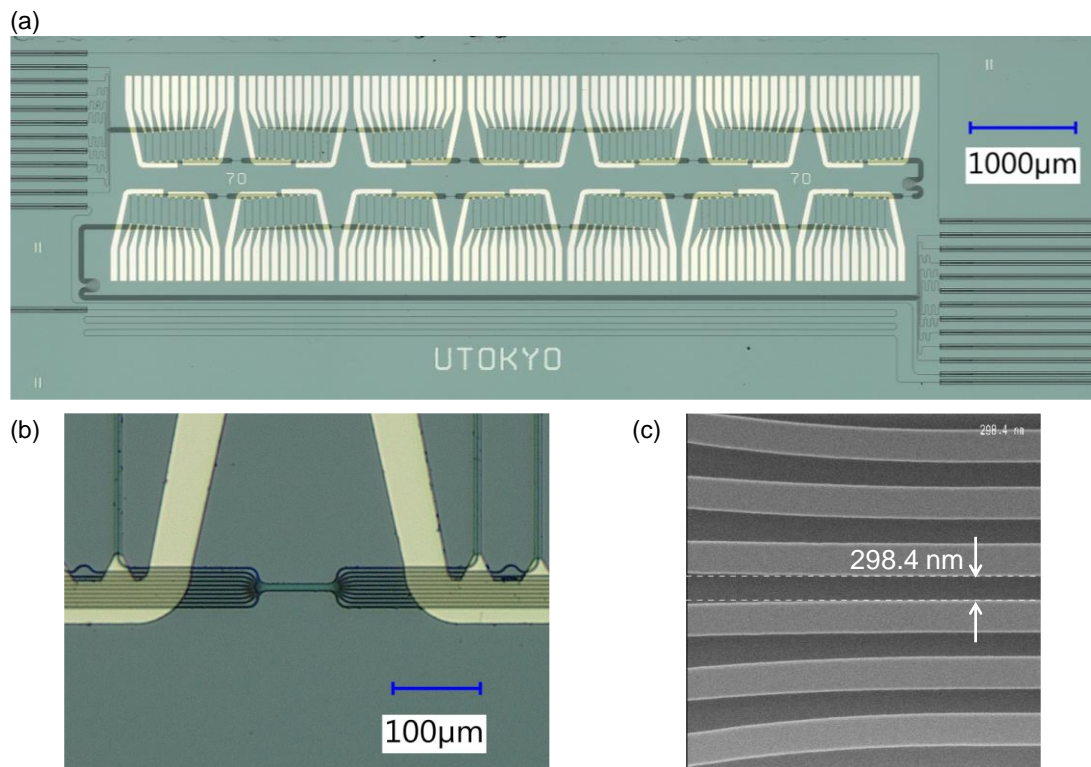


Fig. 5.3. Microscope images of (a) the device and (b) one 10-port DC. (c) SEM image of one 10-port DC. The measured G is 298.4 nm , only 1.6-nm narrower than the designed value.

5.2 Device characterization

5.2.1 Propagation loss and phase shifter

Following the same procedure in previous chapters, the insertion loss of three single-mode waveguides are measured and shown in Fig. 5.4. From the fitting curves, we can

see the propagation loss of single-mode waveguides is 1.9 dB/cm for TE mode and 0.6 dB/cm for TM mode.

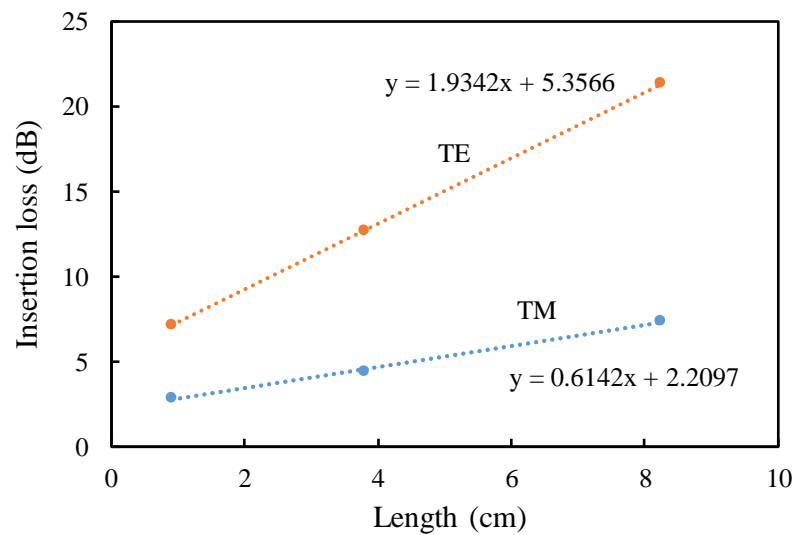


Fig. 5.4. Measured insertion losses of three single-mode waveguides.

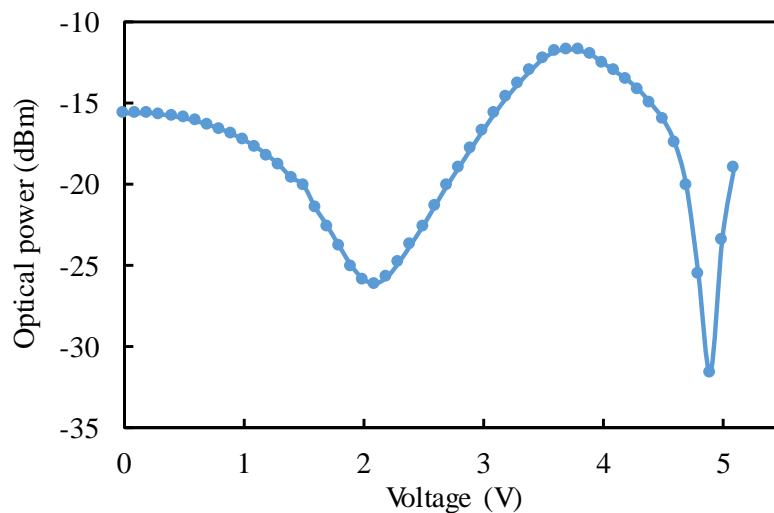


Fig. 5.5. Measured optical output power of a symmetric MZI as a function of the heater voltage.

Figure 5.5 shows the measured optical output power of a symmetric MZI when the voltage applied to the phase shifter on one arm is changed. We can see that the 2π -shift voltage is ~ 4.5 V.

5.2.2 Custom-designed electronic circuit

The previous PCB cannot provide enough output channels for this chip. Therefore, a new electronic circuit is designed to implement the optimization algorithm. In order to flexibly adjust the output voltage, this circuit is divided into two modules: the control module and the amplification module. The control module detects the output signals of

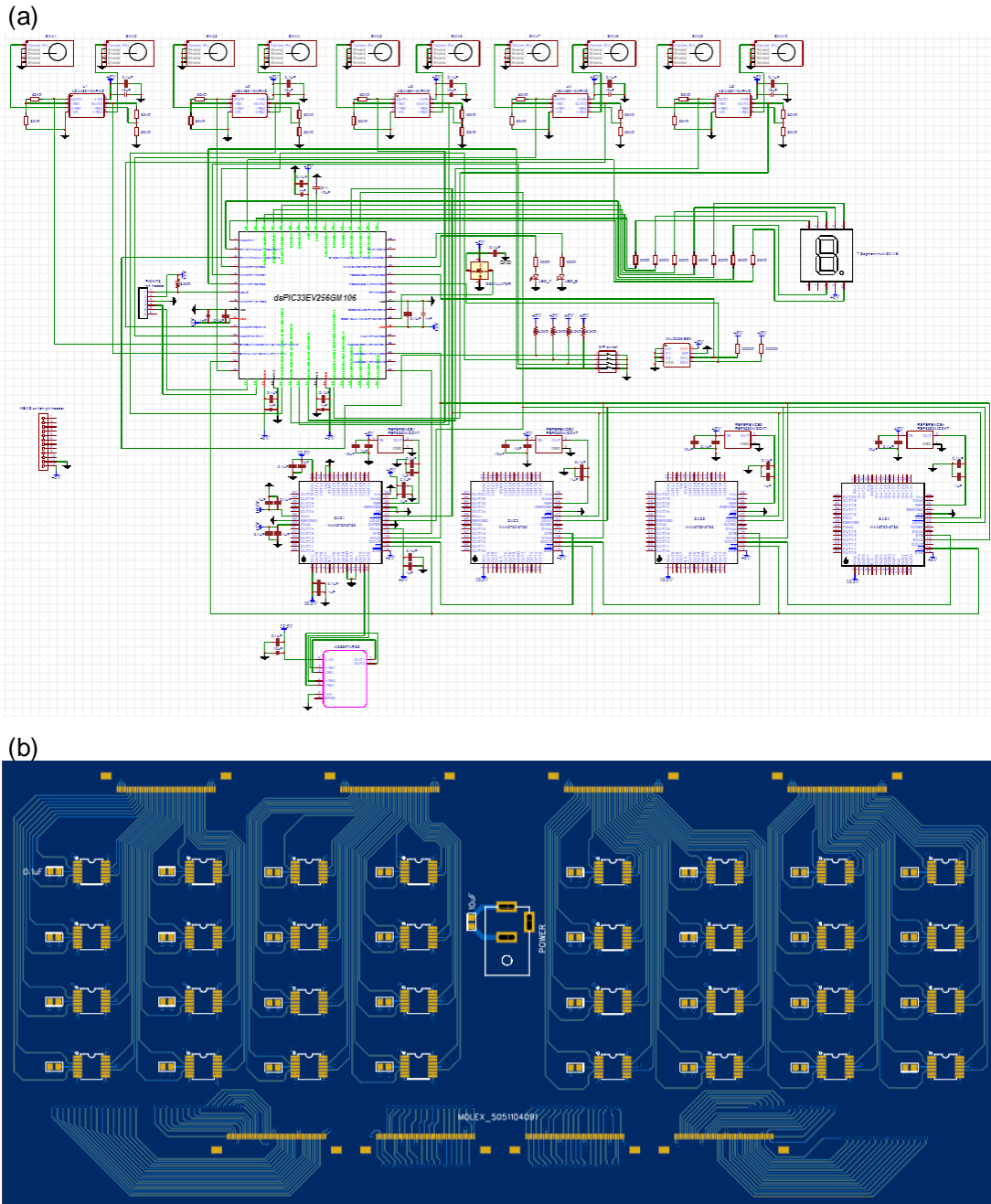


Fig. 5.6. (a) Schematic of the electronic circuit. (b) One designed amplification module.

photodetectors and controls the output voltages of four 32-channel DACs through the SPI communication. The range of the output voltage is 0~5 V. The amplification module consists of operational amplifiers that can provide enough output currents for the phase shifters. The two modules are connected via flexible flat cables. It is easy to design multiple amplification modules, each with a different gain factor, to flexibly adjust the output voltage range of the whole circuit. Figure 5.6(a) and 5.6(b) shows the schematic of the electronic circuit and one designed amplification module, respectively.

5.2.3 Chip packaging

Because a large number of bonding wires are required, the wire bonding process is done by a commercial service. The image of one packaged chip, after attaching the chip to a custom-designed chip carrier and the wire bonding process, is given in Fig. 5.7.

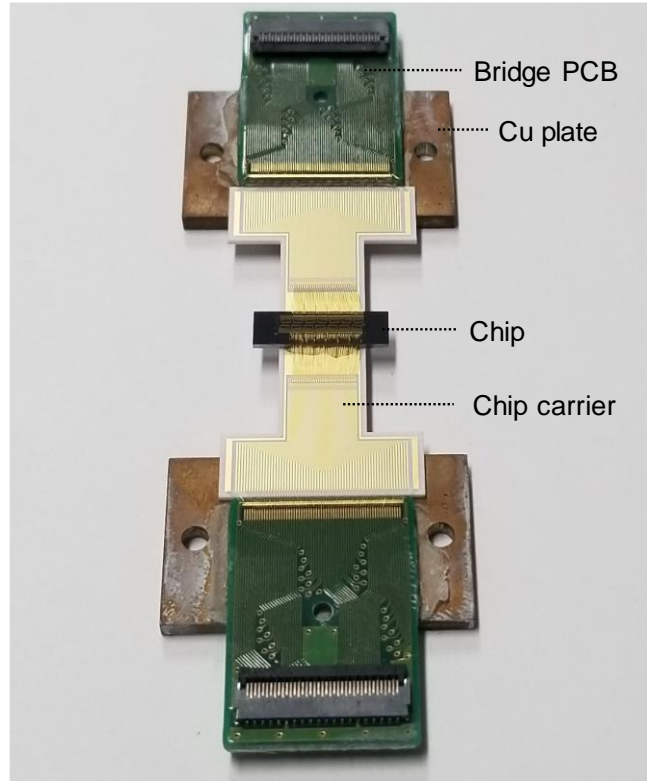


Fig. 5.7. Image of one packaged chip.

5.3 Comparison with previous work

The comparison with previous work is listed in Tab. 5.1. As we can see, most of the demonstrated OUCs are applied into optical communication and quantum information processing. There is one demonstration on the optical neural network, but the scale is too small and cannot be put into practical use. Applying OUCs into these areas is still in the exploratory phase due to the small scale and the relatively inferior device performance. The current priority is to increase the scale of OUC, which requires efforts in the chip design, fabrication, packaging, and external control circuits. The 6×26 chip from MIT is the largest-scale chip up to now, but does not obey the standard $N \times N$ structure, which may limit its applications. The 10×10 chip in this work is the largest-scale chip which obeys the standard $N \times N$ structure. We expect that this OUC structure may find important applications when the scale reaches 30×30 .

Table 5.1. Comparison with previous work

Scale	Material	Applications	Scheme	Institute	Year	Ref.
2×2	InP	Optical Commu.	MZI	Politecnico di Milano	2016	[20]
3×3	Si	Optical Commu.	MMI coupler	This work	2018	
4×4	Si	Optical Commu.	MZI	Politecnico di Milano	2017	[16]
4×4	Si	Optical Commu.	MZI	Ghent Univ./IMEC	2016	[19]
4×4	Si	Optical Commu.	Multiport DC	This work	2019	
4×4	Si	Optical neural network	MZI	MIT	2017	[18]
6×6	SiO ₂	Quantum Informa.	MZI	Univ. of Bristol	2015	[15]
8×8	SiN	Quantum Informa.	MZI	Univ. of Twente	2018	[21]
10×10	Si	To be characterized	Multiport DC	This work	2020	
6×26	Si	Quantum Informa.	MZI	MIT	2017	[17]

5.4 Summary

In this chapter, we presented the design and preliminary characterization results of a 10×10 OUC using multiport DCs, and compared the devices in this work with previous demonstrations. While all other works are based on the MZI structure, the OUCs demonstrated in this work presented different methods that have unique advantages, such as the wide operation bandwidth or robustness against fabrication errors. What's more, the 10×10 OUC in this work is the largest-scale device which obeys the standard $N \times N$ structure.

Chapter 6 Conclusions

In this thesis, we have proposed and demonstrated novel integrated OUCs based on MPLC.

The first OUC structure consists of cascaded stages of MMI couplers and phase shifter arrays. We studied the feasibility of this scheme through numerical analysis and showed that given enough stages and phase accuracy, this structure can implement desired unitary matrices with low MSEs and unscramble coupled modes with low modal crosstalks. Next, we demonstrated a 3×3 OUC on the SOI platform and applied it into mode unscrambling. Owing to the symmetric structure and the relatively wavelength-insensitive MMI couplers, reconfigurable 3-mode demultiplexing was realized with a wavelength-dependent loss of less than 3 dB and a modal crosstalk less than -10 dB over a 23-nm wavelength range. Error-free demultiplexing of 40 Gbps signals was successfully demonstrated. This wide operation bandwidth of this OUC makes it useful in optical communication systems.

The second OUC structure consists of cascaded stages of multiport DCs and phase shifter arrays. From the numerical analysis, we showed that this structure is robust against fabrication errors and is easy to design. We can find a wide range of waveguide gap (G) and length (L) of the multiport DC that can yield a relatively good device performance. Next, we demonstrated a 4×4 OUC on the SOI platform based on this structure. Reconfigurable 4-mode demultiplexing was realized with a modal crosstalk of less than -10.5 dB at the 1550-nm wavelength. After this proof-of-concept demonstration, we further designed a 10×10 integrated OUC and preliminarily characterized the device. This scheme is beneficial in realizing large-scale OUCs for quantum information processing, and optical neural networks.

Further efforts should be put into finding the rigorous proof that these structures are universal to arbitrary unitary transformation, although the numerical results indicate that it can realize a large number of desired unitary transformation with a sufficiently-high fidelity. Besides, the optimization time needs be reduced, which requires more efficient optimization algorithms, pilot modulation signals, or/and on-chip monitoring channels. In addition, the device performance, such as the modal crosstalk after mode unscrambling, needs be improved. This requires improvements in both the photonic

chip and the external electronic circuit. For example, the on-chip thermal crosstalk between adjacent phase shifters can be suppressed by heat isolation trenches; DACs and ADCs with higher precisions can be used to reduce electronic noises. For even larger-scale devices, for example, $N = 20$, the power consumption of phase shifters needs be further reduced. Moreover, advanced packaging techniques, such as the flip-chip bonding, can be used to reduce the size of the chip module.

Appendix I Source codes for numerical analysis

As an example, the following Python codes optimize a 4×4 OUC using MMI couplers, in order to configure the transfer matrix of the OUC to desired unitary matrices. These codes are based on Python 3.6 and require external packages specified in the code.

- <RandomUnitary.py>

```
# File description: this code randomly generates 100 unitary matrices and saves them in
# a .npy file.
```

```
import numpy as np
from scipy.stats import unitary_group
N=4
filename = 'TargetMatrices_4by4'
Matrix_list = []
for i in range(100):
    Matrix_list.append(unitary_group.rvs(N))
np.save(filename, Matrix_list)
```

- <Main_4by4_5stages.py>

```
# File description: this code optimizes all the phase shifters to configure the transfer matrix
# of the OUC to 100 unitary matrices generated in <RandomUnitary.py>. The phase
# accuracy is 0.01 rad and  $M = 5$ .
```

```
import numpy as np
import random
import copy
import os
```

```
#####
# Ideal transfer matrix of the MMI coupler
#####
MMI = np.zeros((4,4), dtype = complex)
a = np.cos(np.pi/4) + np.sin(np.pi/4)*1.0j
MMI[0, 0] = 0.5
MMI[1, 0] = -0.5 * a
MMI[2, 0] = 0.5 * a
MMI[3, 0] = 0.5
MMI[0, 1] = -0.5 * a
MMI[1, 1] = 0.5
MMI[2, 1] = 0.5
MMI[3, 1] = 0.5 * a
MMI[0, 2] = MMI[3, 1]
MMI[1, 2] = MMI[2, 1]
MMI[2, 2] = MMI[1, 1]
MMI[3, 2] = MMI[0, 1]
MMI[0, 3] = MMI[3, 0]
MMI[1, 3] = MMI[2, 0]
```

```

MMI[2, 3] = MMI[1, 0]
MMI[3, 3] = MMI[0, 0]

#####
# Global variables
#####
# matrix dimension: 4*4
N = 4
# 5-stage phase shifter arrays
num_phaseshifter = N*(N+1)
N_trial = num_phaseshifter*10
ps_start = np.array([[1,0,0,0], [0,1,0,0], [0,0,1,0], [0,0,0,1]], dtype = complex)

#####
# Functions
#####
def mse(m: np.ndarray, n: np.ndarray):
    MSE = 0
    for i in range(N):
        for j in range(N):
            MSE = MSE + abs(m[i][j] - n[i][j])**2
    return MSE/(N*N)

#####
# Main body
#####
# load 100 random target matrices
target_list = np.load('TargetMatrices_4by4.npy')
MSE_list = []

for i in range(100):
    # phase accuracy
    L = 0.01
    # temperature
    T = 1
    # boundary
    b = 30

    # set all phase shifts to zero
    ph = [[0,0,0,0], [0,0,0,0], [0,0,0,0], [0,0,0,0], [0,0,0,0]]
    # initialize phase shifter arrays
    ps = [copy.deepcopy(ps_start), copy.deepcopy(ps_start), copy.deepcopy(
        ps_start), copy.deepcopy(ps_start), copy.deepcopy(ps_start)]

    # jump times
    N_jump = 0

    target = target_list[i]
    y = ps[4] @ MMI @ ps[3] @ MMI @ ps[2] @ MMI @ ps[1] @ MMI @ ps[0]
    f = mse(y, target)

    while (b>0) and (T>0.000000000001):
        N_jump = 0
        # repeat N_trial times

```

```

for j in range(N_trial):
    # randomly choose a phase shifter
    m = random.randrange(N+1)
    n = random.randrange(N)

    # generate a random phase shift
    ph_temp = copy.deepcopy(ph[m][n])
    ph[m][n] = ph[m][n] + random.randint(-b,b)*L
    if ph[m][n] > 2*np.pi:
        ph[m][n] = ph[m][n] - 6.28
    elif ph[m][n] < 0:
        ph[m][n] = ph[m][n] + 6.28

    # store current values and calculate the new MSE
    ps_temp = copy.deepcopy(ps[m])
    ps[m][n][n] = np.complex(np.cos(ph[m][n]), np.sin(ph[m][n]))
    y_temp = ps[4] @ MMI @ ps[3] @ MMI @ ps[2] @ MMI @ ps[1] @ MMI
              @ ps[0]
    f_temp = mse(y_temp, target)

    # jump or not
    if f_temp < f:
        f = f_temp
        y = copy.deepcopy(y_temp)
        N_jump = N_jump + 1
    else:
        if np.exp((f-f_temp)/T) > random.random():
            f = f_temp
            y = copy.deepcopy(y_temp)
            N_jump = N_jump + 1
        else:
            ph[m][n] = ph_temp
            ps[m] = copy.deepcopy(ps_temp)
    if N_jump > N_trial/2.0:
        T = T / 2
    else:
        b = b - 1
print('i='+str(i)+' MSE='+str(f)+' ('+str(10.0*np.log10(f))+dB)')
MSE_list.append(f)

```

```

#####
# Save results into files
#####
# save results into a .npz file
name = 'MMI_4by4_5stages'
np.save(name, MSE_list)

```

```

# save results into a .txt file
filename = name + '.txt'
file = open(filename, 'w')
for element in MSE_list:
    file.write(str(element)+'\n')
file.close()

```

Appendix II Source code written into the microcontroller

C codes are written into the microcontroller (PIC18F46K22) to implement the simulated annealing algorithm. The following code shows the main part of the source codes. Some functions and the initialization of the microcontroller are omitted due to the limited space.

```
<Heater_SA.c>
#define _XTAL_FREQ 64000000
#define SPI_RX_IN_PROGRESS 0x0
#define Num_heater 10

extern unsigned short HeaterVoltage[32] = {0};

#include <stdio.h>
#include <stdlib.h>
#include <xc.h>
#include <time.h>
#include <math.h>
#include <stdbool.h>
#include <stddef.h>
#include <stdint.h>

uint8_t SPI1_Exchange8bit(uint8_t data)
{
    SSP1CON1bits.WCOL = 0;
    SSP1BUF = data;
    while(SSP1STATbits.BF == SPI_RX_IN_PROGRESS);
    return (SSP1BUF);
}

void ch(char i)
{
    // channels of the optical switch
    switch(i)
    {
        case 0: {PORTB = 0b00000000; break;}
        case 1: {PORTB = 0b00010000; break;}
        case 2: {PORTB = 0b00010010; break;}
        case 3: {PORTB = 0b00000001; break;}
        case 4: {PORTB = 0b00001001; break;}
        case 5: {PORTB = 0b00100001; break;}
    }
}

char ADC_channel(char i)
{
    switch(i)
```

```

    {
        case 0: {return 0b00001; break;}
        case 1: {return 0b00100; break;}
        case 2: {return 0b00101; break;}
        case 3: {return 0b00110; break;}
        case 4: {return 0b00111; break;}
        case 5: {return 0b01000; break;}
    }
}

unsigned short ADC_Conversion()
{
    // start the conversion
    ADCON0bits.GO_nDONE = 1;
    unsigned short vin = 0x0000;
    while (ADCON0bits.GO_nDONE);
    vin = (vin | ADRESH) <<8;
    vin = vin | ADRESL;
    return vin;
}

double OneAcquisition()
{
    // 1. from channel 1 → channel 3, ADC conversion
    // 2. add ADC conversion results, return the result
    unsigned short PD_voltage_int[3];
    float PD_voltage[3];
    for (unsigned char i=0; i<3; i++)
    {
        ch(i);
        ADC_SelectChannel(ADC_channel(i));
        __delay_ms(1);
        PD_voltage_int[i] = ADC_Conversion();
        PD_voltage[i] = (double)PD_voltage_int[i]/(double)1024*2.5*Channel_loss(i);
    }
    return PD_voltage[0]+PD_voltage[i]+PD_voltage[2];
}

void HeaterSet(unsigned char DAC_channale, unsigned short Voltage)
{
    unsigned char data_high, data_middle, data_low;
    data_high = DAC_channel;
    data_low = (Voltage<<2) & 0b11111100;
    data_middle = 0b11111111 & (Voltage>>6);
    data_middle = 0b11000000 & data_middle;
    PORTAbits.RA0 = 0;
    __delay_us(0.1);
    SPI1_Exchange8bit(data_high);
    SPI1_Exchange8bit(data_middle);
    SPI1_Exchange8bit(data_low);
    PORTAbits.RA0 = 1;
}

void main(void)
{

```

```

SYSTEM_Initialize();
__delay_ms(100);

// set boundary and simulation temperature
repeat: unsigned short b = 600;
double T = 10;
int MAX_voltage = 3441;
int N_trial = Num_heater*10;
int N_jump = 0;

// seed for rand()
volatile unsigned char value = 0x00;
unsigned uint16_t address = 0x00;

// Initial figure of merit
double f, f_temp;
ADC_Initialize();
f = OneAcquisition();

// Optimization starts
unsigned char ChooseHeater = 0;
unsigned char DAC[10] = {29, 26, 24, 22, 20, 18, 16, 15, 13, 11};
unsigned short HeaterVoltage_temp = 0;
value = EEPROM_read(address);
srand(value);
while ((b>0)&&(T>0.00000000001))
{
    N_jump = 0;
    EEPROM_write(address, rand() % (0xFF+1));
    for (int i = 0; i<N_trial: i++)
    {
        ChooseHeater = DAC[rand() % Num_heater];
        HeaterVoltage_temp = HeaterVoltage[ChooseHeater];
        HeaterVoltage[ChooseHeater] = HeaterVoltage[ChooseHeater] + (-b+rand()%(2*
            b+1));
        while(HeaterVoltage[ChooseHeater]>MAX_voltage)
        { HeaterVoltage[ChooseHeater]=HeaterVoltage[ChooseHeater]-MAX_voltage; }
        while(HeaterVoltage[ChooseHeater]<0)
        { HeaterVoltage[ChooseHeater]=HeaterVoltage[ChooseHeater]+MAX_voltage; }
        HeaterSet(ChooseHeater, HeaterVoltage[ChooseHeater]);
        f_temp = OneAcquisition();
        if (f_temp > f)
        {
            f = f_temp;
            N_jump = N_jump + 1;
        }
        else if (f_temp < f)
        {
            if(exp((f_temp-f)/T)>(rand()/(double)RAND_MAX))
            {
                f = f_temp;
                N_jump = N_jump + 1;
            }
            else
            { HeaterVoltage[ChooseHeater] = HeaterVoltage_temp; }
        }
    }
}

```



```

    }
}
if((float)N_jump > ((float)N_trial/2))
{
    T = T/2;
    // LED_T on and off
    PORTCbits.RC1 = 1;
    __delay_ms(1);
    PORTCbits.RC1 = 0;
}
else
{
    b = b - 10;
    // LEB_B on and off
    PORTCbits.RC2 = 1;
    __delay_ms(1);
    PORTCbits.RC2 = 0;
}
}

// Optimization finished
PORTCbits.RC1 = 1;
PORTCbits.RC2 = 1;
__delay_ms(100);

// Save results into EEPROM
address = 0x01;
for (int i=0; i<Num_heater; i++)
{
    unsigned char temp_high, temp_low;
    temp_low = HeaterVoltage[DAC[i]] & 0xFF;
    temp_high = (HeaterVoltage[DAC[i]]>>8 & 0xFF);
    EEPROM_write(address, temp_high);
    address++;
    EEPROM_write(address, temp_low);
    address++;
}

// Keep the current condition
while (1) { }
return;
}

```

Appendix III Wavelength dependencies of the MMI coupler and the multiport DC

From the experimental results, we can see that the multiport directional coupler (DC) is more wavelength-sensitive than MMI coupler. This is because a larger part of light exists in the cladding region in the DC than in the MMI coupler due to the narrower waveguide width of the DC, and the ratio of light in the cladding region is more sensitive to the change of wavelength in the DC. Therefore, the effective refractive indices of modes in the DC are more sensitive to the change of wavelength.

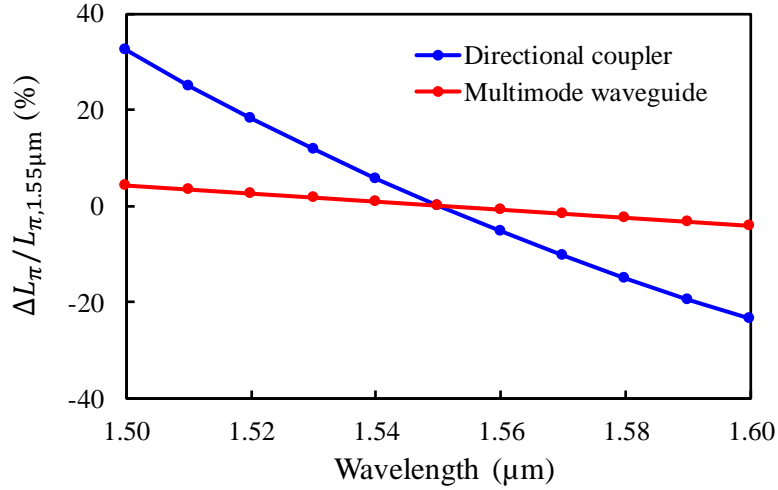


Fig. III.1. Change of L_π with respect to L_π at the 1.55- μm wavelength.

Take a 2×2 DC and a 2×2 MMI coupler for example, the beat length L_π can be calculated by

$$L_\pi = \frac{\pi}{\beta_0 - \beta_1}, \quad (\text{III.1})$$

where β_0 and β_1 are the propagation constants of the two lowest-order modes (or supermodes for the DC) and are given by

$$\beta = n_{\text{eff}} \frac{2\pi}{\lambda}. \quad (\text{III.2})$$

The wavelength dependency can be evaluated by the change of L_π at different wavelengths. We first use FDM simulations to obtain β_0 and β_1 of a 2×2 silicon DC (waveguide width: 460 nm, gap: 300 nm) and a 5- μm -wide multimode silicon waveguide, then calculate L_π at different wavelengths. Figure III.1 shows the change

of L_π with respect to L_π at the 1.55- μm wavelength. We can see that within the wavelength range of 1.5 ~ 1.6 μm , L_π of the DC changes -23% ~ 32% with respect to the value at 1.55 μm , while it is only -4% ~ 4% for the multimode waveguide. Therefore, the wavelength dependency of the 2 \times 2 DC is significantly stronger than that of the 2 \times 2 MMI coupler.

Bibliography

- [1] D. A. B. Miller, "All linear optical devices are mode converters," *Optics Express*, vol. 20, no. 21, pp. 23985-23993, 2012.
- [2] D. J. Richardson, J. M. Fini and L. E. Nelson, "Space-division multiplexing in optical fibres," *Nature Photonics*, vol. 7, pp. 354-362, 2013.
- [3] R. Olshansky, "Mode coupling effects in graded-index optical fibers," *Applied Optics*, vol. 14, no. 4, pp. 935-945, 1975.
- [4] C. R. Doerr, "Proposed architecture for MIMO optical demultiplexing using photonic integration," *IEEE Photonics Technology Letters*, vol. 23, no. 21, pp. 1573-1575, 2011.
- [5] D. A. B. Miller, "Self-configuring universal linear optical component," *Photonics Research*, vol. 1, no. 1, pp. 1-15, 2013.
- [6] Y. Shen, N. C. Harris, S. Skirlo, M. Prabhu, T. Baehr-Jones, M. Hochberg, X. Sun, S. Zhao, H. Larochelle, D. Englund and M. Soljačić, "Deep learning with coherent nanophotonic circuits," *Nature Photonics*, vol. 11, pp. 441-446, 2017.
- [7] S. Aaronson and A. Arkhipov, "The computational complexity of linear optics," in *Proceedings of the forty-third annual ACM symposium on Theory of computing*, 2011.
- [8] JePPIX, 27 October 2014. [Online]. Available: <https://www.lightjumps.eu/get-inspired/photronics-post/jepix-foundry-services-deliver-120-circuits-two-years/>. [Accessed August 2019].
- [9] H. Takahashi, "High performance planar lightwave circuit devices for large capacity transmission," *Optics Express*, vol. 19, no. 26, pp. B173-B180, 2011.
- [10] S. Saeidi, P. Rasekh, K. M. Awan, A. Tüngen, M. J. Huttunen and K. Dolgaleva, "Demonstration of optical nonlinearity in InGaAsP/InP passive waveguides," *Optical Materials*, vol. 84, pp. 524-530, 2018.
- [11] I. Agha, M. Davanço, B. Thurston and K. Srinivasan, "Low-noise chip-based frequency conversion by four-wave-mixing Bragg scattering in SiNx waveguides," *Optics Letters*, vol. 37, no. 14, pp. 2997-2999, 2012.

- [12] [Online]. Available:
<https://www.fotonik.dtu.dk/english/Research/Nanophotonics/Nanodev/Research/Silicon-photonics>. [Accessed August 2019].
- [13] M. Reck, A. Zeilinger, H. J. Bernstein and P. Bertani, "Experimental realization of any discrete unitary operator," *Physical Review Letters*, vol. 73, no. 1, pp. 58-61, 1994.
- [14] G. T. Reed, G. Mashanovich, F. Y. Gardes and D. J. Thomson, "Silicon optical modulators," *Nature Photonics*, vol. 4, pp. 528-526, 2010.
- [15] J. Carolan, C. Harrold, C. Sparrow, E. Martín-López, N. J. Russell, J. W. Silverstone, P. J. Shadbolt, N. Matsuda, N. Oguma, M. Itoh, G. D. Marshall, M. G. Thompson, J. C. F. Matthews, T. Hashimoto, J. L. O'Brien and A. Laing, "Universal linear optics," *Science*, vol. 349, no. 6249, pp. 711-716, 2015.
- [16] A. Annoni, E. Guglielmi, M. Carminati, G. Ferrari, M. Sampietro, D. A. B. Miller, A. Melloni and F. Morichetti, "Unscramble light-automatically undoing strong mixing between modes," *Light: Science & Applications*, vol. 6, no. 12, p. e17110, 2017.
- [17] N. C. Harris, G. R. Steinbrecher, M. Prabhu, Y. Lahini, J. Mower, D. Bunandar, C. Chen, F. N. C. Wong, T. Baehr-Jones, M. Hochberg, S. Lloyd and D. Englund, "Quantum transport simulations in a programmable nanophotonic processor," *Nature Photonics*, vol. 11, pp. 447-452, 2017.
- [18] Y. Shen, N. C. Harris, S. Skirlo, M. Prabhu, T. Baehr-Jones, M. Hochberg, X. Sun, S. Zhao, H. Larochelle, D. Englund and M. Soljačić, "Deep learning with coherent nanophotonic circuits," *Nature Photonics*, vol. 11, pp. 441-446, 2017.
- [19] A. Ribeiro, A. Ruocco, L. Vanacker and W. Bogaerts, "Demonstration of a 4×4 -port universal linear circuit," *Optica*, vol. 3, no. 12, pp. 1348-1357, 2016.
- [20] D. Melati, A. Alippi and A. Melloni, "Reconfigurable photonic integrated mode (de)multiplexer for SDM fiber transmission," *Optics Express*, vol. 24, no. 12, pp. 12625-12634, 2016.
- [21] D. Melati, A. Alippi, A. Annoni, N. Peserico and A. Melloni, "Integrated all-optical MIMO demultiplexer for mode- and wavelength-division multiplexed transmission," *Optics Letters*, vol. 42, no. 2, pp. 342-345, 2017.

- [22] C. Taballione, T. A. W. Wolterink, J. Lugani, A. Eckstein, B. A. Bell, R. Grootjans, I. Visscher, J. J. Renema, D. Geskus, C. G. H. Roeloffzen, I. A. Walmsley, P. W. H. Pinkse and K.-J. Boller, "8×8 Programmable Quantum Photonic Processor based on Silicon Nitride Waveguides," in *Frontiers in Optics / Laser Science*, 2018.
- [23] J.-F. Morizur, L. Nicholls, P. Jian, S. Armstrong, N. Treps, B. Hage, M. Hsu, W. Bowen, J. Janousek and H.-A. Bachor, "Programmable unitary spatial mode manipulation," *Journal of the Optical Society of America A*, vol. 27, no. 11, pp. 2524-2531, 2010.
- [24] N. K. Fontaine, R. Ryf, H. Chen, S. Wittek, J. Li, J. C. Alvarado, J. E. A. Lopez, M. Cappuzzo, R. Kopf, A. Tate, H. Safar, C. Bolle, D. T. Neilson, E. Burrows, K. W. Kim, P. Sillard, F. Achten, M. Bigot, A. Amezcua-Correa, R. A. Correa, J. Du, Z. He and J. Carpenter, "Packaged 45-mode multiplexers for a 50- μm graded index fiber," in *European Conference on Optical Communication (ECOC)*, Rome, 2018.
- [25] N. K. Fontaine, R. Ryf, H. Chen, D. Neilson and J. Carpenter, "Design of high order mode-multiplexers using multiplane light conversion," in *European Conference on Optical Communication (ECOC)*, Gothenburg, 2017.
- [26] K. Okamoto, *Fundamentals of optical waveguides*, Academic Press, 2006.
- [27] E. A. J. Marcatili, "Dielectric rectangular waveguide and directional coupler for integrated optics," *The Bell System Technical Journal*, vol. 48, no. 7, pp. 2071-2102, 1969.
- [28] M. S. Stern, "Semivectorial polarized finite difference method for optical waveguides with arbitrary index profiles," *IEEE Proceedings J - Optoelectronics*, vol. 135, no. 1, pp. 56-63, 1988.
- [29] K. Bierwirth, N. Schulz and F. Arndt, "Finite-difference analysis of rectangular dielectric waveguide structures," *IEEE Transactions on Microwave Theory and Techniques*, vol. 34, no. 11, pp. 1104-1114, 1986.
- [30] Z. Zhu and T. G. Brown, "Full-vectorial finite-difference analysis of microstructured optical fibers," *Optics Express*, vol. 10, no. 17, pp. 853-864, 2002.
- [31] K. S. Yee, "Numerical solution of initial boundary value problems involving Maxwell's equations in isotropic media," *IEEE Transactions on Antennas and Propagation*, vol. 14, no. 3, pp. 302-307, 1966.

- [32] J. V. Roey, J. v. d. Donk and P. E. Lagasse, "Beam-propagation method: analysis and assessment," *Journal of the Optical Society of America*, vol. 71, no. 7, pp. 803-810, 1981.
- [33] D. Gallagher, "Photonic CAD matures," *IEEE LEOS NewsLetter*, pp. 8-14, 2008.
- [34] A. Taflove and S. C. Hagness, *Computational electrodynamics: the finite-difference time-domain method*, Artech house, 2005.
- [35] G. Sztefka and H. P. Nolting, "Bidirectional eigenmode propagation for large refractive index steps," *IEEE Photonics Technology Letters*, vol. 5, no. 5, pp. 554-557, 1993.
- [36] D. F. G. Gallagher and T. P. Felici, "Eigenmode expansion methods for simulation of optical propagation in photonics: pros and cons," in *Proc. SPIE 4987, Integrated Optics: Devices, Materials, and Technologies VII*, 2003.
- [37] Q. Xu, D. Fattal and R. G. Beausoleil, "Silicon microring resonators with 1.5- μm radius," *Optics Express*, vol. 16, no. 6, pp. 4309-4315, 2008.
- [38] K. Yamada, "Silicon photonic wire waveguides: fundamentals and applications," in *Silicon Photonics II*, Berlin, Springer, 2011, pp. 1-29.
- [39] K. K. Lee, D. R. Lim, L. C. Kimerling, J. Shin and F. Cerrina, "Fabrication of ultralow-loss Si/SiO₂ waveguides by roughness reduction," *Optics Letters*, vol. 26, no. 23, pp. 1888-1890, 2001.
- [40] Y. A. Vlasov and S. J. McNab, "Losses in single-mode silicon-on-insulator strip waveguides and bends," *Optics Express*, vol. 12, no. 8, pp. 1622-1631, 2004.
- [41] S. K. Selvaraja, P. D. Heyn, G. Winroth, P. Ong, G. Lepage, C. Cailler, A. Rigny, K. K. Bourdelle, W. Bogaerts, D. V. Thourhout, J. V. Campenhout and P. Absil, "Highly uniform and low-loss passive silicon photonics devices using a 300mm CMOS platform," in *Optical Fiber Communication Conference*, San Francisco, 2014.
- [42] P. Dong, W. Qian, S. Liao, H. Liang, C.-C. Kung, N.-N. Feng, R. Shafiqi, J. Fong, D. Feng, A. V. Krishnamoorthy and M. Asghari, "Low loss shallow-ridge silicon waveguides," *Optics Express*, vol. 18, no. 14, pp. 14474-14479, 2010.
- [43] Q. Xu, D. Fattal and R. G. Beausoleil, "Silicon microring resonators with 1.5- μm radius," *Optics Express*, vol. 16, no. 6, pp. 4309-4315, 2008.

- [44] S. Somekh, E. Garmire, A. Yariv, H. Garvin and R. Hunsperger, "Channel optical waveguide directional couplers," *Applied Physics Letters*, vol. 22, no. 2, pp. 46-47, 1973.
- [45] L. B. Soldano and E. C. M. Pennings, "Optical multi-mode interference devices based on self-imaging: principles and applications," *Journal of Lightwave Technology*, vol. 13, no. 4, pp. 615-627, 1995.
- [46] F. Wang, J. Yang, L. Chen, X. Jiang and M. Wang, "Optical switch based on multimode interference coupler," *IEEE Photonics Technology Letters*, vol. 18, no. 2, pp. 421-423, 2006.
- [47] S. Nagai, G. Morishima, H. Inayoshi and K. Utaka, "Multimode interference photonic switches (MIPS)," *Journal of Lightwave Technology*, vol. 20, no. 4, pp. 675-681, 2002.
- [48] K. Ogusu, "All-optical switching in nonlinear multimode interference couplers," *Japanese Journal of Applied Physics*, vol. 51, no. 8R, 082503, 2012.
- [49] J. M. Hong, H. H. Ryu, S. R. Park, J. W. Jeong, S. G. Lee, E.-H. Lee, S.-G. Park, D. Woo, S. Kim and B.-H. O, "Design and fabrication of a significantly shortened multimode interference coupler for polarizatoin splitter application," *IEEE Photonics Technology Letters*, vol. 15, no. 1, pp. 72-74, 2003.
- [50] X. Guan, H. Wu, Y. Shi and D. Dai, "Extremely small polarization beam splitter based on a multimode interference coupler with a silicon hybrid plasmonic waveguide," *Optics Letters*, vol. 39, no. 2, pp. 259-262, 2014.
- [51] Q. Wang and G. Farrell, "All-fiber multimode-interference-based refractometer sensor: proposal and design," *Optics Letters*, vol. 31, no. 3, pp. 317-319, 2006.
- [52] K. R. Kribich, R. Copperwhite, H. Barry, B.Kolodziejczyk, J. -M.Sabattié, K. O'Dwyer and B. D. MacCraith, "Novel chemical sensor/biosensor platform based on optical multimode interference (MMI) couplers," *Sensors and Actuators B: Chemical*, vol. 107, no. 1, pp. 188-192, 2005.
- [53] D. A. May-Arriolja, P. LiKamWa, J. J. Sánchez-Mondragón, R. J. Selvas-Aguilar and I. Torres-Gomez, "A reconfigurable multimode interference splitter for sensing applications," *Measurement Science and Technology*, vol. 18, no. 10, pp. 3241-3246, 2007.

- [54] M. Bachmann, P. A. Besse and H. Melchior, "General self-imaging properties in $N \times N$ multimode interference couplers including phase relations," *Applied Optics*, vol. 33, no. 18, pp. 3905-3911, 1994.
- [55] L. B. Soldano and E. C. M. Pennings, "Optical multi-mode interference devices based on self-imaging: principles and applications," *Journal of Lightwave Technology*, vol. 13, no. 4, pp. 615-627, 1995.
- [56] R. Halir, I. Molina-Fernández, A. Ortega-Moñux, J. G. Wangüemert-Pérez, D.-X. Xu, P. Cheben and S. Janz, "A design procedure for high-performance, rib-waveguide-based multimode interference couplers in silicon-on-insulator," *Journal of Lightwave Technology*, vol. 26, no. 16, pp. 2928-2936, 2008.
- [57] Z. Sheng, Z. Wang, C. Qiu, L. Li, A. Pang, A. Wu, X. Wang, S. Zou and F. Gan, "A compact and low-loss MMI coupler fabricated with CMOS technology," *IEEE Photonics Journal*, vol. 4, no. 6, pp. 2272-2277, 2012.
- [58] D. J. Thomson, Y. Hu, G. T. Reed and J.-M. Fedeli, "Low loss MMI couplers for high performance MZI modulators," *IEEE Photonics Technology Letters*, vol. 22, no. 20, pp. 1485-1487, 2010.
- [59] P. Dumais, Y. Wei, M. Li, F. Zhao, X. Tu, J. Jiang, D. Celo, D. J. Goodwill, H. Fu, D. Geng and E. Bernier, "2x2 multimode interference coupler with low loss using 248 nm photolithography," in *Optical Fiber Communication Conference (OFC)*, paper W2A.19, 2016.
- [60] D. S. Levy, R. Scarmozzino and R. M. Osgood, "Length reduction of tapered $N \times N$ MMI devices," *IEEE Photonics Technology Letters*, vol. 10, no. 6, pp. 830-832, 1998.
- [61] P. P. Sahu, "Parabolic tapered structure for an ultracompact multimode interference coupler," *Applied Optics*, vol. 48, no. 2, pp. 206-211, 2009.
- [62] D. S. Levy, R. Scarmozzino, Y. M. Li and R. M. Osgood, "A new design for ultracompact multimode interference-based 2x2 couplers," *IEEE Photonics Technology Letters*, vol. 10, no. 1, pp. 96-98, 1998.
- [63] C. M. Gee, G. D. Thurmond and H. W. Yen, "17-GHz bandwidth electro-optic modulator," *Applied Physics Letters*, vol. 43, no. 11, pp. 998-1000, 1983.

- [64] R. Spickermann, S. R. Sakamoto, M. G. Peters and N. Dagli, "GaAs/AlGaAs travelling wave electro-optic modulators with an electrical bandwidth > 40GHz," *Electronics Letters*, vol. 32, no. 12, pp. 1095-1096, 1996.
- [65] D. Chen and H. R. Fetterman, "Demonstration of 110 GHz electro-optic polymer modulators," *Applied Physics Letters*, vol. 70, no. 25, pp. 3335-3337, 1997.
- [66] B. Chmielak, M. Waldow, C. Matheisen, C. Ripperda, J. Bolten, T. Wahlbrink, M. Nagel, F. Merget and H. Kurz, "Pockels effect based fully integrated, strained silicon electro-optic modulator," *Optics Express*, vol. 19, no. 18, pp. 17212-17219, 2011.
- [67] F. Eltes, M. Kroh, D. Caimi, C. Mai, Y. Popoff, G. Winzer, D. Petousi, S. Lischke, J. E. Ortmann, L. Czornomaz, L. Zimmermann, J. Fompeyrine and S. Abel, "A novel 25 Gbps electro-optic Pockels modulator integrated on an advanced Si photonic platform," in *IEEE International Electron Devices Meeting (IEDM)*, San Francisco, 2017.
- [68] J. Fage-Pedersen, L. H. Frandsen, A. V. Lavrinenko and P. I. Borel, "A linear electrooptic effect in silicon, induced by use of strain," in *3rd IEEE International Conference on Group IV Photonics*, Ottawa, 2006.
- [69] J. Komma, C. Schwarz, G. Hofmann, D. Heinert and R. Nawrodt, "Thermo-optic coefficient of silicon at 1550 nm and cryogenic temperatures," *Applied Physics Letters*, vol. 101, no. 4, 041905, 2012.
- [70] N. Yang, Q. Qiu, J. Su and S.-J. Shi, "Research on the temperature characteristics of optical fiber refractive index," *Optik*, vol. 125, no. 19, pp. 5813-5815, 2014.
- [71] A. Trenti, M. Borghi, S. Biasi, M. Ghulinyan, F. Ramiro-Manzano, G. Pucker and L. Pavesi, "Thermo-optic coefficient and nonlinear refractive index of silicon oxynitride waveguides," *AIP Advances*, vol. 8, no. 2, 025311, 2018.
- [72] A. Arbabi and L. L. Goddard, "Measurements of the refractive indices and thermo-optic coefficients of Si₃N₄ and SiO_x using microring resonances," *Optics Letters*, vol. 38, no. 19, pp. 3878-3881, 2013.
- [73] Q. Fang, J. F. Song, T.-Y. Liow, H. Cai, M. B. Yu, G. Q. Lo and D.-L. Kwong, "Ultralow power silicon photonics thermo-optic switch with suspended phase arms," *IEEE Photonics Technology Letters*, vol. 23, no. 8, pp. 525-527, 2011.

- [74] M. R. Watts, J. Sun, C. DeRose, D. C. Trotter, R. W. Young and G. N. Nielson, "Adiabatic thermo-optic Mach–Zehnder switch," *Optics Letters*, vol. 38, no. 5, pp. 733-735, 2013.
- [75] N. C. Harris, Y. Ma, J. Mower, T. Baehr-Jones, D. Englund, M. Hochberg and C. Galland, "Efficient, compact and low loss thermo-optic phase shifter in silicon," *Optics Express*, vol. 22, no. 9, pp. 10487-10493, 2014.
- [76] K. Tanizawa, K. Suzuki, M. Toyama, M. Ohtsuka, N. Yokoyama, K. Matsumaro, M. Seki, K. Koshino, T. Sugaya, S. Suda, G. Cong, T. Kimura, K. Ikeda, S. Namiki and H. Kawashima, "Ultra-compact 32×32 strictly-non-blocking Si-wire optical switch with fan-out LGA interposer," *Optics Express*, vol. 23, no. 13, pp. 17599-17606, 2015.
- [77] A. Liu, L. Liao, D. Rubin, H. Nguyen, B. Ciftcioglu, Y. Chetrit, N. Izhaky and M. Paniccia, "High-speed optical modulation based on carrier depletion in a silicon waveguide," *Optics Express*, vol. 15, no. 2, pp. 660-668, 2007.
- [78] N.-N. Feng, S. Liao, D. Feng, P. Dong, D. Zheng, H. Liang, R. Shafiiha, G. Li, J. E. Cunningham, A. V. Krishnamoorthy and M. Asghari, "High speed carrier-depletion modulators with 1.4V-cm $V\pi L$ integrated on 0.25 μm silicon-on-insulator waveguides," *Optics Express*, vol. 18, no. 8, pp. 7994-7999, 2010.
- [79] Z.-Y. Li, D.-X. Xu, W. R. McKinnon, S. Janz, J. H. Schmid, P. Cheben and J.-Z. Yu, "Silicon waveguide modulator based on carrier depletion in periodically interleaved PN junctions," *Optics Express*, vol. 17, no. 18, pp. 15947-15958, 2009.
- [80] L. Liao, D. Samara-Rubio, M. Morse, A. Liu, D. Hodge, D. Rubin, U. D. Keil and T. Franck, "High speed silicon Mach-Zehnder modulator," *Optics Express*, vol. 13, no. 8, pp. 3129-3135, 2005.
- [81] D. J. Thomson, F. Y. Gardes, J.-M. Fedeli, S. Zlatanovic, Y. Hu, B. P. P. Kuo, E. Myslivets, N. Alic, S. Radic, G. Z. Mashanovich and G. T. Reed, "50-Gb/s Silicon Optical Modulator," *IEEE Photonics Technology Letters*, vol. 24, no. 4, pp. 234 - 236, 2012.
- [82] A. Densmore, D.-X. Xu, P. Waldron, S. Janz, P. Cheben, J. Lapointe, A. Del age, B. Lamontagne, J. H. Schmid and E. Post, "A Silicon-on-Insulator Photonic Wire Based Evanescent Field Sensor," *IEEE Photonics Technology Letters*, vol. 18, no. 23, pp. 2520-2522, 2006.

- [83] A. Densmore, D.-X. Xu, S. Janz, P. Waldron, T. Mischki, G. Lopinski, A. Delâge, J. Lapointe, P. Cheben, B. Lamontagne and J. H. Schmid, "Spiral-path high-sensitivity silicon photonic wire molecular sensor with temperature-independent response," *Optics Letters*, vol. 33, no. 6, pp. 596-598, 2008.
- [84] J. Wo, G. Wang, Y. Cui, Q. Sun, R. Liang, P. P. Shum and D. Liu, "Refractive index sensor using microfiber-based Mach–Zehnder interferometer," *Optics Letters*, vol. 37, no. 1, pp. 67-69, 2012.
- [85] Z. Li, C. Liao, Y. Wang, L. Xu, D. Wang, X. Dong, S. Liu, Q. Wang, K. Yang and J. Zhou, "Highly-sensitive gas pressure sensor using twin-core fiber based in-line Mach-Zehnder interferometer," *Optics Express*, vol. 23, no. 5, pp. 6673-6678, 2015.
- [86] C. J. Oton, C. Manganelli, F. Bontempi, M. Fournier, D. Fowler and C. Kopp, "Silicon photonic waveguide metrology using Mach-Zehnder interferometers," *Optics Express*, vol. 24, no. 6, pp. 6265-6270, 2016.
- [87] G. Shi, F. Zhang, X.-H. Qu and X. Meng, "High-resolution frequency-modulated continuous-wave laser ranging for precision distance metrology applications," *Optical Engineering*, vol. 53, no. 12, 122402, 2014.
- [88] D. Bonneau, E. Engin, K. Ohira, N. Suzuki, H. Yoshida, N. Iizuka, M. Ezaki, C. M. Natarajan, M. G. Tanner, R. H. Hadfield, S. N. Dorenbos, V. Zwiller, J. L. O'Brien and M. G. Thompson, "Quantum interference and manipulation of entanglement in silicon wire waveguide quantum circuits," *New Journal of Physics*, vol. 14, 045003, 2012.
- [89] B. Qi, L.-L. Huang, L. Qian and H.-K. Lo, "Experimental study on the Gaussian-modulated coherent-state quantum key distribution over standard telecommunication fibers," *Physical Review A*, vol. 76, no. 5, 052323, 2007.
- [90] P. Sibson, C. Erven, M. Godfrey, S. Miki, T. Yamashita, M. F. M. Sasaki, H. Terai, M. G. Tanner, C. M. Natarajan, R. H. Hadfield, J. L. O'Brien and M. G. Thompson, "Chip-based quantum key distribution," *Nature Communications*, vol. 8, 13984, 2017.
- [91] C. Ma, W. D. Sacher, Z. Tang, J. C. Mikkelsen, Y. Yang, F. Xu, T. Thiessen, H.-K. Lo and J. K. S. Poon, "Silicon photonic transmitter for polarization-encoded quantum key distribution," *Optica*, vol. 3, no. 11, pp. 1274-1278, 2016.
- [92] K. Bartkiewicz, A. Černoč, D. Javůrek, K. Lemr, J. Soubusta and J. Svozilík, "One-state vector formalism for the evolution of a quantum state

- through nested Mach-Zehnder interferometers," *Physical Review A*, vol. 91, no. 1, 012103, 2015.
- [93] D. A. B. Miller, "Perfect optics with imperfect components," *Optica*, vol. 2, no. 8, pp. 747-750, 2015.
- [94] C. M. Wilkes, X. Qiang, J. Wang, R. Santagati, S. Paesani, X. Zhou, D. A. B. Miller, G. D. Marshall, M. G. Thompson and J. L. O'Brien, "60 dB high-extinction auto-configured Mach-Zehnder interferometer," *Optics Letters*, vol. 41, no. 22, pp. 5318-5321, 2016.
- [95] K. Shiraishia, H. Yoda, A. Ohshima and H. Ikedo, "A silicon-based spot-size converter between single-mode fibers and Si-wire waveguides using cascaded tapers," *Applied Physics Letters*, vol. 91, 141120, 2007.
- [96] N. Hatori, T. Shimizu, M. Okano, M. Ishizaka, T. Yamamoto, Y. Urino, M. Mori, T. Nakamura and Y. Arakawa, "A hybrid integrated light source on a silicon platform using a trident spot-size converter," *Journal of Lightwave Technology*, vol. 32, no. 7, pp. 1329-1336, 2014.
- [97] R. Takei, M. Suzuki, E. Omoda, S. Manako, T. Kamei, M. Mori and Y. Sakakibara, "Silicon knife-edge taper waveguide for ultralow-loss spot-size converter fabricated by photolithography," *Applied Physics Letters*, vol. 102, 101108, 2013.
- [98] N. Fang, Z. Yang, A. Wu, J. Chen, M. Zhang, S. Zou and X. Wang, "Three-dimensional tapered spot-size converter based on (111) silicon-on-insulator," *IEEE Photonics Technology Letters*, vol. 21, no. 12, pp. 820-822, 2009.
- [99] K. Watanabe, S. Kamei, H. Hirota, M. Kohtoku and Y. Inoue, "Low loss and compact arrayed waveguide grating with double-core spot-size converters," in *31st European Conference on Optical Communication (ECOC)*, Glasgow, paper Th. 3.6.5, 2005.
- [100] Z. I. Borevich and S. L. Krupetskii, "Subgroups of the unitary group that contain the group of diagonal matrices," *Journal of Soviet Mathematics*, vol. 17, pp. 1951-1959, 1981.
- [101] D. Serre, *Matrices: Theory and Applications*, Springer, pp. 202, 2002.
- [102] P. J. M. v. Laarhoven and E. H. L. Aarts, "Simulated annealing," in *Simulated Annealing: Theory and Applications*, Springer, 1987, pp. 7-15.
- [103] F. Mezzadri, "How to generate random matrices from the classical compact groups," *NOTICES of the AMS*, vol. 54, pp. 592-604, 2007.

- [104] N. P. Diamantopoulos, M. Hayashi, Y. Yoshida, A. Maruta, R. Maruyama, N. Kuwaki, K. Takenaga, H. Uemura, S. Matsuo and K. Kitayama, "Mode-selective optical packet switching in mode-division multiplexing networks," *Optics Express*, vol. 23, no. 18, pp. 23660-23666, 2015.
- [105] "MODE - EigenMode Expansion (EME) solver introduction," Lumerical, [Online]. Available: <https://support.lumerical.com/hc/en-us/articles/360034396614-MODE-EigenMode-Expansion-EME-solver-introduction>. [Accessed 18 12 2019].
- [106] D. A. B. Miller, "Self-aligning universal beam coupler," *Optics Express*, vol. 21, no. 5, pp. 6360-6370, 2013.
- [107] R. Hanfoug, L. M. Augustin, Y. Barbarin, J. J. G. M. v. d. Tol, E. A. J. M. Bente, F. Karouta, D. Rogers, S. Cole, Y. S. Oei, X. J. M. Leijtens and M. K. Smit, "Reduced reflections from multimode interference couplers," *Electronics Letters*, vol. 42, no. 8, pp. 465-466, 2006.
- [108] E. Kleijn, D. Melati, A. Melloni, T. d. Vries, M. K. Smit and X. J. M. Leijtens, "Multimode Interference Couplers With Reduced Parasitic Reflections," *IEEE Photonics Technology Letters*, vol. 26, no. 4, pp. 408-410, 2014.
- [109] R. Burgwal, W. R. Clements, D. H. Smith, J. C. Gates, W. S. Kolthammer, J. J. Renema and I. A. Walmsley, "Using an imperfect photonic network to implement random unitaries," *Optics Express*, vol. 25, no. 23, pp. 28236-28245, 2017.
- [110] G. Labroille, B. Denolle, P. Jian, P. Genevieux, N. Treps and J.-F. Morizur, "Efficient and mode selective spatial mode multiplexer based on multi-plane light conversion," *Optics Express*, vol. 22, no. 13, pp. 15599-15607, 2014.
- [111] N. K. Fontaine, R. Ryf, H. Chen, D. T. Neilson, K. Kim and J. Carpenter, "Scalable mode sorter supporting 210 Hermite-Gaussian modes," in *Optical Fiber Communication Conference (OFC)*, paper Th4B.4, 2018.
- [112] Y. Ota, S. Ashhab and F. Nori, "Implementing general measurements on linear optical and solid-state qubits," *Physical Review A*, vol. 85, no. 4, 043808, 2012.
- [113] M. L. Cooper and S. Mookherjea, "Numerically-assisted coupled-mode theory for silicon waveguide couplers and arrayed waveguides," *Optics Express*, vol. 17, no. 3, pp. 1583-1599, 2009.

- [114] B. B. Bakir, A. V. d. Gyves, R. Orobtchouk, P. Lyan, C. Porzier, A. Roman and J.-M. Fedeli, "Low-loss (<1 dB) and polarization-insensitive edge fiber couplers fabricated on 200-nm silicon-on-insulator wafers," *IEEE Photonics Technology Letters*, vol. 22, no. 11, pp. 739-741, 2010.

Publications

Journal papers

(Related to this work)

[1] (*co-first and corresponding author) Ryota Tanomura, **Rui Tang***, Samir Ghosh, Takuo Tanemura, and Yoshiaki Nakano, “Robust integrated optical unitary converter using multiport directional couplers,” *Journal of Lightwave Technology*, 38(1), pp. 60-66, 2020.

[2] **Rui Tang**, Takuo Tanemura, Samir Ghosh, Keijiro Suzuki, Ken Tanizawa, Kazuhiro Ikeda, Hitoshi Kawashima, and Yoshiaki Nakano, “Reconfigurable all-optical on-chip MIMO three-mode demultiplexing based on multi-plane light conversion,” *Optics Letters*, 43(8), pp. 1798-1801, 2018.

[3] **Rui Tang**, Takuo Tanemura, and Yoshiaki Nakano, “Integrated reconfigurable unitary optical mode converter using MMI couplers,” *IEEE Photonics Technology Letters*, 29(12), pp. 971-974, 2017.

(Others)

[4] Yusuke Kohno, Kento Komatsu, **Rui Tang**, Yasuyuki Ozeki, Yoshiaki Nakano, and Takuo Tanemura, “Ghost imaging using a large-scale silicon photonic phased array chip,” *Optics Express*, 27(3), pp. 3817-3823, 2019.

[5] Taichiro Fukui, Yusuke Kohno, **Rui Tang**, Yoshiaki Nakano, and Takuo Tanemura, “Resolution-enhanced phased-array imaging via multimode fiber,” 2020 (Submitted to *Optica*).

International conferences

(Related to this work)

[1] Ryota Tanomura, **Rui Tang**, Samir Ghosh, Takuo Tanemura, and Yoshiaki Nakano, “Integrated reconfigurable 4×4 optical unitary converter using multiport directional couplers,” *Optical Fiber Communication Conference (OFC)*, paper Th1E.3, 2019.

[2] **Rui Tang**, Takuo Tanemura, Samir Ghosh, Keijiro Suzuki, Ken Tanizawa, Kazuhiro Ikeda, Hitoshi Kawashima, and Yoshiaki Nakano, “Reconfigurable 3 channel all optical MIMO circuit on silicon based on multi plane light conversion,” *Optical Fiber Communication Conference (OFC)*, paper W1E.3, 2018.

[3] **Rui Tang**, Takuo Tanemura, and Yoshiaki Nakano, “Robust reconfigurable optical mode demux using multiport directional couplers,” *Opto-Electronics and Communications Conference (OECC)* and *Photonics Global Conference (PGC)*, paper s2385, 2017.

[4] **Rui Tang**, Takuo Tanemura, and Yoshiaki Nakano, “Reconfigurable integrated MIMO optical mode demultiplexer using MMI couplers,” *Conference on Lasers and Electro-Optics (CLEO)*, paper JTh2A.116, 2017.

(Others)

[5] Taichiro Fukui, Yusuke Kohno, **Rui Tang**, Yoshiaki Nakano, and Takuo Tanemura, “Single-pixel imaging through multimode fiber using silicon optical phased array chip,” *Optical Fiber Communication Conference (OFC)*, paper M2C.2, 2020 (accepted).

[6] Ryota Tanomura, **Rui Tang**, Samir Ghosh, Takuo Tanemura, and Yoshiaki Nakano, “Monolithic InP 4×4 optical unitary converter for all-optical MIMO demultiplexing,” *European Conference on Optical Communication (ECOC)*, paper P49, 2019.

[7] Ryota Tanomura, **Rui Tang**, Samir Ghosh, Takuo Tanemura, and Yoshiaki Nakano, “Compact reconfigurable optical unitary converter based on non-uniform multimode interference coupler,” *Photonics Switching and Computing Conference (PSC)*, paper TuF3.1, 2019.

Domestic conferences

(Related to this work)

[1] 田之村 亮汰, **唐 睿**, 種村 拓夫, 中野 義昭, “多ポート方向性結合器を利用した4チャンネルユニタリ光モード変換器の実証,” *Photonics Device Workshop*, 2018年.

[2] 種村 拓夫, **唐 睿**, Samir Ghosh, 中野 義昭, “光集積回路による全光MIMO処理/任意ユニタリ変換デバイス,” 電子情報通信学会ソサイエティ大会, BI-2-6, 2018年.

[3] **唐 睿**, 種村 拓夫, 中野 義昭, “多モード干渉結合器を用いた光MIMO処理回路,” 電子情報通信学会ソサイエティ大会, C-3-41, 2016年.

(Others)

[4] 田之村 亮汰, **唐 睿**, 種村 拓夫, 中野 義昭, “InP光集積4×4ユニタリ変換器の実証,” 電子情報通信学会ソサイエティ大会, C-3-19, 2019年.

[5] 田之村 亮汰, **唐 睿**, 種村 拓夫, 中野 義昭, “非等分配多モード干渉器による小型光ユニタリ変換器の検証,” 電子情報通信学会総合大会, C-3-14, 2019年.

Acknowledgement

First of all, I would like to express my sincere gratitude to my supervisor, Prof. Yoshiaki Nakano, for managing the lab, giving comments and advice at the lab meetings, and providing sufficient research equipment and funds for all the lab members. Prof. Nakano gave me his full support to my research, scholarship applications, and oversea visit. His decades of experience in research and life is a precious treasure for everyone in the lab.

I would like to thank my research advisor, Prof. Takuo Tanemura, for supervising this project and providing numerous advice throughout the years. He has been an awesome mentor for all students in the PIC group. This thesis cannot be completed without his guidance and advice.

I would like to thank Prof. Masakazu Sugiyama, for providing insightful comments on this thesis and technical advice at the lab meetings.

I would like to thank Prof. Yasuyuki Ozeki, for providing technical advice on the design of the electronic circuit and important comments on this thesis.

I would like to thank Prof. Toshihiko Yamasaki for his insightful comments, which greatly improve the quality of this thesis.

I would like to thank my colleague, Dr. Samir Ghosh, for teaching me many things about the experiments. It would have cost me much more time to characterize the devices without his help. I would like to thank Ryota Tanomura, who has been an awesome collaborator. I would also like to thank Daiji Yamashita, Kento Komatsu, and Yuki Okamoto. They provided many useful suggestions on the design and debugging of the electronic circuit.

I would like to thank many other colleagues at UTokyo, especially Yi Xiao, Jiaqi Zhang, Hsiang-Hung Huang, Hao Xu, Peng Zhou, Takahiro Suganuma, Yusuke Kohno, Yuguang Wang, Taichiro Fukui, and Kaiyin Feng.

I would like to thank Prof. Dirk Englund for hosting me one year at MIT. I learned many new things about quantum photonics and optical neural networks at his lab. It was a wonderful experience. I would like to thank my colleague, Dr. Jacques Carolan, who is an excellent researcher and one of the pioneers in the field of programmable

linear optics. I would like to thank Dr. Ryan Hamerly. Together, we designed so far the largest-scale optical neural network chip. I would also like to thank Uttara Chakraborty, Ian Christen, Cheng Peng, Mihika Prabhu, Christopher Panuski, Jordan Goldstein, and Hugo Larocque.

I would like to thank my scholarship sponsors: University of Tokyo, Takaku Foundation, Tokyu Foundation for Foreign Students, and Atsumi International Scholarship Foundation. Without their kind support, I would not be able to fully concentrate on my study and research.

Last but not least, I am grateful for the support from my family, especially my parents. Nothing would happen without their support.